

Active control of turbulent skin-friction

An experimental study

Ujjaini Kempaiah, K.

DOI

[10.4233/uuid:0e2ad030-dcb4-4cd1-8cd8-127e65ddc1ef](https://doi.org/10.4233/uuid:0e2ad030-dcb4-4cd1-8cd8-127e65ddc1ef)

Publication date

2023

Document Version

Final published version

Citation (APA)

Ujjaini Kempaiah, K. (2023). *Active control of turbulent skin-friction: An experimental study*. [Dissertation (TU Delft), Delft University of Technology]. <https://doi.org/10.4233/uuid:0e2ad030-dcb4-4cd1-8cd8-127e65ddc1ef>

Important note

To cite this publication, please use the final published version (if applicable). Please check the document version above.

Copyright

Other than for strictly personal use, it is not permitted to download, forward or distribute the text or part of it, without the consent of the author(s) and/or copyright holder(s), unless the work is under an open content license such as Creative Commons.

Takedown policy

Please contact us and provide details if you believe this document breaches copyrights. We will remove access to the work immediately and investigate your claim.

**ACTIVE CONTROL OF TURBULENT SKIN-FRICTION
AN EXPERIMENTAL STUDY**

ACTIVE CONTROL OF TURBULENT SKIN-FRICTION AN EXPERIMENTAL STUDY

Dissertation

for the purpose of obtaining the degree of doctor
at Delft University of Technology
by the authority of the Rector Magnificus Prof.dr.ir. T.H.J.J. van der Hagen;
Chair of the Board for Doctorates
to be defended publicly on
Tuesday, 14th November 2023 at 12:30 o'clock

by

Kushal UJJAINI KEMPAIAH

Master of Science in Aerospace Engineering
Delft University of Technology, The Netherlands
born in Mandya, India.

This dissertation has been approved by the *promotor* and *copromotor*.

Composition of the doctoral committee:

Rector Magnificus,	chairperson
Prof.dr. F. Scarano,	TU Delft, <i>promotor</i>
Dr.ir. W. Baars,	TU Delft, <i>copromotor</i>

Independent members:

Prof.dr.ir. S. Hickel,	TU Delft
Prof.dr. K.S. Choi,	University of Nottingham, United Kingdom
Prof.dr. M. Quadrio,	Politecnico di Milano, Italy
Dr. D. Michealis,	LaVision GmbH, Germany
Dr.Ing. J. Kriegseis	KIT, Germany

Reserve member:

Prof.dr.ir. A.C. Viré,	TU Delft
------------------------	----------



Keywords: Quantitative flow visualization, Particle image velocimetry, Skin-friction reduction, wall bounded turbulence

Printed by:

Front & Back:

Copyright © 2023 by K.U. Kempaiah (TU Delft Open Access)

ISBN 978-94-6366-773-9

An electronic version of this dissertation is available at
<http://repository.tudelft.nl/>.

CONTENTS

Summary	ix
1 Introduction	1
1.1 Aerodynamics for sustainable aviation	1
1.2 Objectives of current work.	5
1.2.1 Skin-friction reductions from wall oscillation	5
1.2.2 Effect of wall oscillation on the coherent structures	5
1.2.3 Techniques for high Reynolds number regimes	6
1.3 Outline of thesis	6
2 Wall bounded turbulence and its control	9
2.1 Turbulent boundary layers	10
2.1.1 Scaling and statistical representation	11
2.1.2 Near-wall structures	15
2.1.3 Structures in the logarithmic region.	16
2.1.4 Large and very-large scale structures	19
2.2 Skin-friction reduction techniques	20
2.2.1 Spanwise wall oscillations	22
2.2.2 Travelling waves	26
2.2.3 Plasma actuators	29
2.2.4 Rotating discs	32
2.3 Research questions.	36
3 Particle Image Velocimetry	37
3.1 Working principle	38
3.2 Tracer particles	40
3.3 Illumination of the flow	42
3.4 Imaging of tracer particles	44
3.5 Image interrogation	45
3.6 PIV dynamic ranges, errors and uncertainties	46
4 Skin-friction control by spanwise wall oscillations	49
4.1 Introduction	50
4.2 Experimental setup and procedure	51
4.2.1 Wind tunnel and oscillating wall	51

4.2.2	PIV setup	53
4.2.3	Data reduction and uncertainty analysis	55
4.2.4	Drag reduction evaluation	57
4.3	Results and discussion	58
4.3.1	Turbulent boundary layer characteristics	58
4.3.2	Turbulent skin-friction analysis	58
4.3.3	Reynolds stress and turbulence production	60
4.3.4	Instantaneous flow organization	63
4.3.5	Tomographic PIV flow visualizations	66
4.3.6	Proposed physical mechanism	69
4.4	Conclusion	71
5	Distortion of coherent structures in TDR regime	73
5.1	Introduction	74
5.2	Experimental setup and procedure	75
5.2.1	Flow facility and boundary layer properties	75
5.2.2	Tomographic PIV and assessment of measured velocity.	75
5.2.3	Data reduction	77
5.3	Results and discussion	82
5.3.1	Analysis by spatial correlation	82
5.3.2	Analysis by feature detection	87
5.3.3	Properties, phase statistics and conceptual model.	89
5.4	Conclusion	94
6	Plasma based surrogate of the oscillating wall	95
6.1	Introduction	96
6.2	Experimental setup and procedure	97
6.2.1	Characterisation in quiescent conditions.	97
6.2.2	Boundary layer environment	103
6.3	Results and discussion	105
6.3.1	Plasma field comparison.	105
6.3.2	Effect of plasma actuator on TBL	106
6.4	Steady actuator as a surrogate.	108
6.5	Conclusion	110
7	TBL control by an array of rotating discs	113
7.1	Introduction	114
7.2	Experimental methodology	115
7.2.1	Wind tunnel and array of rotating discs.	115
7.2.2	PIV Setup	116

7.3	Results.	117
7.3.1	Boundary layer assessment	117
7.3.2	Large scale flow organization	118
7.4	Conclusion	122
8	Conclusion	125
8.1	Mechanical wall oscillations.	126
8.2	Mechanism of skin-friction reductions.	127
8.3	Extension to large Reynolds numbers	127
8.3.1	Plasma surrogate of wall oscillations	127
8.3.2	Array of flush mounted rotating discs.	128
	References	131
	Acknowledgements	145
	Curriculum vitae	147
	List of publications	149

SUMMARY

A flying aircraft consumes fuel to overcome air resistance during its motion. A significant part of this consumption (55%) is due to turbulent skin friction arising at the interface of the aircraft surface and the air. The current work aims to develop and investigate relevant turbulent skin-friction reduction techniques and assist in advancing technologies that will contribute to achieving a reduction in turbulent skin-friction drag and, consequently, fuel consumption and the associated emissions.

The thesis examines active flow control techniques derived from the spanwise wall oscillation concept. The latter involves introducing a time-dependent spanwise motion to the wall over which a turbulent boundary layer is present. The current work relies on the experimental investigation using particle image velocimetry to quantify the effect of the active control techniques.

The turbulent skin-friction reductions obtained from the spanwise wall oscillation are quantified using high-resolution planar and tomographic-PIV, yielding a maximum drag reduction of 15% when the wall oscillates at optimum conditions. The results agree well with the computer simulations from the literature. Based on the qualitative observations of the instantaneous flow topology, a hypothesis is formulated that explains the observed reductions in skin friction. The principle states that the wall motion disrupts packets of hairpin vortices, inhibiting the hairpin auto-generation process. The inhibition in the auto-generation will affect the features in the flow, especially the streaks and ejections.

To delve deeper into the effect of the wall oscillation on the streaks and ejections. A feature detection algorithm is implemented using the 3-dimensional data obtained from tomographic-PIV. The developed feature detection algorithm is compared with the traditional analysis based on spatial correlation techniques. The latter returns limited information on the properties and arrangement due to the spatial averaging effect. Instead, the feature detection algorithm can quantify a decrease in the spatial occupation and length of the ejection events by 40% and 20%, respectively.

Additional observations are possible by feature detection, such as tilt (x - z plane) and pitch (x - y plane) of the streaks and ejections, which help form a phenomenological model of the drag reduction mechanism. The maximum observed tilt angle of approximately 20° is consistent with proposed estimates based on geometric/kinematic criteria. The overall behaviour and properties of streaks

and ejections observed here are compatible with the hypothesis proposed.

With an understanding of the underlying mechanism of turbulent skin friction, the next step is to develop alternative forcing methods to overcome mechanical wall oscillation's limitations. The primary restriction is the large actuation frequency desired for more practical flow conditions, which are not feasible. A possible solution is surrogating mechanical wall oscillation with plasma actuators.

Plasma actuators are electrical devices that produce a body force at the wall through air ionization and require no moving parts. An unsteady, uni-directional plasma actuator is developed to surrogate the oscillating wall conditions that decrease skin friction drag. However, skin-friction measurements immediately downstream of the unsteady, uni-directional plasma actuator reported a consistent increase in the skin-friction drag and momentum deficit throughout the boundary layer. The unsteadiness of the actuation leads to the formation of a starting vortex, which is unavoidable and leads to a complex non-linear interaction with the flow in the near-wall regions of the turbulent boundary layer. As a result, the chosen form of the actuator cannot be used to surrogate spanwise wall oscillation.

Therefore the unsteadiness is overcome by employing a steady actuator. The steady actuator converts the temporal variation in spanwise wall velocity into a spatially varying forcing. Due to the convecting flow, spanwise wall oscillation is still mimicked. The forcing obtained from the steady actuator produces a peak velocity close to the wall ($y = 0.8$ mm) compared to the unsteady, uni-directional actuator ($y = 3.0$ mm). This forcing leads to better confinement of the jet near the wall and indicates a potential for further investigations in future studies.

Finally, an array of flush-mounted rotating discs is an alternative to enable scaling up to more relevant flow conditions. The practical implementation of this actuation method is relatively easy as it does not require any oscillatory, linear motion but is based on steady rotational motion. The array of discs is designed and manufactured based on the optimal case in terms of the largest drag reduction, as identified in the literature using computational methods. Flow field investigations of the array in the wall-parallel plane showed low and high momentum pathways established in the flow due to the spanwise varying friction drag. The motion of the discs creates a suction effect for the flow over them. The current work reports the first experimental investigation of this concept.

1

INTRODUCTION

*Keep on beginning and failing.
Each time you fail, start all
over again, and you will
grow stronger until you have
accomplished a purpose —
not the one you began with
perhaps, but one you'll be
glad to remember.*

Anne Sullivan

1.1. AERODYNAMICS FOR SUSTAINABLE AVIATION

In the last 20 years, mankind has experienced noticeable changes in the physical climate system, from increasing global temperatures (Figure 1.1), ice volume loss, rising sea levels, to changes in global precipitation patterns (Chen et al., 2021). This has increased the occurrence of intense and extreme weather events affecting life on the planet (Jentsch and Beierkuhnlein, 2008). The Intergovernmental Panel on Climate Change (IPCC), in its 5th Assessment Report, concluded that *'it is extremely likely'* that human influence caused more than half of the observed global mean surface temperature increase from 1951 to 2010. The main drivers are the increase in the atmospheric concentrations of greenhouse gases and aerosols from burning fossil fuels and land use patterns (IPCC).

Ritchie et al. (2020), while investigating a sectorial breakdown of anthropogenic greenhouse emissions, reported that the aviation sector accounts for 2% of total

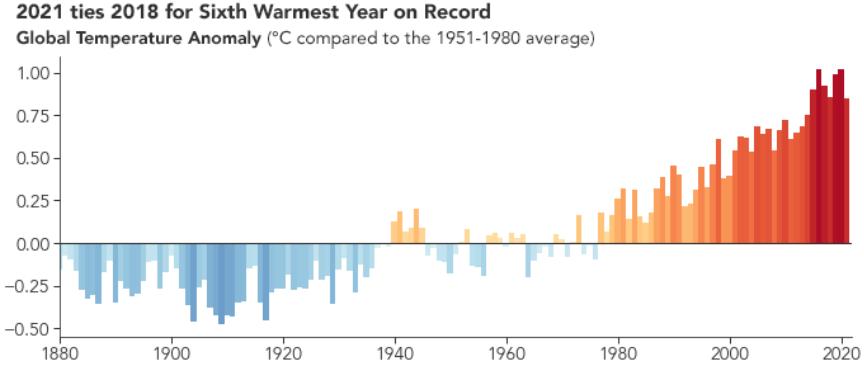


Figure 1.1: Trend of global mean air temperature with respect to the levels in the period 1951-1980 by [NASA Earth Observatory](#).

greenhouse emissions, which corresponds to 50 billion tonnes of CO_2 eq¹. The Advisory Council of Aeronautics Research in Europe (ACARE) has adopted targets for the year 2050 to reduce CO_2 emissions by 75% relative to the level in the year 2000. Both operational and technological innovations are required to meet these targets. The desired technological innovations in the aviation sector are expected from efficient propulsion systems, novel materials and a reduction in aerodynamic drag.

Aerodynamic drag can be defined as the force that is exerted on a moving object by the surrounding fluid which opposes its motion. The drag on an object arises from the distribution of pressure and shear stress along its surface. For subsonic flows with a Mach number (M)² less than 1, the drag on an object can be broadly classified as skin-friction drag and pressure drag.

Skin-friction drag originates from the shear stress distribution exerted by the fluid in the tangential direction to the surface (see Figure 1.2, top-right). The no-slip condition at the wall and the viscosity of the fluid lead to the formation of a decelerated region of flow close to the surface called the boundary layer (Figure 1.3(a)). In this region, the velocity increases from zero³ at the wall to a finite value corresponding to the outer stream. The shear stress generated at the wall (τ_w) due to the formation of the boundary layer is the primary source of skin-friction drag.

The pressure drag, on the other hand, is the axial component (opposing the relative motion) which arises due to pressure distribution in the direction normal

¹Carbon dioxide equivalent or CO_2 eq means the number of metric tons of CO_2 emissions with the same global warming potential as one metric ton of another greenhouse gas.

²Dimensionless quantity representing the ratio of flow velocity to the local speed of sound.

³due to the no-slip boundary condition at the wall.

to the surface. Flow phenomena such as separation increase the pressure drag further due to the formation of a low-pressure region behind the body called the wake (see Figure 1.2, left).

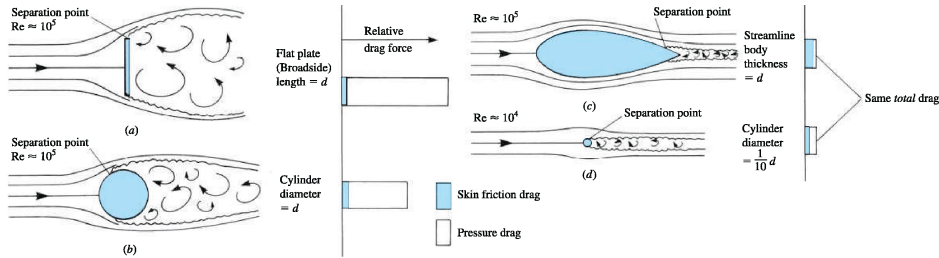


Figure 1.2: The relative comparison between skin-friction drag and pressure drag for various shapes (Anderson, 2011).

From Figure 1.2, it is clear that skin-friction drag dominates for streamlined objects like over the wing and fuselage of an aircraft where no separation occurs. Pressure drag, instead, is more prominent for bluff bodies as they feature large flow separation. For an aircraft in cruise⁴, 50-60% of the aerodynamic drag is due to skin friction (Abbas et al., 2017). For some more context, a 1% reduction in skin-friction drag translates to 0.75% in fuel savings and a reduction of CO_2 production by 2-3 tonnes per flight. For example, a trans-continental B747 flight produces roughly 400 tonnes of CO_2 (Ricco et al., 2021).

SKIN-FRICTION DRAG

The total skin-friction drag can be obtained by integrating the shear stress over the aircraft's surface in the axial direction. The local shear stress (τ_w) is obtained from the slope of the velocity profile at the wall.

$$\tau_{wall} = \mu \left. \frac{\partial u}{\partial y} \right|_{y=0} \quad (1.1)$$

The boundary layer exists in two states which are laminar (Figure 1.3(b)) and turbulent (Figure 1.3(c)). A laminar boundary layer corresponds to the orderly flow of fluid. In contrast, the flow in a turbulent boundary layer corresponds to chaotic flow with enhanced mixing, making the shape of the velocity profile fuller than its laminar counterpart; note that the turbulent boundary layer profile shown is a mean profile. From the shape of the two profiles, it should become apparent that the slope of the velocity profile, which determines the shear stress

⁴Cruise is the phase of aircraft flight that starts when the aircraft levels off after a climb until it begins to descend for landing. Most fuel is consumed in this condition (60-70%).

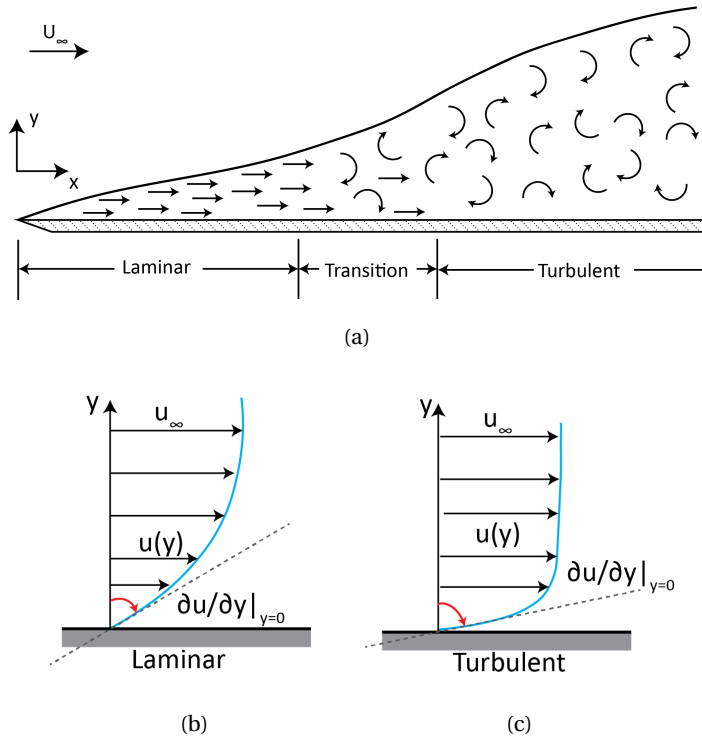


Figure 1.3: The development of a boundary layer on a flat plate with an illustration of the distinct flow behaviours (a), the velocity profile of a laminar (b) and turbulent boundary layer (c) to highlight the difference in shape and the corresponding slope near the wall.

and the skin-friction drag, is larger for the turbulent boundary layer. The state of the boundary layer can be predicted by the Reynolds Number (Re_x)⁵. In many engineering systems, Re has a large value $O(10^6)$, and the flow in the boundary layer is predominantly turbulent.

Reductions in skin-friction drag are obtained from two possible routes: transition delay and turbulent skin-friction reduction. As the name suggests, transition delay postpones the transition of the laminar flow to turbulent over the surface, thereby obtaining the benefits of laminar flow (Joslin, 1998). On the other hand, in a turbulent boundary layer, the skin friction can be reduced by acting on the complex mixing processes that occur in turbulence, for example, by introducing specifically targeted inputs to the flow. The latter is the focus of the current research.

⁵Dimensionless quantity determined from the velocity of the flow (u_∞), the viscosity of the fluid (ν) and the flow geometry (streamwise distance x) and represented as $\frac{u_\infty x}{\nu}$.

1.2. OBJECTIVES OF CURRENT WORK

The current research aims to investigate skin-friction reduction techniques that are relevant to aerodynamic flows and assist in the realization of technology that will contribute to achieving the environmental targets. The research performed comprises the following topics.

1.2.1. SKIN-FRICTION REDUCTIONS FROM WALL OSCILLATION

One of the most popular and well-documented methods is spanwise wall oscillation (SWO). This control technique introduces an unsteady spanwise oscillatory motion to the wall over which a turbulent boundary layer is present. This is documented to produce skin-friction reduction of up to 45% from numerical (Quadrio and Ricco, 2004) and experimental studies (Gouder et al., 2013). However, a determination of the skin-friction reduction from experimental methods relies on force balance measurements (Bird et al., 2018; Gouder et al., 2013). A direct measurement of the slope of the velocity profile over the oscillating wall has not been afforded due to the challenges in the desired spatial resolution and the intrusive nature of the techniques adopted.

Therefore, investigating the use of Particle Image Velocimetry (PIV) for the direct skin-friction measurement from the slope of the velocity profile is desired. Furthermore, the flow field data provide insight into the spatial organization of the flow to enhance the understanding of the mechanism at play. Thus, experimental confirmation of the results is required by employing high-resolution near-wall planar-PIV and tomographic-PIV (3-dimensional data). Through these experiments, the reductions in skin-friction drag can be quantified. In addition, the results from tomographic PIV provide an opportunity to further develop the mechanism of skin-friction reductions.

1.2.2. EFFECT OF WALL OSCILLATION ON THE COHERENT STRUCTURES

To examine the underlying mechanism of drag reductions further, the data from tomographic-PIV is employed to quantify the effects of wall oscillation on the coherent structures⁶. In literature, the flow structures are commonly analyzed using pointwise statistics or spatial correlation, which are affected due to their random and jittery appearance. Therefore there is a need to quantify the systematic distortions of the dominant turbulent structures by feature analysis, which is intended to provide an insight into the instantaneous changes to flow structures, as opposed to an average change to the statistics. The methodology adopted is based on the instantaneous distribution of Reynolds stresses, where a specific

⁶Features in the flow documented in the literature and associated with a spatial and temporal organization. They play an essential role in the enhanced mixing, leading to increased skin-friction drag, such as low and high-speed streaks, hairpin vortices, flow sweeps and ejections

spatial template is defined for low-speed streaks and flow ejections. Events corresponding to this template will be collected and parametrized with their occurrence, geometrical properties (length and orientation), and dynamics (intensity). The developed approach will be compared with the most practised statistical analysis to explain the significance of the features extracted by the detection algorithm in relation to the drag reduction mechanism.

1.2.3. TECHNIQUES FOR HIGH REYNOLDS NUMBER REGIMES

CAN PLASMA ACTUATORS SURROGATE WALL OSCILLATION?

The use of mechanical actuation has inherent drawbacks. The system is limited in the actuation frequency due to the large inertial forces involved and is a limiting factor in developing strategies that can be used at higher and more representative Reynolds numbers. Therefore, a non-moving substitute for the mechanical system of wall oscillation is desired. Plasma actuators are electrical devices that produce the desired body forces through the ionization of the air (Kotsonis, 2015). They are employed to produce near-wall forcing to achieve skin-friction reductions as reported in literature (Kriegseis et al., 2016).

This aspect of the research aims to develop an array of plasma actuators which act as a suitable surrogate of the oscillating wall. The actuators will be used to study the effect of the plasma forcing on the near-wall dynamics and the skin-friction behaviour of the turbulent boundary layer.

ARRAY OF FLUSH MOUNTED ROTATING DISCS

The limitation of spanwise wall oscillation is that when scaled to practical flow situations, the forces and the frequencies of operation will be beyond the limit of applicability. With the same motivation of scaling in Reynolds number as stated earlier, one possible option is to replace the wall oscillation with rotating discs embedded in the wall. It is to be noted that the motions induced by the disc is different from that of the earlier efforts with the oscillating wall. Nonetheless, the near-wall nature of the actuation technique is relevant, as is reported, to produce skin-friction reductions (Ricco and Hahn, 2013). The rotation of the discs about its axis overcomes the limitations of the inertial forces. Currently, there are no experimental investigations reported in literature that employ an array of rotating discs for skin-friction reductions. For this purpose, an array of flush-mounted discs will be designed and used to assess the flow manipulation of this wall-based actuation method using PIV.

1.3. OUTLINE OF THESIS

Chapter 2 provides an overview of near-wall turbulence control techniques with a specific emphasis on wall motions. The discussion covers the relevant litera-

ture from numerical, experimental and analytical studies that have been made in the field. In addition, experimental studies employing spanwise wall oscillation, plasma surrogates of the wall oscillations and rotating discs are discussed in more detail.

Chapter 3 discusses the fundamental concepts of Particle Image Velocimetry, which include the description of the technical requirements of tracer particle, illumination, imaging and image acquisition. To explain the conversion of particle images to velocity fields, the cross-correlation algorithm is introduced. Different PIV methods relevant to the current work are also described, alongside concepts of measurement error and uncertainties.

Chapter 4 presents the results of the experiments employing high-resolution planar-PIV experiments performed to quantify the skin-friction reduction through spanwise wall oscillations. The results obtained are compared with that of existing literature. Furthermore, three-dimensional measurements are obtained with tomographic-PIV, which provides information on the instantaneous velocity and vorticity distribution near the wall. The chapter concludes with a description of the hypothesis for the mechanism of skin-friction reduction based on the observations of the 3-dimensional data.

Chapter 5 focuses on developing a method to examine the effect of the wall oscillations on the coherent motions in the flow. A feature detection algorithm is introduced, and the impact of the wall oscillations on the organisation of the turbulent flow structures is presented and discussed.

In Chapter 6, an electrical system based on plasma actuators is developed to surrogate the motion of the oscillating wall. First, the unsteady actuator development and its effect on the turbulent boundary layer are discussed. The subsequent steps towards a steady operating regime are also introduced by comparing the produced forcing with the Stokes layer of the wall oscillations.

The progress of the near-wall control techniques to a higher Reynolds number is investigated in Chapter 7, where an array of flush-mounted rotating discs is employed to study the large-scale flow dynamics.

Finally, a summary of the main results and the conclusions from the earlier chapters is given in Chapter 8.

2

WALL BOUNDED TURBULENCE AND ITS CONTROL

The current chapter reviews relevant concepts and literature, which will be referred to in the remainder of the thesis.

2

2.1. TURBULENT BOUNDARY LAYERS

Boundary layer flows have been extensively studied since the landmark paper of Prandtl (1904) over a century ago. The boundary layer exists in all flows with relative motion between the fluid and the surface. The no-slip condition at the wall, coupled with the fluid's viscosity, lead to the boundary layer's formation. In the boundary layer, the velocity increases from zero at the wall to the freestream velocity away from it. In many engineering systems, the boundary layer on the surface does not remain laminar but transitions to turbulence for $Re_{x|crit} \sim 3.5 \times 10^5 - 10^6$ (Schlichting and Kestin, 1961) giving rise to the turbulent boundary layer.

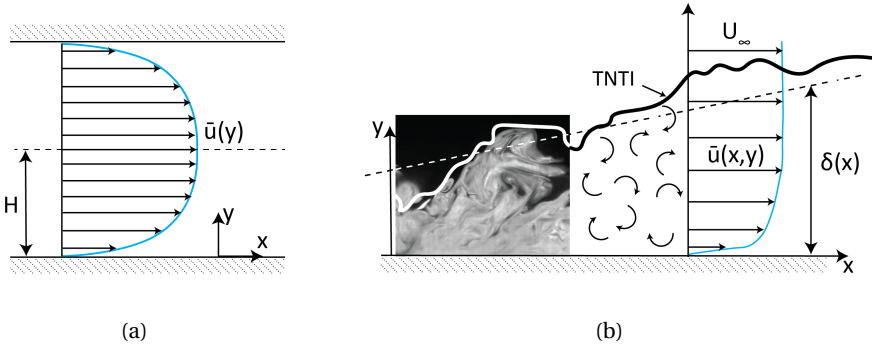


Figure 2.1: Schematic of a channel flow between two parallel plates (a) and that of a developing turbulent boundary layer (b, figure adapter from Tennekes et al. (1972)). An instantaneous smoke flow visualization from Lee et al. (2012) is superimposed on the schematic.

The concept of a turbulent boundary layer is a subset of wall-bounded turbulent flows. These flows occur at the vicinity of a fixed wall such as a channel, pipe, or flat plate. Both channel and pipe flow are classified as internal flows, while the latter is an external flow. The primary difference between the two (i.e. internal and external) is the absence of the freestream, as illustrated in Figure 2.1, and the boundary layer develops as a function of the streamwise (x) coordinate. The cyan profile corresponds to the mean profile of the velocity. The following discussions will focus on the turbulent boundary layer; however, the discussion remains largely valid for all canonical wall-bounded turbulent flows. Throughout the thesis, x , y and z indicate the streamwise, wall-normal and spanwise

directions. The respective velocity components are u , v and w . Mean flow quantities are represented by an overline (\overline{u} , \overline{v} , \overline{w}), and the fluctuating quantities obtained through a Reynolds decomposition (refer Equation 2.1) is represented with a prime (u' , v' , w').

$$u = \overline{u} + u' \quad (2.1)$$

For external flows like that shown in Figure 2.1(b), an interface can be identified as the turbulent non-turbulent interface (TNTI). In the statistical sense, the thickness of the region where the boundary layer is present is called the boundary layer thickness (δ), and it grows with \sqrt{x} (Schlichting and Kestin, 1961).

The transition to turbulence is accompanied by a significant increase in the boundary layer thickness (δ) and the wall shear stress (τ_w). Figure 2.2 shows the increase in the wall shear for the laminar and turbulent boundary layer as a function of the Reynolds number (Re_x). The penalties associated due to turbulence have far-reaching consequences in many industries (Gad-el Hak and Bandyopadhyay, 1994).

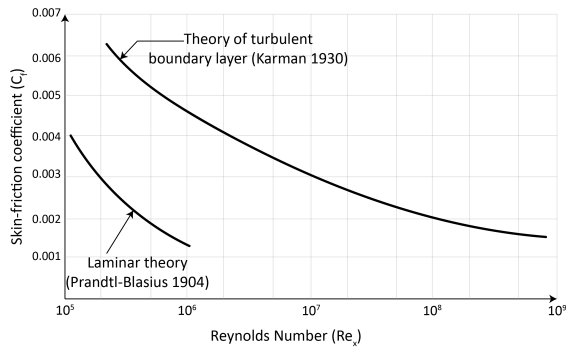


Figure 2.2: Comparison of the skin-friction coefficient of laminar and turbulent boundary layer as a function of Reynolds number (Re_x) (Von Karman, 1934).

2.1.1.1. SCALING AND STATISTICAL REPRESENTATION

In every wall-bounded turbulent flow, scaling regions can be identified where fluid flow velocities (or kinematics) scale according to specific length and time-scales. These regions are described in terms of the characteristic scaling parameters, as shown in Figure 2.3. In the near wall region Prandtl (1925) stated that the streamwise velocity is dependent on the wall-normal location (y), kinematic viscosity (ν) and the wall friction velocity (u_τ). The wall friction velocity is defined as $u_\tau = \sqrt{\frac{\tau_w}{\rho}}$, where ρ is the density of the fluid. The scaling parameters for the near wall region are the characteristic length ($l^+ = \frac{\nu}{u_\tau}$) and velocity (u_τ). The expression obtained based on the experimental data was termed the 'law of the wall'. It showed that the behaviour of the velocity profile was independent of the external flow conditions.

$$\frac{\bar{u}}{u_\tau} = f\left(\frac{yu_\tau}{\nu}\right) \quad (2.2)$$

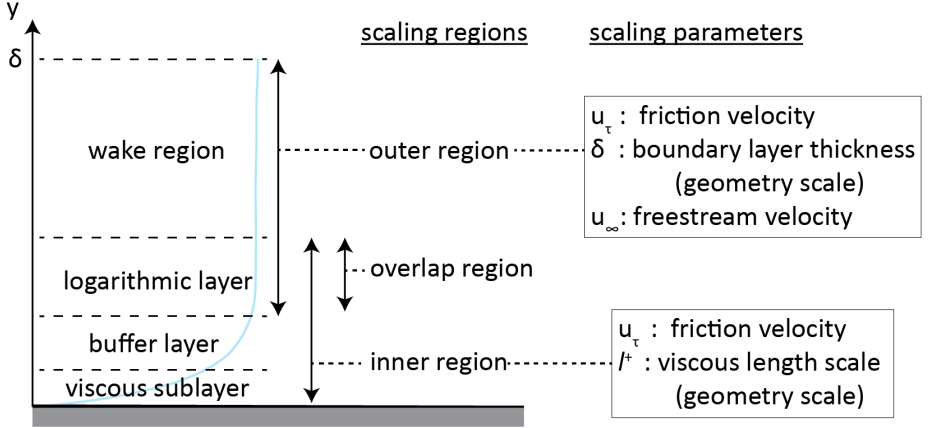


Figure 2.3: Scaling regions in a turbulent boundary layer; Figure adapted from Nieuwstadt et al. (2016).

Away from the wall in the outer region, the velocity scales with the friction velocity (u_τ), the freestream velocity (U_∞) and the thickness of the boundary layer (δ) and is referred to as the 'deficit law' as shown in Equation 2.3.

$$\frac{U_\infty - \bar{u}}{u_\tau} = f\left(\frac{y}{\delta}\right) \quad (2.3)$$

In addition, there is a region in the flow referred to as the overlap region where both scaling laws are valid. Therefore, the matching condition proposed by Millikan (1939) states that the solutions of the above two equations (Equation 2.4, 2.5) are continuous. Finally, the matching condition is applied to the velocity gradients, which results in the solution exhibiting a logarithmic velocity profile, as shown below.

$$\frac{\bar{u}}{u_\tau} = \frac{1}{\kappa} \ln\left(\frac{yu_\tau}{\nu}\right) + A \quad (2.4)$$

$$\frac{U_\infty - \bar{u}}{u_\tau} = \frac{1}{\kappa} \ln\left(\frac{y}{\delta}\right) + B \quad (2.5)$$

Here, κ and A are constants, and B depends on the flow geometry under investigation. Coles (1962) reported suitable values of $\kappa = 0.41$ and $A = 5.0$.

In literature, one of the paths to understanding turbulent flows is employing statistical methods based on the mean and standard deviations of the fluctuating flow quantities. This method is referred to as Reynolds decomposition, where in a turbulent flow, an instantaneous quantity (u) can be split into an average (\bar{u}) and a fluctuation (u'). Reynolds decomposition, when applied to the Navier-Stokes equations, gives rise to the Reynolds-averaged Navier–Stokes Equations. For more theoretical analysis of the Reynolds decomposition to the governing equations of fluid flow, refer [Schlichting and Kestin \(1961\)](#) or [Nieuwstadt et al. \(2016\)](#). From the decomposed equations, the energy budget of the mean flow and the turbulent fluctuations can be obtained, providing insight into the turbulence energy cascade ([Nieuwstadt et al. \(2016\)](#)). For wall-bounded turbulent flows in literature, results are reported in terms of the inner region scaled velocity profile, the Reynolds stresses and the turbulent kinetic energy (TKE) budget. The results discussed in the thesis will employ these characteristic plots to understand and quantify the effect of the different control techniques. [Figure 2.4\(a\)](#) reports the near-wall scaled velocity profile obtained by employing the near-wall scaling for two different Reynolds numbers (Re_τ). The Reynolds number referred to in [Figure 2.4\(a\)](#) is defined as the friction Reynolds number $Re_\tau = u_\tau h / \nu$ (where the length scale can be the channel half width or the boundary layer thickness); Re_τ denotes the ratio of the outer to the inner layer thickness. In addition, it emphasises the disparity between the two scales (i.e. inner and outer) and the diversity of the intermediate and interacting scales ([Gad-el Hak and Bandyopadhyay, 1994](#)).

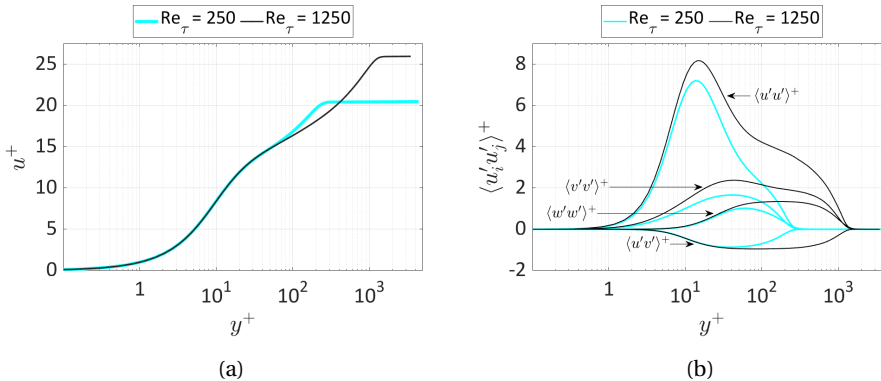


Figure 2.4: Inner scaled velocity profile (a) and Reynolds stresses distribution (b) from the DNS simulations of turbulent boundary layer flow by [Schlatter and Örlü \(2010\)](#) at Re_τ of 250 and 1250.

The regions of the flow illustrated in Figure 2.3 and which can be observed in Figure 2.4(a) are the

- Viscous sublayer ($y^+ < 5$): The viscous sublayer can be identified as the region close to the wall where the mean velocity profile follows $u^+ = y^+$. This behaviour in the viscous layer enables the determination of the skin-friction drag from direct velocity measurements near the wall.
- Buffer layer ($5 < y^+ < 30$): The intermediate region between the logarithmic and viscous sublayer is referred to as the buffer layer. It is in this region that both the viscous stress and the turbulence shear stress are important and where the peak production and dissipation of turbulent kinetic energy occurs (Gad-el Hak and Bandyopadhyay (1994)). This can be observed in Figure 2.4(b) and 2.5.
- Logarithmic layer ($y^+ > 30$): in this region, the velocity profile is logarithmic and is a fundamental property of the turbulent velocity profile near a solid wall.
- Wake region ($y/\delta > 0.1$): corresponds to the region close to the edge of the boundary layer where the energy responsible for the turbulent energy cascade is derived from the freestream.

From the Reynolds stress profiles shown in Figure 2.4(b), it is clear that the streamwise Reynolds stress is dominant. This production of the Reynolds stress is directly linked with the mixing in the boundary layer flow due to the vortical motions. Figure 2.5 shows the budget of turbulent kinetic energy. It is important to note that the energy for the TKE production is derived from the mean flow. The Reynolds number encountered in many practical applications are typically orders of magnitude higher than those studied through DNS and experiments. The effect of the Reynolds number can be observed in Figure 2.4(a) and 2.4(b). A direct consequence of the Re_τ is the increase in the range of scales in the flow. And the increase in the energy content in the outer regions of the flow.

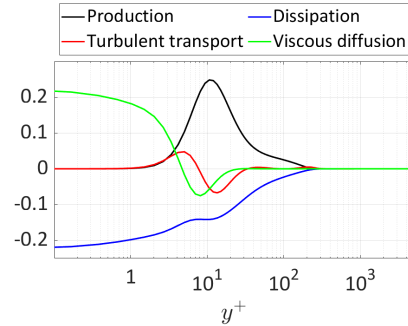


Figure 2.5: Inner scaled TKE budget from the DNS simulations of Schlatter and Örlü (2010) at Re_τ of 250.

The statistical representation of the TBL dynamics discussed above provides a comprehensive understanding of the flow. However, it is unclear how to draw the connections between the observed statistics and the underlying structure in the flow. In addition, the study of structure in the flow can aid in a better understanding of the desired data from statistics. For example, it is now well understood in the turbulence community that wall-bounded turbulent shear flows are populated by recurring, statistically significant features termed 'Coherent Structures'. [Robinson \(1991\)](#) defined these structures as '*a three-dimensional region of the flow over which at least one fundamental flow variable (velocity component, density, temperature, etc.) exhibits significant correlation with itself or with another variable over a range of space and/or time that is significantly larger than the smallest local scales of the flow*'. The topic of coherent structures has been reviewed periodically by [Kline and Robinson \(1990\)](#), [Robinson \(1991\)](#), [Panton \(2001\)](#), [Adrian \(2007\)](#), and [Wallace \(2012\)](#).

2.1.2. NEAR-WALL STRUCTURES

Early visualization experiments by [Kline et al. \(1967\)](#) using small hydrogen bubbles showed that the boundary layer in the near wall region ($y^+ < 30$) is organized into narrow streaks of high and low-speed fluid elongated in the streamwise direction. Figure 2.6 is a timeline image showing five low-speed streaks (labelled 1 to 5) with the hydrogen bubble wire at $y^+ = 20$ from the experimental works of [Jiang et al. \(2020\)](#). The average spacing of neighbouring low-speed streaks is 100 wall units and is well-accepted in the literature. [Corino and Brodkey \(1969\)](#) performed pipe flow experiments where the low-speed regions were observed to erupt outward from the wall. The term '*ejections*' was given to such events. Similarly, the ejection event was accompanied by a coordinated motion of high-speed flow toward the wall and termed '*sweeps*'. The occurrence of such events indicated the presence of a vortex principally oriented in the streamwise direction.

The observations of ejection and sweep events, [Wallace et al. \(1972\)](#) imple-

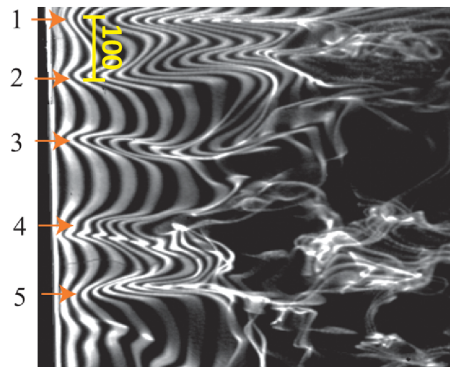


Figure 2.6: (a) Hydrogen bubble visualization of low-speed streaks in a turbulent boundary layers in the x - z plane at $y^+ = 20$ ([Jiang et al., 2020](#)), a yellow bar on the image indicates the physical scale in viscous lengths $\frac{\nu}{u_\tau}$.

mented a '*quadrant analysis*' of the velocity fluctuations in a turbulent channel flow. The principle was based on the classification of the streamwise and wall-normal velocity fluctuations according to their signs, i.e. Q1 ($+u'$, $+v'$), Q2 ($-u'$, $+v'$), Q3 ($-u'$, $-v'$) and Q4 ($+u'$, $-v'$). Wallace and Brodkey (1977) related the quadrant decomposition to the joint probability density distribution, which showed that the velocity fluctuations spend more time in the 2nd and 4th quadrants of the $u' - v'$ plane so that the average of u' times v' is negative.

2.1.3. STRUCTURES IN THE LOGARITHMIC REGION

Head and Bandyopadhyay (1981) used smoke flow visualizations to report the structures in the logarithmic region of the boundary layer. Laser sheets inclined at 45° upstream and downstream were used to observe structures that resembled hairpin-like shapes that existed in abundance over a range of Reynolds numbers. Based on the observations made by Head and Bandyopadhyay (1981), Perry and Chong (1982) proposed a physical model of the boundary layer structure, which was stated to arise out of the sheets of spanwise vorticity just above the wall. The near-wall layer was imagined to be a forest of hairpin vortices and was modelled with simplified shapes in a hierarchy of scales above the wall but attached to it.

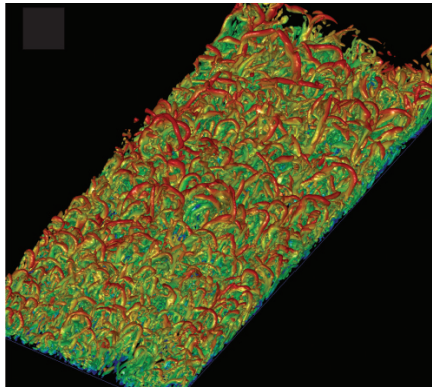


Figure 2.7: Hairpin shaped structures observed in the instantaneous velocity field from Direct Numerical Simulations of TBL by Wu and Moin (2009).

The advent of DNS simulations of wall-bounded turbulent flow and planar PIV enabled further investigation into the structure of turbulence (refer Figure 2.7). The first DNS channel flow simulations by Kim et al. (1987) plotted vorticity lines in the vicinity of the ejection-type Reynolds stress event and showed a bundle of vorticity lines with the general shape of a hairpin vortex. In addition, the authors employed flow visualizations by introducing virtual flow markers that mimicked the effect of hydrogen bubbles, and the near-wall low-speed streaks

were identified, showing that the data had all the characteristics of the physical flows.

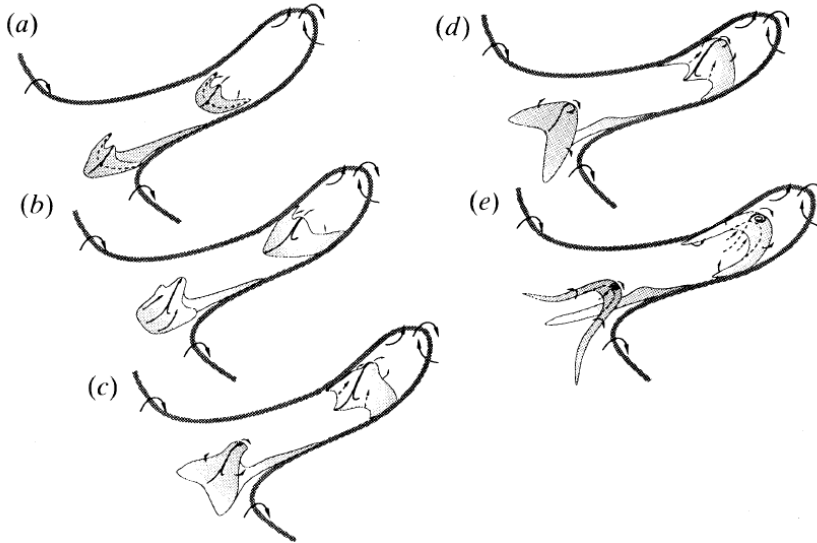


Figure 2.8: Hairpin auto-generation process illustrated by [Smith et al. \(1991\)](#) (a) The onset of interaction: sharp, crescent-shaped ridge develops in the the induced pressure gradient near the surface is adverse. (b) Rapid outward movement erupting ridge which contains concentrated vorticity. (c) The erupting sheet starts Partial roll-over reached. (e) Complete generation of secondary hairpin vortex.

[Smith et al. \(1991\)](#) reported a theoretical analysis of a mechanism to explain the creation of consecutive hairpins, and visualizations of the spanwise vorticity fields in a channel flow with PIV showed a vorticity pattern consistent with near-wall hairpins (illustrated in Figure 2.8). [Bernard et al. \(1993\)](#) reported through their channel flow simulations that the vortices in the near-wall region were principally oriented in the streamwise direction with both positive and negative sense of rotation, which can be thought of as the legs of these hairpins. Many numerical and experimental studies highlighted the association of the vortices with the sweep and ejection events. However, a self-sustaining cycle was proposed, where the near-wall streaks are created by the streamwise vortices and become unstable and wavy with time. The instability in the streaks stretches the streamwise vorticity, which gives rise to new vortices, and the autonomous cycle is sustained ([Hamilton et al. \(1995\)](#), [Jeong et al. \(1997\)](#), [Jiménez and Pinelli \(1999\)](#)). In the following years, the availability of high-resolution PIV data critically complemented the DNS data to allow measurements at higher Reynolds number.

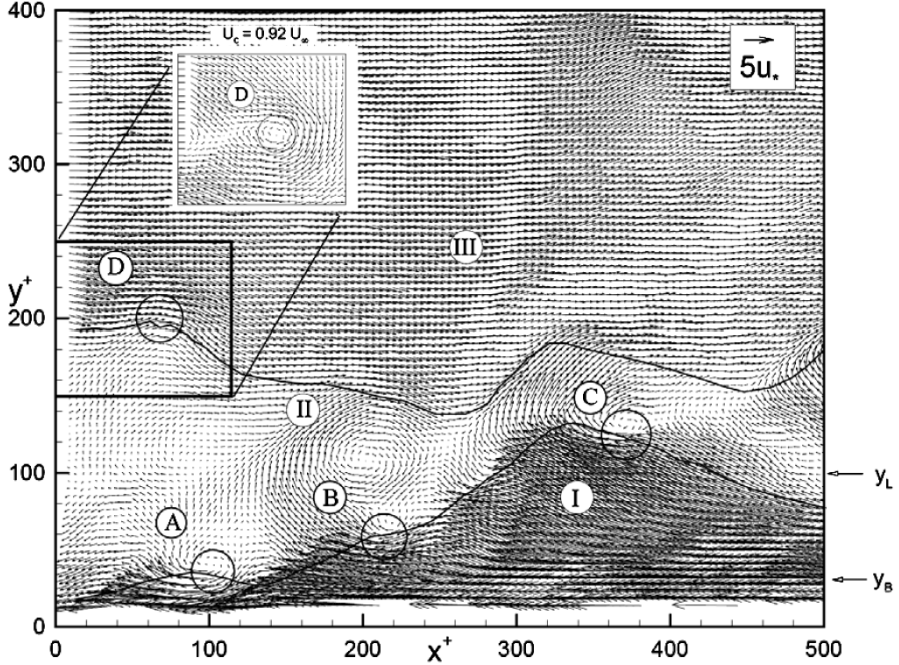


Figure 2.9: Hairpin vortex signatures in a PIV measurement of flow in the streamwise-wall-normal plane of a turbulent boundary layer, $Re_\theta = 930$. The heads of the hairpins are labelled A, B, C, and D. Zones of uniform momentum are labelled I, II, and III. The reference frame for the vectors is translating at 80% of the free-stream velocity (From [Adrian et al. \(2000\)](#)).

Adrian and co-workers PIV in several studies to investigate many aspects of the boundary layer structure. [Adrian et al. \(2000\)](#) performed high-speed planar-PIV measurements. One of the study's conclusions was that hairpin vortices occur in packets. These hairpins begin in or above the buffer layer, similar to the packets created by the auto-generation mechanism (refer to Figure 2.8) reported by [Smith et al. \(1991\)](#) and [Zhou et al. \(1996\)](#). All the individual hairpins were observed to travel with nearly equal velocities with small dispersion in their velocity. During the auto-generation process, new quasi-streamwise vortices are also generated close to the wall ([Adrian \(2007\)](#)). The packets of hairpins were experimentally shown to contribute significantly to the Reynolds shear stress by [Ganapathisubramani et al. \(2003\)](#). [Jodai and Elsinga \(2016\)](#) performed time-resolved tomographic PIV measurements in a turbulent boundary layer and quantified the hairpin auto-generation time (t_{auto}^+) to be 30 near wall scaled units (refer to Figure 2.10).

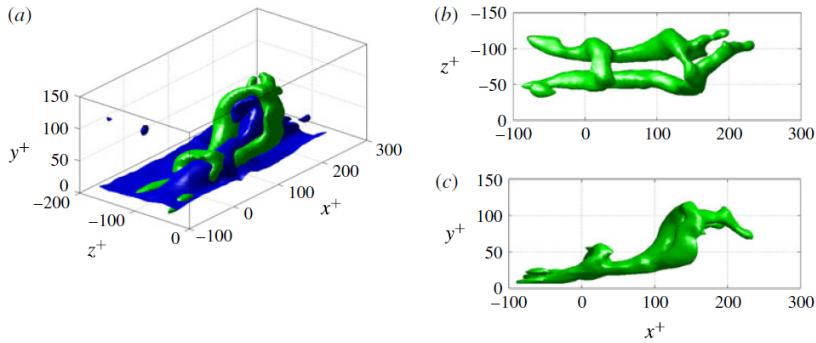


Figure 2.10: A hairpin packet in oblique (a), top (b) and side (c) views. Vortices (green) are visualized using swirling strength ($0.08 u_{\tau}^2/\nu$). In (a) the blue surface indicates a streamwise velocity of $14u_{\tau}$ by [Jodai and Elsinga \(2016\)](#).

2.1.4. LARGE AND VERY-LARGE SCALE STRUCTURES

A more recent observation of structure in TBLs is called very large-scale motions (VLSMs). [Kim and Adrian \(1999\)](#), through their pipe flow measurements, observed structures of uniform streamwise momentum, which are present in the logarithmic and outer region of the boundary layer and extended by 12-14 times the radius of the pipe. Similarly, [Hutchins and Marusic \(2007\)](#) observed these structures in the TBL, which extended up to 20δ in the streamwise direction. Their study concluded that the contribution of the streamwise velocity fluctuation intensities from these VLSMs increased with the Reynolds numbers due to the scale separation. Therefore, most TKE production is from the outer region of the flow at a large Reynolds number, as observed in [Figure 2.4\(a\)](#), where the contribution from the outer regions to the Reynolds stresses increases with the Reynolds number.

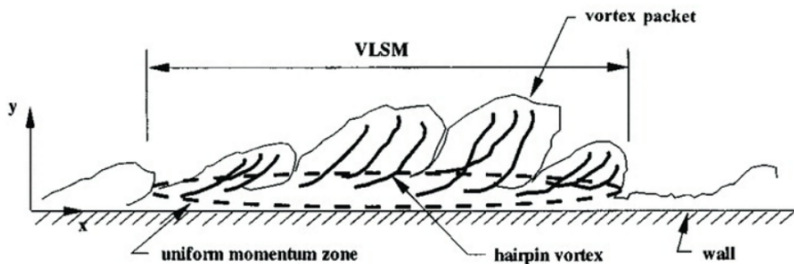


Figure 2.11: A schematic of VLSM, forming from packets of hairpin vortices adapted from [Kim \(2012\)](#).

Measurements in a laboratory boundary layer with $Re_\tau = 14,380$ with hot-wire rakes in the wall parallel plane at $y/\delta = 0.15$ highlight negative streamwise fluctuations indicating VLSMs. It has been hypothesized in the literature that hairpin vortices auto-generate and align coherently in groups to form packets, and the packets themselves also align to form VLSMs as illustrated in Figure 2.11 (Kim, 2012). It is, however, essential to note that VLSMs are relevant in high Reynolds number flows and exist in the logarithmic and outer region of the TBL.

The coherent structures discussed, i.e. (streaks, quasi-streamwise vortices, hairpin vortices, hairpin packets and VLSMs) are some of the features that contribute to the turbulent boundary layer flow dynamics. Therefore, the mechanism of near-wall flow control techniques focuses on inhibiting the structures close to the wall to limit the exchange of momentum and as a result obtain skin-friction reductions. The following section will introduce some near-wall control techniques while concisely reviewing the methods investigated in the current research.

2.2. SKIN-FRICTION REDUCTION TECHNIQUES

The techniques used for near-wall skin-friction control can be classified as active and passive. Active techniques involves the addition of auxiliary energy into the flow. Whereas passive techniques require no energy input into the flow. A variety of techniques have been proposed and studied in literature. Some of the methods include

- Riblets: These are passive skin-friction control devices consisting of longitudinal grooves on the surface. The features of the riblets are determined by their height, spacing periodicity, spacing and shape. Results in the literature report that riblets can obtain drag reduction in the order of 7-10%. Wilkinson and Lazos (1988) reported that a maximum reduction of 8% was realizable with triangular riblets with $s^+ = h^+ = 15$, where s^+ is the dimensionless spacing and h^+ is the dimensionless riblet height. Choi (1989) stated that the riblets act as longitudinal fences that restrict the spanwise movement of the quasi-streamwise vortices, leading to premature bursts of shorter duration and reduced intensity. An alternate explanation states that the reductions are obtained due to viscous interaction due to the low speed, quiescent flow within the riblet valley (Djenidi et al., 1994; Lim and Kim, 2004).
- Opposition flow control: This technique consists of measuring wall-normal (or spanwise) velocity at the detection plane and opposing it at the wall and is reported to give up to 20% in friction drag reduction (Choi et al.,

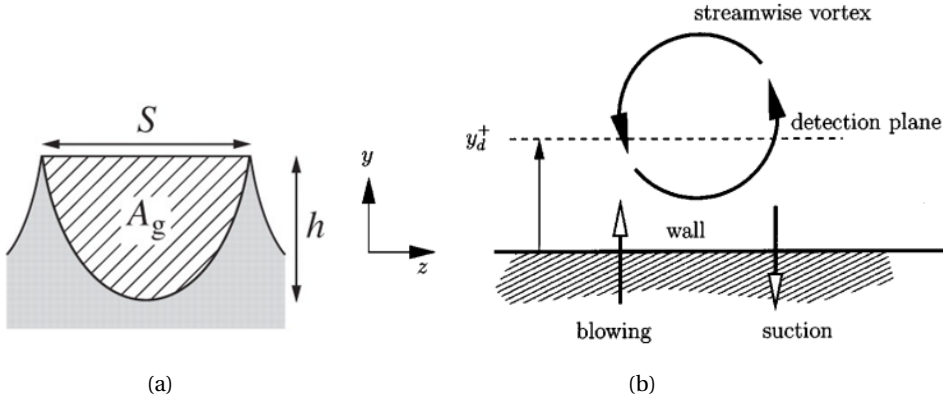


Figure 2.12: Illustration of passive skin-friction reduction technique like Riblets (a) and the active technique of opposition flow control (b) adapted from the works of [García-Mayoral and Jiménez \(2011\)](#).

1994). Early investigations focused on the detection and control of buffer layer structures where the control technique was impracticable due to the small spatial and temporal scales. The control technique is currently being investigated to control the structures at large Reynolds numbers in the logarithmic region where the structures have a longer lifetime and can be detected and controlled. [Pastor et al. \(2020\)](#) showed through numerical simulations that a single actuator located above $y^+ = 50$ could reduce drag by 3-4% by opposing the vertical motions near the wall.

The reader can refer to the articles cited above for a more in-depth review of these techniques. However, the current research falls under the purview of transverse wall oscillation. As the name suggests, these active techniques introduce wall-parallel oscillatory motion. The most straightforward configuration is the spanwise wall oscillations, where the wall oscillates in time in the spanwise direction. Introducing the streamwise component to purely spanwise oscillation gives rise to the method of travelling waves. The two techniques arise from the motion of the wall. Still, to overcome the disadvantages of the mechanical system, plasma actuators are investigated as a surrogate for spanwise wall oscillation. Another interesting version of the mechanical system is that of flush-mounted rotating discs. The following discussion focuses on the four techniques mentioned to highlight state of the art and provide an overview of the works performed and the challenges yet to be addressed. For a more elaborate discussion, the readers can refer to the review article by [Ricco et al. \(2021\)](#).

2.2.1. SPANWISE WALL OSCILLATIONS

Spanwise wall oscillation is an active flow control technique that employs spanwise sinusoidal motion of the wall/surface over which a TBL is present (shown in Figure 2.13). The first reported investigation of spanwise wall oscillations (SWO) was performed by Jung et al. (1992). The authors were motivated by the earlier works by Bradshaw and Pontikos (1985) and Driver and Hebbar (1987), who indicated that the imposition of a sudden spanwise flow in a 2-dimensional turbulent boundary layer flow resulted in the reduction of the turbulent activity/Reynolds stress near the wall.

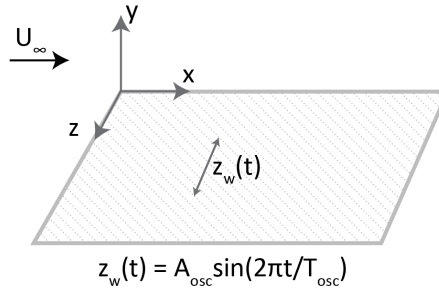


Figure 2.13: Illustration of the concept of spanwise wall oscillation where $z_w(t)$ denotes the spanwise location of the plate.

The technique of spanwise wall oscillations is governed by two parameters which are the amplitude (A_{osc}) and time period (T_{osc}) of wall oscillation. In this technique, the wall oscillates in time according to the following equation.

$$z_w(t) = A_{osc} \sin\left(\frac{2\pi t}{T_{osc}}\right) \quad (2.6)$$

The parameters are represented in a non-dimensional form in literature, based on the near-wall scaling as

$$A_{osc}^+ = \frac{A_{osc} u_\tau}{\nu} \quad \text{and} \quad T_{osc}^+ = \frac{T_{osc} u_\tau^2}{\nu} \quad (2.7)$$

In addition, a derived parameter is defined as the amplitude of wall velocity $W_m^+ = \frac{\pi A_{osc}^+}{T_{osc}^+}$. Jung et al. (1992) reported a maximum drag reduction of 40% at an optimal oscillation period of $T_{osc}^+ = 100$. A drag increase was observed at $T_{osc}^+ = 500$. Laadhari et al. (1994) performed the first experimental study with 3-dimensional hotwire probes to verify the DNS results. A crank-shaft mechanism produced the desired wall oscillations, and they quantified a reduction of 36%

in the wall shear stress. [Baron and Quadrio \(1995\)](#) performed DNS simulations of channel flow at $Re_\tau = 200$. The authors quantified 40% reductions in skin-friction drag and observed that the SWO caused a shift of all turbulent quantities away from the wall and thickened the viscous sublayer. The reductions quantified in skin-friction were attributed to the thickness of the Stokes layer under optimum conditions, which caused a relative displacement of the low-speed streaks and the streamwise vortices.

[Choi et al. \(1998\)](#) reported qualitative smoke visualizations of the tilting of the streaks (in the x - z plane referred to as γ in the subsequent discussions) due to the oscillatory wall motion with a maximum reported reduction of 45%. In addition, the authors conceptualized the formation of spanwise vorticity by the periodic Stokes layer produced by the wall oscillations, caused the reduction in skin-friction. [Choi \(2002\)](#) performed a large set of channel flow simulations, and observed that the maximum drag reductions of 44.5%, 39.2% and 34.1% were obtained at a Reynolds number of 100, 200 and 400 corresponding to $T_{osc}^+ = 100$ and $W_m^+ = 20$.

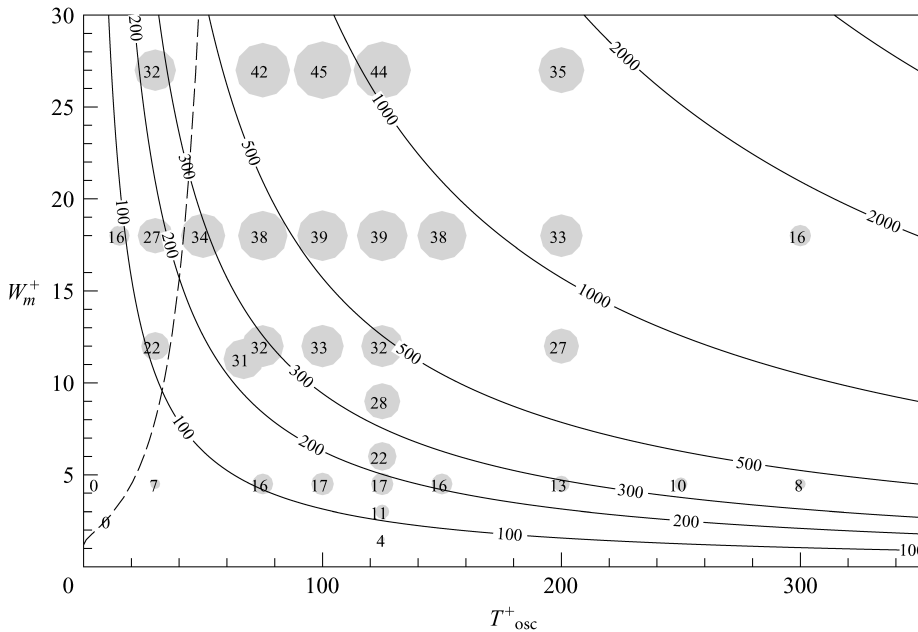


Figure 2.14: Map of friction DR(%) plotted against the time period (T_{osc}^+) and velocity (W_m^+) of wall oscillation from the DNS simulations of [Quadrio and Ricco \(2004\)](#).

Although both DNS and experiments provided evidence that spanwise oscillation can lead to a reduction in skin-friction drag, there are many quantitative

Table 2.1: Overview of the literature on spanwise wall oscillations undertaken using numerical and experimental methods.

Experiments					
Authors	Geometry/ Fluid	Reynolds number (Re_θ)	A_{osc}^+	T_{osc}^+	Max drag reductions (%)
Laadhari et al. (1994)	TBL/ Air	950	160	100	36
Trujillo et al. (1997)	TBL/ Water	1400	360	70	27
Choi et al. (1998)	TBL/ Air	1190	50mm	0.2s	45
Ricco and Wu (2004)	TBL/ Water	500- 1400	240	42	32
Gouder et al. (2013)	TBL/ Air	2430	130	90	11.5
Gatti et al. (2015)	Duct/ Air	4520- 15140	3.2	69	2.4
Kempaiah et al. (2020)	TBL/ Air	980	100	94-700	15
Numerical Simulations					
Authors		Reynolds number (Re_τ)	W_m^+	T_{osc}^+	Max drag reduction (%)
Jung et al. (1992)		200	12	25-500	40
Baron and Quadrio (1995)		200	4, 9, 13, 17	100	40
Choi (2002)		100	1,5,10,20	1-200	45.4
		200	5, 10, 20	50-200	39.2
		400	5, 10, 20	50-200	34.1
Quadrio and Ricco (2003)		200	3-27	50-200	50
Quadrio and Ricco (2004)		200	1.5-27	5-750	44.7
Ricco and Quadrio (2008)		200	300	125	36
		400	12		28.1
Touber and Leschziner (2012)		200	12	100, 200	38
		500			32
		1000			29
Yakeno et al. (2014)		150	3.0, 7.0, 12.0	16, 50, 75, 125, 250, 500	42.8
Agostini et al. (2014)		1000	12	100, 200	29
Yao et al. (2019)		200	12	100	35.3
		497			28
		1000			25.9
		1998			23.2
Yuan et al. (2019)		200	3, 6, 12, 18	50, 100, 200	41.6
Yang and Hwang (2019)		800	12	100	25

discrepancies when comparing the maximum drag reduction and the underlying mechanism. [Quadrio and Ricco \(2004\)](#) performed an additional 37 DNS simulations, and a comprehensive drag reduction map was generated (shown in Figure 2.14). From Figure 2.14, it can be seen that the optimum period (T_{osc}^+) at a fixed W_m^+ lies between 100-125. In addition, a net energy savings of 7.3% was obtained at the an $Re_\tau = 200$. Experimental investigations in a water tunnel by [Ricco and Wu \(2004\)](#) reported that the flow over an oscillating wall readjusted to the unforced conditions at 2δ downstream of the plate. In contrast, the flow required a longer length (3δ) to fully establish the drag reduction conditions. Table 2.1 reports the works performed employing spanwise wall oscillations both experimentally and numerically. [Touber and Leschziner \(2012\)](#) performed channel flow studies using DNS at $Re_\tau = 500$ to better understand the root cause of the drag reductions. Through their work, they identified that the streaks in the near wall region did not realign periodically in response to the wall oscillation. Rather, they weakened when the Stokes strain varied rapidly and strengthened when the strain changed at a low rate.

[Gouder et al. \(2013\)](#) successfully employed an electroactive polymer sheet with an electromagnetic actuator to produce SWO. Through this actuation method, maximum reductions of 16% were quantified by using a drag balance. [Gatti et al. \(2015\)](#) experimentally investigated the drag reductions by spanwise wall oscillations through airflow in a duct. An electroactive polymer surface was used in the duct to produce the wall oscillations, and reductions of 2.4% were measured.

[Agostini et al. \(2014\)](#) examined phase-averaged statistics, including Reynolds stress budgets at sub optimal actuation period of $T_{osc}^+ = 200$. The authors confirm the mechanism introduced by [Touber and Leschziner \(2012\)](#) where the drag-reduction is linked to the rate of change in the Stokes strain in the upper region of the viscous sublayer. [Yakeno et al. \(2014\)](#) proposed an empirical model that correlated the drag reduction linearly to the spanwise shear at two wall normal positions at $y^+ = 10$ and $y^+ = 15$. The authors attributed the drag reduction effect to the suppression of the Q2 (ejection) events below the optimal oscillation period as the spanwise shear is expected to counteract the rotation of the quasi-streamwise vortices at $y^+ = 10$ at a particular phase of the oscillation. In addition, the authors also state that the tilting of the structures in the flow, can also lead to the suppression of turbulence. At large T_{osc}^+ , the authors observe a drastic enhancement of the Q4 events which diminishes the drag reduction effect.

[Yao et al. \(2019\)](#) reported a decrease in the optimal time period of oscillation with an increase in the Reynolds number of the flow through their channel flow simulations. [Yuan et al. \(2019\)](#) concluded that drag reduction is linked to the increase in turbulence-energy dissipation. [Dong et al. \(2019\)](#) reported that wall oscillations reduce pressure fluctuation and decrease skin-friction drag.

2.2.2. TRAVELLING WAVES

The flow control strategy of travelling waves (TW) is a more complex form of actuation in comparison to SWO. The actuation can be understood as streamwise travelling waves of spanwise velocity and can be described with the following equation.

$$W(x, t) = W_m \cos(k_x x - \omega t) \quad (2.8)$$

Where $W(x, t)$ is the spanwise velocity, similar to SWO the parameters that govern the TW are the streamwise wavenumber (k_x , related to the wavelength $\lambda_x = \frac{2\pi}{k_x}$) and the frequency (ω , related to $T_{osc} = \frac{2\pi}{\omega}$). It is important to note that SWO are a subset of this concept and corresponds to the condition when $k_x = 0$. For $\omega = 0$ the forcing corresponds to a standing wave (SW).

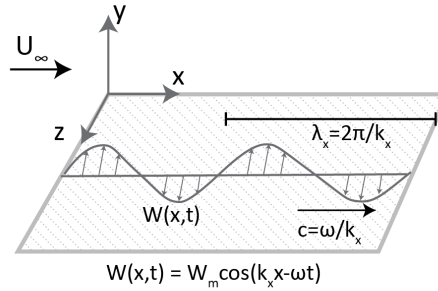


Figure 2.15: Illustration of the concept of streamwise travelling waves of spanwise velocity, where k_x denotes the streamwise wavenumber, ω and W_m are the frequency and maximum velocity.

Viotti et al. (2009) performed DNS simulations of a channel flow with a standing wave in the range of $\lambda_x^+ = 200 - 3000$, $W_m^+ = 12$ and it was reported that optimal reductions of 45% were observed for $\lambda_x^+ = 1200$. A connection was made between the optimal time period in SWO of $T_{osc}^+ = 100$ with $\lambda_x^+ = 1200$ based on the convection velocity ($u_c^+ = 10$) of the structure in the buffer layer. Yakeno et al. (2009) confirmed the connection between the T_{osc}^+ and λ_x^+ by performing DNS simulations of both a standing wave and pure SWO. In addition, it was observed the maximum drag reductions of 35% (SWO) and 45% (standing wave) were obtained.

Quadrio et al. (2009) used DNS to investigate channel flow at $Re_\tau = 200$ with $W_m^+ = 12$ and wide range of frequency and wavelength values to produce a map of drag reductions (250 simulations were performed, refer to Figure 2.16). The list of relevant literature for TW is reported in Table 2.2. Maximum reductions

of 48% were obtained at $T_{osc}^+ = 350$ and $\lambda_x^+ = 750$. The maximum reductions obtained through TW is higher than that obtained from SWO (34%) and SW (45%). An observation from the results were that backward travelling waves resulted in drag reductions at all wave speeds. However, maximum increase in drag was observed in the forward travelling condition at a wave speed matching the convection velocity of the near wall turbulent structures ($u_c^+ = 10$).

Table 2.2: Overview of the literature on standing and travelling waves undertaken using numerical and experimental methods.

Experiments						
Authors	Geometry/ Fluid	Reynolds number	W_m^+	λ_x^+	T^+	Max D.R (%)
Auteri et al. (2010)	Pipe flow/ water	175	-	511, 766, 1532	-	33
Bird et al. (2018)	TBL/Air	1225	-	910	100	21.5
Marusic et al. (2021)	TBL/Air	1000	0.27	4500	140	29
Numerical Simulations						
Authors	Forcing	Reynolds number	W_m^+	λ_x^+	T^+	Max D.R (%)
Viotti et al. (2009)	SW	200	1-27	200- 500	-	45
Quadrio et al. (2009)	TW	200	12	750	350	48
Yakeno et al. (2009)	SW	150	1-10	1000	-	55
	SWO		1-10	-	100	35
Quadrio and Ricco (2011)	TW	200	12	525	140	45
Gatti and Quadrio (2013)	TW	199	12	1250	350	49
	TW	951	12	450	150	42
	TW	2108	12	420	150	37
Hurst et al. (2014)	TW	200	12	800	300	50
	TW	400	12	800	300	44
	TW	800	12	800	300	40
Gatti and Quadrio (2016)	TW	199	12	997	322	50
	TW	948	12	322	125	39
Gatti et al. (2018)	TW	200	7	630	260	36.4
	TW	1000	7	630	260	26.6

The first experimental investigation of travelling waves was undertaken by [Auteri et al. \(2010\)](#) in a pipe flow setup, where individual sections were actuated to obtain the desired forcing conditions. The maximum drag reductions observed (33%) were lower than that obtained by [Quadrio et al. \(2009\)](#). The dif-

ferences were ascribed to the effect of spatial transience. DNS investigation at higher Reynolds numbers of 2100 were performed by [Gatti and Quadrio \(2013\)](#). The results indicated that the drag reduction decreased with an increase in the Reynolds number. In addition, the optimal parameters increased towards larger wavenumbers and frequencies with an increase in the Reynolds number. [Hurst et al. \(2014\)](#) reported that the increase in Reynolds affected the spanwise wall oscillation more than purely spatial actuation.

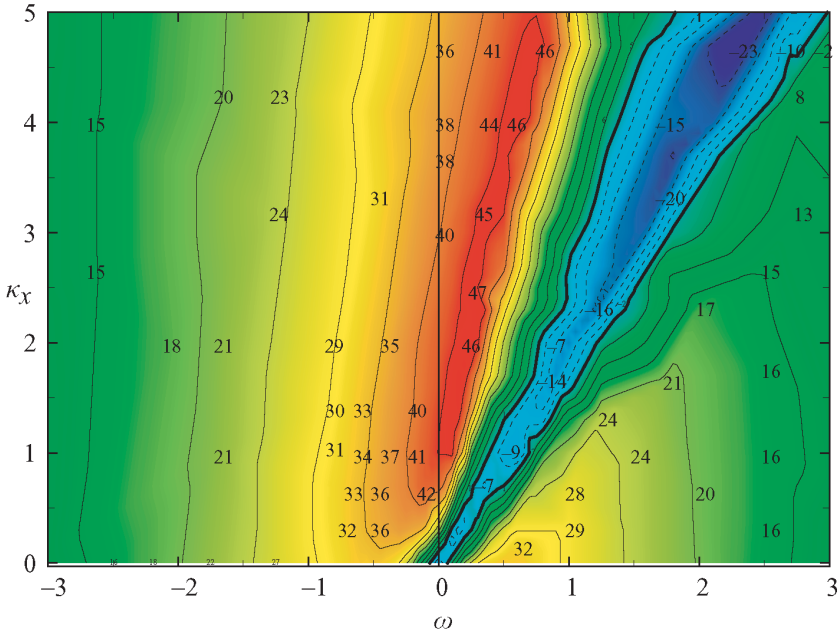


Figure 2.16: Map of friction DR (%) in the $\omega - \kappa_x$ plane from the DNS simulations of [Quadrio et al. \(2009\)](#).

[Bird et al. \(2018\)](#) employed a Kagome lattice covered with a thin smooth layer of silicon rubber to generate forward and backward travelling waves of spanwise wall displacement. A maximum drag reduction of 21.5% was measured for backward travelling wave. The results obtained were in agreement with [Quadrio et al. \(2009\)](#).

Recently, [Marusic et al. \(2021\)](#) performed experiments with upstream travelling waves in a TBL. The results indicated that effective drag reduction at high Reynolds number conditions can be achieved with wall-oscillation frequencies on the order of large, outer-scaled flow features (refer to [Figure 2.17\(a\)](#) and [2.17\(b\)](#)). The results have opened up opportunities to scale to larger and more representative Reynolds numbers.

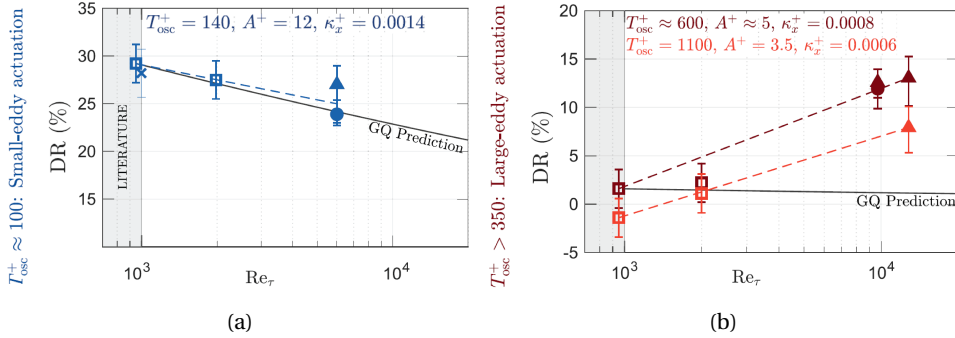


Figure 2.17: Trends of drag reductions (%) for near-wall control (small-eddy actuation, a) and VLSM control (large-eddy actuation) where the DR margin decreases with Re_τ for near-wall control and increases for the latter (Marusic et al., 2021).

2.2.3. PLASMA ACTUATORS

Plasma actuators are active flow-control device that produce a discharge-based body force in the vicinity of the wall (Kriegseis et al. (2016)). Plasma actuator have been employed for skin-friction reduction studies from the early works of Wilkison et al. (2003). The advantages of these actuators include low power consumption, lack of moving parts and their associated robustness. The actuators are employed with the aim of controlling the near-wall turbulence generation, while avoiding the mechanical motion of the surface as in SWO. The most popular type of plasma actuators for skin-friction reduction effects is the Di-electric Barrier Discharge (DBD) actuator. It works on the principle of ionization of air using high voltage AC current. In these actuators one or both electrodes are encapsulated in a dielectric insulating material. The dielectric allows the accumulation of the ionized gas in the vicinity of the exposed electrode. The momentum transfer occurs due to the collision of the heavy plasma species (ions) and the neutral air (Likhanskii et al., 2007). Moreau (2007), Corke et al. (2010) and Kotsonis (2015) provide a comprehensive review of the operation, diagnostics and characterization of plasma actuators.

The plasma force is analogous to a body force that is applied in the flow domain. Numerically a variety of body force configurations have been used to assess the drag reduction benefits. However, the experimental implementation of these techniques possesses its own challenges. Wilkison et al. (2003) reported that the plasma jet obtained in the experiments could not be confined in the near wall region and found it undesirable for surrogating the wall oscillations.

Jukes et al. (2004), performed measurements over a single symmetric bi-directional plasma forcing in quiescent air. The results of the characterisation reported that

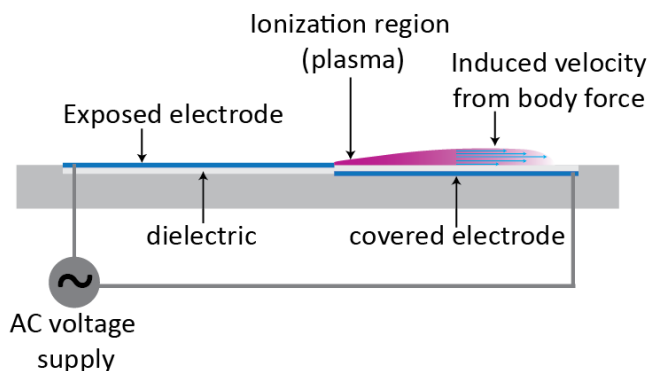


Figure 2.18: The geometric configuration and operation of the plasma actuator (adapted from Kotsonis et al. (2011)).

maximum velocities of 2.1 m/s could be obtained with a forcing corresponding to an output in the form of an alternating polarity pulses of 4kV amplitude. Jukes et al. (2006), then performed measurements of the characterized array discussed earlier in the form of an oscillatory plasma forcing using two opposing sets of plasma actuators, which produced co-rotating streamwise vortices in the inner region of the boundary layer. Using this approach skin-friction reductions of 45% were obtained downstream of the array and the streamwise vortices were hypothesized to interact with the naturally occurring quasi streamwise vortices and disrupting the turbulence production cycle.

A parametric investigation of a single electrode was undertaken by Thomas et al. (2009) for flow control applications at high Reynolds numbers. Through the study it was found that actuators constructed with thick dielectric material of low dielectric constant produce a body force that is an order of magnitude larger than that obtained by Kapton-based actuators used in the earlier studies. Whalley and Choi (2014), investigated an array of plasma actuators in two different forcing configurations which were uni-direction travelling wave and bi-directional forcing similar to Jukes et al. (2006). In the uni-directional case, the actuator creates a single streamwise vortex in sequence, which moves as a single vortex engulfing the neighbouring vortices from the previous phases. Whereas in the bi-directional forcing as in Jukes et al. (2006) leads to a complex interaction of co and counter rotating vortices. Reductions in streamwise velocity by 10% and 20% are observed at a $y^+ = 20$ but drag reductions have not been reported.

Table 2.3: Overview of literature employing plasma actuators for skin-friction reductions.

Author	Actuation direction /fluid	Reynolds number	Electrode parameters		Induced flow parameters		Max D.R (%)
			Physical dimensions (exposed-covered-spacing [mm])	Input signal	Thickness of jet [mm]	Velocity [m/s]	
Jukes et al (2004)	Characterization of single symmetri bi-directional plasma forcing in quiescent air	NA		4kV	4	2.1	NA
Jukes et al (2006)	Two opposing sets of asymmetric plasma actuators	380	4 (spacing)	3.3kV	4	1.2	45%
Thomas et al (2009)	Characterization of a single DBD plasma actuator	NA	25.4 - 50.8 (exposed-covered)	5- 35kV	10	1.8	NA
Whalley et al (2011)	Drag reduction studies for uni-directional travelling wave and bi-direction forcing	435	2.5 - 6 (exposed-covered)	7kV	50y ⁺	15-20u ⁺	NA
Mahfoze et al (2017)	DNS of plasma forcing	180	8 (spacing)	Suzen and Huang model	8	4	33%
Hehner et al (2019, 2020)	Beat frequency concept to produce oscillaing plasma	quiescent condition	1 - 3 (exposed-covered)	3.6kV	2-3	1	NA
Altintas et al (2020)	DNS of plasma forcing	180	plasma width: 29 ⁺ spacing : 0, 35 ⁺ wall units(+)	Shyy model	5	1.6	4% for 0 ⁺ spacing 0% for 35 ⁺ spacing
Thomas et al (2019)	Experiments employing pulsed DC plasma	5000-11,600 (Re _θ)	2-16-23	4kV-8kV	5-6	1	>70% (Re _θ =5000) ~20% (Re _θ =11,600)
Cheng et al (2021)	Experiments with counter and co-rotating vortices	46000 (Re _x)	5-15-0 (counter rotating) 5-15-20 (co-rotating)	5.75kV	100-200 (y ⁺)		25% counter 20% co-rot

Mahfoze and Laizet (2017) employed DNS simulation to study the impact of the sparsity of the plasma forcing. The results highlighted the importance of the jet thickness, velocity and the chosen actuation frequency. The authors highlighted that generation of vortical structures can promote drag with an increase of upto 75%. Whereas the use of uni-directional forcing resulted in reductions up to 33%. Recently, **Thomas et al. (2019)** employed high voltage pulsed DC waveform plasma actuators to produce jets at short pulse widths of $20\mu s$. The drag reductions obtained were close to 70% through load cell measurements at large Reynolds numbers. **Altıntaş et al. (2020)** performed DNS simulations over a spatially oscillating plasma force with three configurations differentiated by the region covered by the plasma force. It is observed that as the arrays with large spanwise spacing no drag reductions are obtained. For the least spacing reductions of 15% are obtained. **Hehner et al. (2019, 2020)** introduced the beat frequency concept to produce a plasma forcing which reduced the spanwise inhomogeneity associated with a bi-directional plasma forcing. Drag reductions from the actuators have not been reported.

Starikovskiy and Aleksandrov (2021) raised queries regarding the drag reduction data obtained by **Thomas et al. (2019)** based on extrapolation of the drag reduction data to low Reynolds numbers and the sensitivity of the measurements to Electromagnetic interference which is commonly seen in DBD actuators using high voltage pulses (**Su et al., 2021**). **Cheng et al. (2021)** investigated the effect of large scale counter and co-rotating streamwise vortices at large Reynolds numbers and reported reductions in skin-friction of 20-25%. **Su et al. (2021)** characterised the performance of a pulsed-DC high voltage actuator in terms of power consumption, induced flow, thermal effect and the body force generated. The characterisation study was followed by the work of **Zong et al. (2022)**, where the interaction pulsed DC high voltage forcing in three modes i.e. uni-directional jet, steady crashing jet and spanwise oscillating jet with the TBL were investigated with stereo-PIV measurements. A model was proposed which predicts the cross-stream flow patterns and the streamwise velocity variations. The upwash and downwash effect of the plasma resulted in significant inhomogeneity in the drag reductions obtained. The configurations, forcing conditions and interpretation of plasma actuators for skin-friction reduction reported in Table 2.3 are diverse, and in some cases contradicting. In the current research, plasma actuators will be developed to surrogate the oscillating wall with the aim of obtaining skin-friction reductions.

2.2.4. ROTATING DISCS

Keefe and Keefe (1997) proposed the concept of flush-mounted rotating disc to achieve turbulent skin-friction reduction. The method was motivated by the re-

sults of the oscillating wall reported in literature. The concept of discs has its benefits in comparison to the oscillating wall as it overcomes the problem associated with the large inertial forces involved while scaling the SWO to high Reynolds numbers.

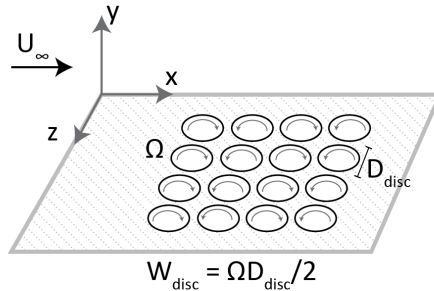


Figure 2.19: Illustration of an array of rotating discs with the governing parameters.

Ricco and Hahn (2013) performed DNS simulations of a turbulent channel flow at $Re_\tau = 180$ by an array of two streamwise aligned discs of opposite rotation. The discs were placed on both the walls of the channel. The parameters that govern the disc array are the diameter of the disc (D_{disc}) and tip velocity (W_{disc}) which can be obtained as $W_{disc} = \frac{\Omega D_{disc}}{2}$. Ω is the angular velocity of the discs. For a disc array, discs that are next to each other along the streamwise direction have opposite direction of rotation, while the direction of rotation along the rows in the z direction is the same. The non-dimensionalization is performed using near wall scaling parameters and are represented with a superscript $+$. Ricco and Hahn (2013) produced a map of drag reductions based on the two governing parameters (refer Figure 2.20(a)) similar to the map for spanwise wall oscillations (Figure 2.14, by Quadrio and Ricco (2004)). The results reported that for an optimal diameter and angular velocity a maximum drag reduction of 23% can be obtained. In addition, a drag increase of 56% was observed at small diameters and larger tip velocities. Table 2.4 shows the relevant works which investigated the concept of rotating discs for skin-friction reduction.

Table 2.4: Overview of literature on rotating discs for skin-friction reductions.

Authors	Geometry/ salient details	Reynolds number (Re_τ)	D_{disc}^+	W_{disc}^+	Max D.R. (%)
Ricco and Hahn (2013)	DNS, Channel flow Drag reduction map	180	150-1850	1.5-17	23
Koch and Kozulovic (2013, 2014)	Experimental, partially covered passively rotating discs	$u_\infty=10-50$ [m/s]	10 [cm]	0.25-2.5 [m/s]	17
Wise and Ricco (2014)	DNS, Channel flow with oscillating discs ($T_{osc}^+ = 0 - 1000$)	180	500-900	1.5-15	20
Wise et al (2014)	DNS, Channel flow to optimize the layout of discs array	180	-	-	18.5
Olivucci et al (2019)	DNS, Channel flow with combination of rotating rings, opposition control and hydrophobic surfaces	180	605	9	20
Olivucci et al (2021)	DNS, Channel flow with passively rotating disc	180	50-1200	-	5.6

The only experimental attempt was made by [Koch and Kozulovic \(2013\)](#), where partially covered passively rotating discs were used. Correlation between the freestream velocity and the disc surface was used to estimate the maximum drag reduction margin to be 17%. Following which [Wise and Ricco \(2014\)](#), replaced the rotary motion of the disc array with sinusoidal oscillatory motion. The results indicated that low frequency actuations have a potential for skin-friction reduction. The arrangement of the discs (refer Figure 2.20(c)) in the array was investigated by [Wise et al. \(2014\)](#). The authors showed that the arrangement of the discs have an influence on the drag reduction margin and observed that the mechanism responsible for drag reduction is more complex than the flow altered by SWO and TW. [Olivucci et al. \(2019\)](#) investigated a combination of rotating rings (refer Figure 2.20(b)), opposition control and hydrophobic surface to improve the drag reduction margin further. [Olivucci et al. \(2021\)](#), took forward the concept of passively rotating discs by performing DNS simulations. The array consisted of half discs and under optimum conditions total skin-friction reductions of 5.6% were obtained. The method of rotating discs has the potential to be scaled up to practical applications. [Ricco and Hahn \(2013\)](#) calculate that for representative flight conditions the required diameter is 6.7mm and rotational frequencies of 3700Hz. Similarly, for ships the suitable diameter is estimated to be 6.5 mm at rotational frequencies of 170Hz which can be achieved with the currently available motors. The underlying mechanism as mentioned by [Wise](#)

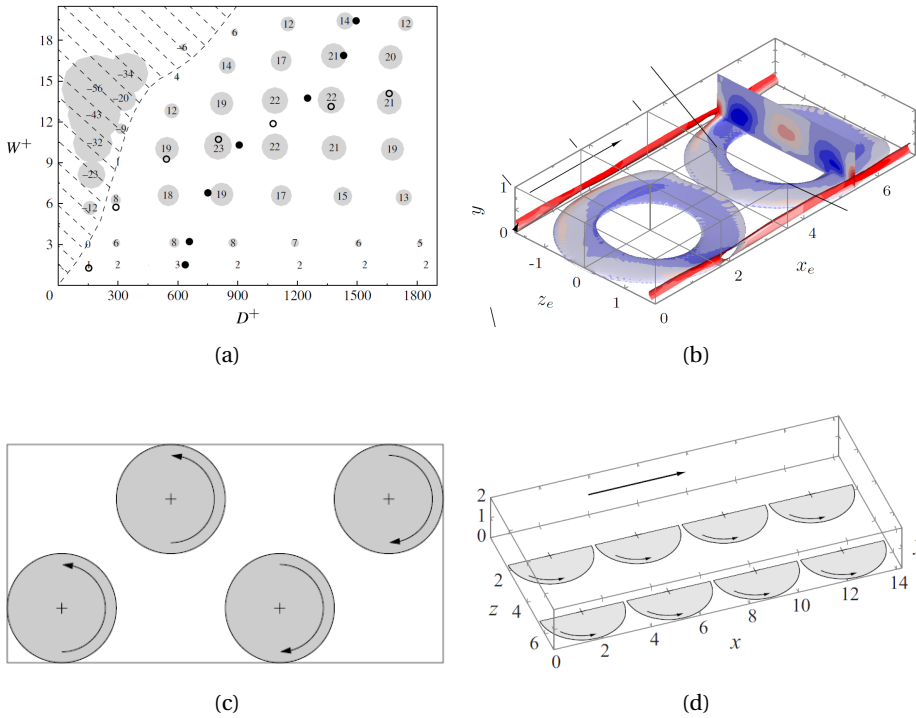


Figure 2.20: The drag reduction map as a function of the governing parameters (D_{disc}^+, W_{disc}^+) produced by Ricco and Hahn (2013); The contours of wall normal ring flow velocity (blue is negative and red is positive) produced by spinning rings (Olivucci et al., 2019); A sparsely arranged array of discs investigated by the work of Wise et al. (2014) to asses the effect of sparsity on the drag reduction margin; Schematic of the rows and columns of half discs investigated by the DNS works of Olivucci et al. (2021).

et al. (2014) is different than that of the SWO and TW concepts. Wise and Ricco (2014) state that the discs modify the flow through two distinct paths which are

- The effect of the boundary layer generated by the rotating discs.
- The effect of the quasi-steady inter-disc structures.

The effect of the rotating discs is similar to the SWO in regions where the wall velocity corresponds is purely in the spanwise direction. In addition, The quasi-steady inter-disc structures were hypothesized to behave like synthetic jets. The review of literature reveals that there is a lack of experimental investigations on the effect of an array of rotating discs on wall bounded turbulent flows.

2.3. RESEARCH QUESTIONS

At this point, motivated by the above research survey, a more detailed statement is made of the research questions investigated throughout this thesis.

1. What are the benefits and limitations of using PIV to study turbulent skin-friction reduction over an oscillating wall?
 - (a) Can we measure down to the wall to infer the skin friction over an oscillating wall?
 - (b) Can we measure 3D data over the oscillating wall in the near-wall region?
2. How should 3D data be inspected to understand the effect of wall oscillations? Does the phase of the oscillation play a role?
 - (a) Can we develop a feature detection method to identify and characterise the coherent structures?
 - (b) How does the feature detection method perform compared to conventional correlation techniques?
 - (c) Can we propose a phenomenological model highlighting the mechanism for skin-friction reduction?
3. Can the motion of the oscillating wall be surrogated by employing plasma actuators, and do the actuators produce the desired skin-friction reduction?
 - (a) What are the desired properties of a plasma actuator to produce near-wall jets that surrogate the motion of the wall?
 - (b) Does the flow topology produced by the plasma actuator differ when investigated in quiescent conditions and in the presence of a stream-wise developing turbulent boundary layer?
 - (c) Are skin-friction reductions expected when employing these actuators at representative conditions of the oscillating wall?
4. How does an array of flush-mounted rotating discs affect the flow organisation in a turbulent boundary layer?
 - (a) Can the effect of the rotation of the discs in the array be observed through the velocity measurements and the turbulent statistics from particle image velocimetry?

3

PARTICLE IMAGE VELOCIMETRY

*It is essential to have good tools,
but it is also essential that the tools
should be used in the right way.*

Wallave D. Wattles

Particle Image Velocimetry (PIV) has been extensively used in this work. The current chapter describes the working principle of PIV, followed by a discussion on the measurement chain (i.e. the procedure of obtaining images and computing the resultant velocity fields). Finally, an overview of the types of PIV systems (Planar, Stereo and Tomographic) employed in the thesis are provided. In addition, It should be noted that the details on the individual PIV setups and measurement configurations are shown in the respective chapters.

3.1. WORKING PRINCIPLE

Particle Image Velocimetry (PIV) is a non-intrusive optical flow measurement technique that is employed to measure the fluid velocity in various domains. PIV has rapidly developed from a laboratory tool employed in research facilities in the 80s to a mature tool currently used extensively in industrial environments. The working principle of PIV is based on the measurement of the displacement of small tracer particles inserted into the flow over a short time separation. The particles are illuminated by a light source (pulsed laser or LEDs) and the corresponding images are captured using a digital camera (CCD or CMOS). To evaluate the fluid velocity, the captured images are partitioned into smaller interrogation windows and the average displacement of the particles in each window is estimated using the cross-correlation operator. The general layout of a planar-PIV setup and an illustration of the particle images are provided in Figure 3.1.

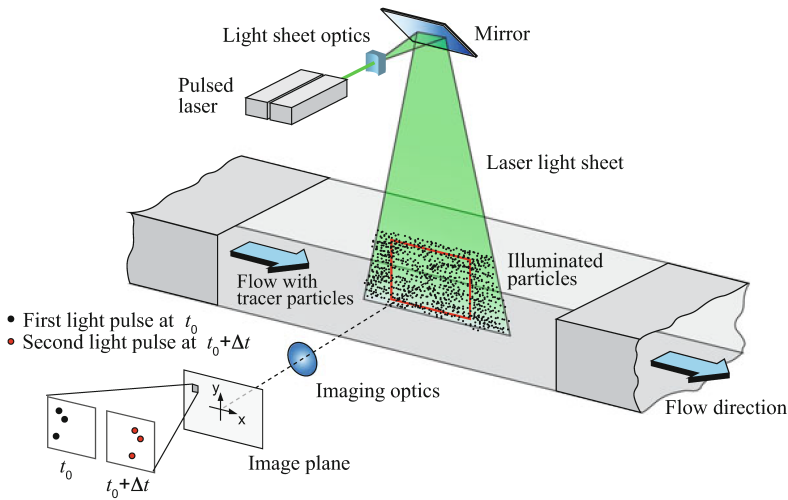


Figure 3.1: Schematic of a planar (2D2C) PIV setup. Illustration reproduced from Raffel et al. (2018).

The advantages of PIV over other flow measurement techniques like hot-wire anemometry (HWA) and Laser-Doppler anemometry (LDA) is it's the ability to provide instantaneous velocity field data, in addition to being non-intrusive. PIV measurements can be distinguished based on the measurement domain, the measured velocity components and the timing (temporal resolution). Based on the domain (nD) and measured velocity components (nC) they are distinguished as follows.

- Planar PIV: measures two velocity components (2C) using a single cam-

era which is oriented normal to the laser sheet (2D measurement volume). This is the most straightforward implementation of PIV, a typical setup is illustrated in Figure 3.1.

- Stereoscopic PIV: measures three velocity components (3C) using two or more cameras at different observation angles to the laser sheet (2D measurement volume). The out-of-plane component is calculated through the known viewing angles of the camera. A typical setup is illustrated in Figure 3.2(a).
- Tomographic PIV: proposed by [Elsinga et al. \(2006\)](#) measures the three velocity components (3C) in a three dimensional domain (3D). This technique employs three or more cameras at different observation angles to an illuminated volume. A typical setup is illustrated in Figure 3.2(b).

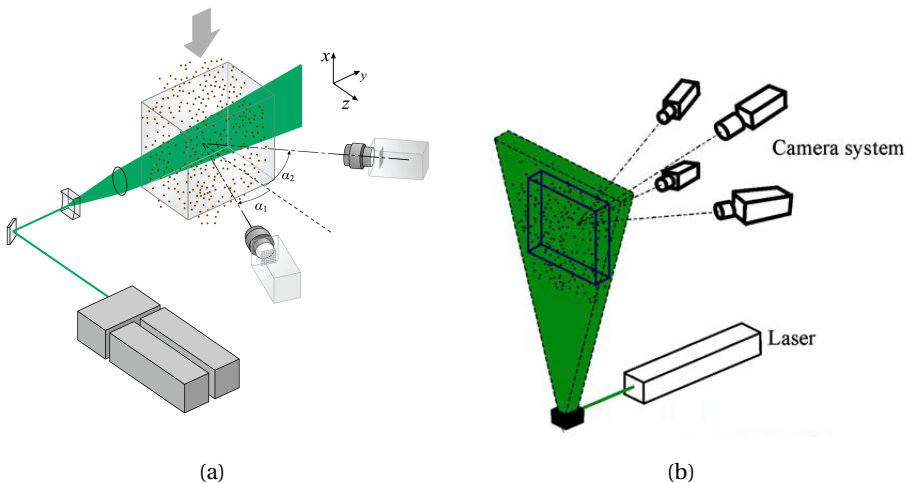


Figure 3.2: Example of camera arrangements from stereoscopic PIV (a) and tomographic PIC (b). Illustrations adapted from [Elsinga et al. \(2006\)](#).

With respect to the timing, two main modes exist i.e. double-frame (single exposure) and multi-frame (single-exposure). In double-frame measurements image pairs are obtained with a small-time separation (Δt), and the time between the image pairs is determined by the recording rate, typically between 10-30 Hz. Whereas in the multi-frame mode (time resolved mode) a continuous series of images are captured, typically at a high frame rate between 1-10 kHz. A schematic of the classification of PIV systems and configurations as proposed in literature is outlined in Figure 3.3.

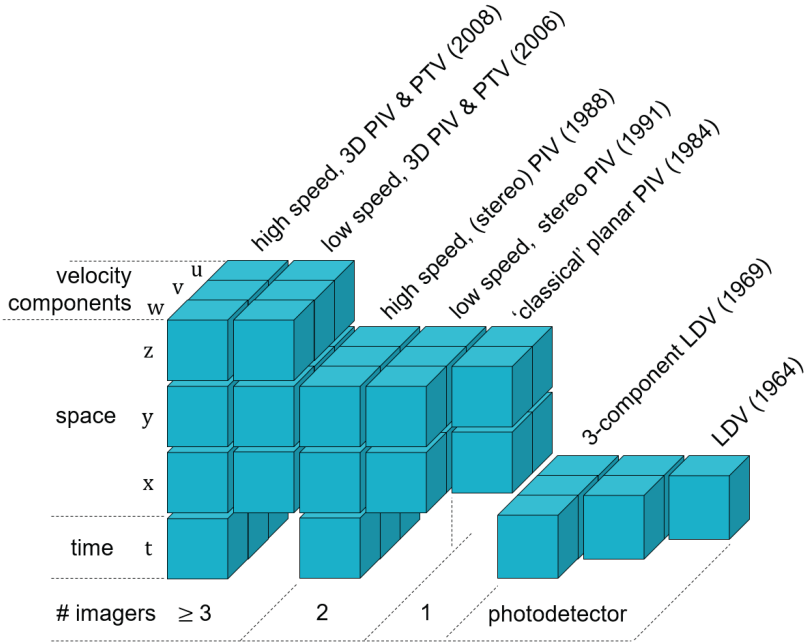


Figure 3.3: Characterisation of PIV and LDV systems by means of measurement dimensionality, resolved velocity components and minimum number of required imagers. Time references in parenthesis indicating first scientific publications of a technique, listed here in order of appearance. Illustration reproduced from [Jux \(2022\)](#).

3.2. TRACER PARTICLES

Measurement of the fluid velocity using PIV would not be possible without suitable tracer particles, whose displacement between two illumination pulses captured on a camera is used to determine the fluid velocity accurately. For a tracer particle to be considered suitable for PIV measurements, the particle is expected to follow the flow faithfully. In an ideal world, the tracer particles would exactly follow the fluid motion while not interacting with each other and not altering the flow or fluid properties. However, the velocity of the tracer particles varies from that of the fluid and is referred to as the slip velocity. The slip velocity leads to a relative motion between the tracer particles and the fluid.

For small particles immersed in a fluid, its motion can be modeled as that of a sphere with a diameter d_p in the Stokes flow regime. The slip velocity (\mathbf{u}_s) can be estimated using the following equation ([Raffel et al., 2018](#)).

$$\mathbf{u}_s = \mathbf{u}_p - \mathbf{u} = d_p^2 \frac{(\rho_p - \rho)}{18\mu} \frac{d\mathbf{u}_p}{dt} \quad (3.1)$$

Where ρ_p is the density of the particle, and ρ and μ are the density and dynamic viscosity of the fluid. From the above equation, zero slip velocity (perfect tracking) can be obtained when.

- $\frac{d\mathbf{u}_p}{dt} = 0$, in a steady and uniform flow.
- $\rho_p - \rho = 0$, for neutrally buoyant particles.

In most cases where PIV is desired, the flow condition does not correspond to a steady uniform flow therefore, the condition of neutrally buoyant needs to be satisfied. For liquid flows, this condition can be easily satisfied ($\rho_p/\rho \sim O(1)$), whereas for gaseous flows, this is not achievable ($\rho_p/\rho \sim O(10^3)$). To overcome this hurdle for gaseous flows, the diameter of the particles is varied to achieve better flow traceability. For this purpose, relaxation time is defined as the response time of the particle to a sudden change in fluid velocity and is represented as

$$\tau_p = d_p^2 \frac{(\rho_p - \rho)}{18\mu} \quad (3.2)$$

For good traceability of the flow, low values of relaxation time are desired, which can be obtained with low particle diameter or with similar densities of that of the particle and the fluid. The fidelity of the tracer particles in turbulent flows is quantified by the particle Stokes number ($S_k = \tau_p/\tau_{flow}$), defines as the ratio between relaxation time and characteristics flow time scale (τ_{flow}). For good tracing capabilities, the particles Stokes number should not exceed 0.1 ([Samimy and Lele, 1991](#)). In the current research, PIV experiments are performed in air, in such conditions the density of the seeding material is often hundreds of times larger than that of the gas ([Melling, 1997](#)). Hence, to achieve good tracing capabilities, small particle diameters of the order of 1 μm are selected. The details of the tracer particles used in the current work are shown in [Table 3.1](#).

Table 3.1: Properties of seeding particles used in the current research.

Material	ρ_p [Kg/m ³]	d_p [μm]	τ_p [μs]	Reference
Fog particles	912	3	22.5	Melling (1997)
Olive oil	970	1	2	Ragni et al. (2011)

In addition to following the flow faithfully the tracer particles are expected to scatter light such that they are captured in the camera. The scattering light intensity is a function of the ratio of the refractive index of the particles to that of the fluid, particles size, shape and orientation and the polarization and observation angles ([Raffel et al., 2018](#)). For spherical particles of diameter d_p larger than

the wavelength of the incident light, Mie's scattering theory applies. Figure 3.4 illustrates the distribution of the scattered light intensity of $1\mu\text{m}$ oil particle in air with wavelength if 532nm .

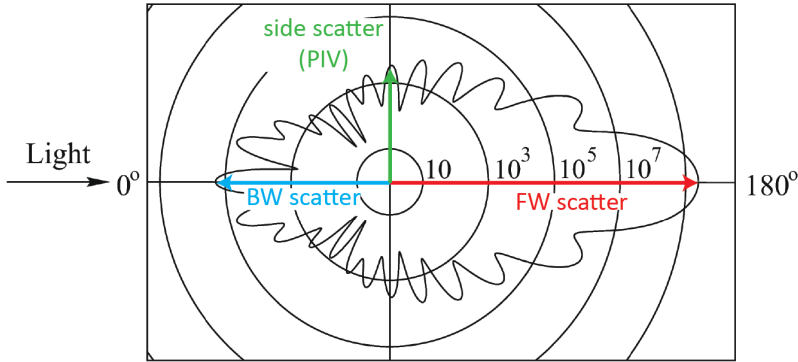


Figure 3.4: Light scattering by a $1\mu\text{m}$ oil particle in air, adapted from Raffel et al. (2018).

From the Figure 3.4 it is clear that light is scattered in all directions, with maximum intensity in the forward direction. However, limitations with respect to the depth of field and optical access necessitate the placement of PIV cameras in side scatter as indicated in Figure 3.4.

3.3. ILLUMINATION OF THE FLOW

The illumination system provides the necessary light that makes the tracer particles visible in the recordings. The shape of the illumination volume can be chosen based on the desired measurement technique (refer to Section 3.1). Lasers are widely used in PIV, due to their ability to emit monochromatic light with high energy density, which can easily be bundled into thin, light sheets/volumes and record the tracer particles without chromatic aberrations. Optics composed of spherical and cylindrical lenses are employed to shape the illumination into sheets with thickness in the 1 to 3mm range, as shown in Figure 3.5.

The most common lasers for PIV measurements are solid-state lasers, such as Nd:YAG and Nd:YLF. Nd:YAG lasers can provide up to 1J of monochromatic light with pulse width below 10ns and repetition rates up to 50 Hz. Nd:YLF lasers, on the other hand, operate in the kilohertz range and are used in high-speed applications. The wavelength of the laser light emitted by Nd:YLF is comparable to Nd:YAG but with lower pulse energy (up to 60mJ at 1kHz and below 10mJ at 10kHz). In addition, some of the temporal parameters that govern the operation of the laser are

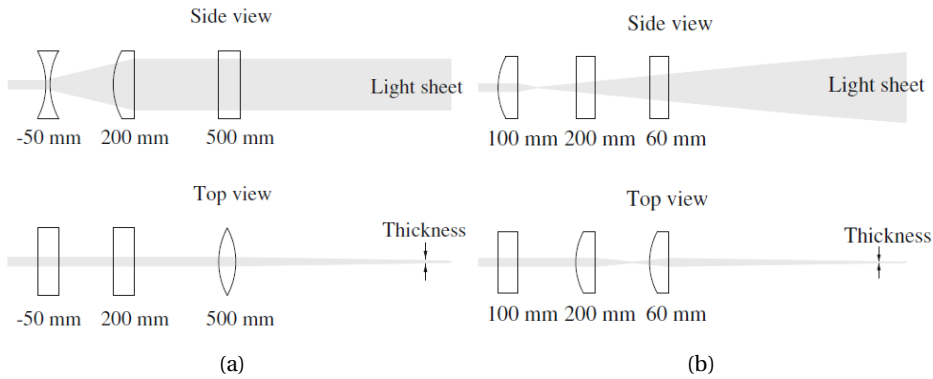


Figure 3.5: Possible configurations of the optics to obtain laser sheet/volumes adapted from Raffel et al. (2018).

- Pulse width (δt): This is the duration for which the light is illuminated. It determines whether the particles are imaged as dots or streaks. Tracer particles in PIV images are imaged as dots, i.e., frozen in time. Therefore, it should not exceed the time the particle takes to move one particle image diameter.
- Pulse separation time (Δt): This is the time between two adjacent light pulses. The value should be determined based on the minimisation of loss-of pairs due to out-of-plane motion (Lin and Perlin), reduction of truncation error based on the assumption of constant velocity between laser pulses and minimisation of relative error on the displacement estimate.
- Acquisition frequency (f_{acq}): It is the rate at which images are acquired. The acquisition frequency determines whether subsequent velocity fields are correlated or uncorrelated in time.

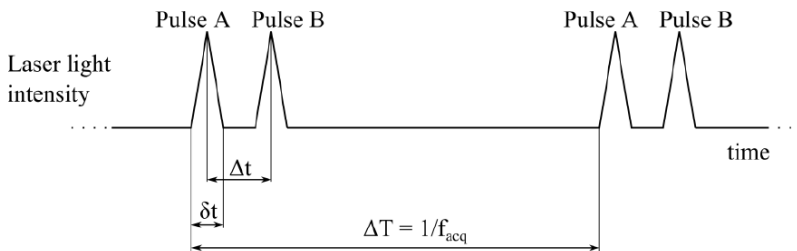


Figure 3.6: Illustration of laser pulse width, pulse separation and acquisition frequency.

3.4. IMAGING OF TRACER PARTICLES

The image of the tracer particles in the light sheet is formed by the lens on the camera sensor. The imaging system is characterised by its focal length (f), f-stop ($f_{\#}$) and image magnification (M). The magnification is defined as the ratio of the image distance and object distance, as described by the thin lens formula:

$$\frac{1}{f} = \frac{1}{d_i} + \frac{1}{d_o} \quad (3.3)$$

$$M = \frac{d_i}{d_o} \quad (3.4)$$

The magnification can also be evaluated as the ratio between the image size (sensor size) and the imaged object size (field of view).

$$M = \frac{\text{sensor size}}{\text{imaged object size}} = \frac{\text{pixel size} \times \text{number of pixels in the sensor}}{\text{field of view}} \quad (3.5)$$

From the diffraction theory, the particle images do not appear as a point but rather form a circular pattern described as an Airy disc (Hecht 2002). A Gaussian function approximates this. Therefore, the diffraction diameter of the particle is given by.

$$d_{diff} = 2.44 f_{\#} (1 + M) \lambda \quad (3.6)$$

The sum of the diffraction and magnification effects gives the resulting particle image diameter.

$$d_{\tau} = \sqrt{(Md_p)^2 + (d_{diff})^2} \quad (3.7)$$

For typical optical parameters in PIV, it is observed that $d_{diff} \gg Md_p$ and therefore $d_{\tau} \approx d_{diff}$. Therefore, the diffraction limit generally dominates the particle image formation, and the particle image diameter is relatively uniform despite variations in d_p . Another point to note is that the light sheet thickness should be smaller than the focal depth of the optical system for the above equation to hold. The focal depth represents the range in which the particles are in focus, i.e. are imaged with sufficient sharpness and is defined as

$$\delta z = 4.88 \lambda f_{\#}^2 \left(\frac{1 + M}{M} \right)^2 \quad (3.8)$$

The seeding density in a PIV image is expressed as the number of particles per unit pixel area (ppp). Typical values of the seeding density range between 0.02 and 0.2 ppp [Scarano and Poelma \(2009\)](#).

The most common sensors used for PIV image acquisition are CCD (charge couple device) and CMOS (Complementary Metal Oxide Semiconductor) devices. These sensors convert the light into electric charge, which is further converted into voltage and the stored digital signal.

3.5. IMAGE INTERROGATION

After the images have been recorded, the fluid motion is evaluated by tracking the displacement of the tracer particles. PIV computes the fluid velocity by tracking the movement of particle image ensembles within regularly spaced interrogation windows. In each interrogation window, the mean particle displacement is evaluated as the shift that maximises the matching between the images at two-time instances t and $t + \Delta t$. The degree of matching is computed mathematically by employing the statistical cross-correlation operator. In digital recordings, the two images I_a and I_b are spatially discretised at integer pixel locations (i, j) . The intensity of each pixel corresponds to the amount of light gathered by the pixel. In such conditions to overcome the sensitivity to the changes in the intensity of the two frames, the normalised cross-correlation function is defined as

$$C(m, n) = \frac{\sum_{i=1}^{W_s} \sum_{j=1}^{W_s} [I_a(i, j) - \bar{I}_a] \cdot [I_b(i + m, j + n) - \bar{I}_b]}{\sqrt{\sum_{i=1}^{W_s} \sum_{j=1}^{W_s} [I_a(i, j) - \bar{I}_a]^2 \cdot \sum_{i=1}^{W_s} \sum_{j=1}^{W_s} [I_b(i, j) - \bar{I}_b]^2}} \quad (3.9)$$

Wherein W_s is the linear size of the interrogation window (assumed to be squared). An optimisation process is conducted to determine the displacement that maximises C . With \bar{I}_a and \bar{I}_b being the spatial average of I_a and I_b respectively, within the interrogation window. One drawback of the abovementioned equation is that it is a discrete function. Therefore, only integer-valued particle displacements would be estimated. As a result, the displacement resolution would be half a pixel, as the cross-correlation peak cannot be identified. This means that, for a displacement of 10 pixels, the relative uncertainty would be 5%.

To overcome this, the peak displacement can be determined with sub-pixel accuracy by interpolating the output of the cross-correlation function. Several peak fitting algorithms have been proposed in the literature, like the centre of mass method, parabolic fit and the Gaussian fit (R). The Gaussian fit algorithm is commonly implemented for its accuracy in estimating the peak shape. The particle images are also described by an Airy function, which a Gaussian function can accurately approximate.

3.6. PIV DYNAMIC RANGES, ERRORS AND UNCERTAINTIES

Dynamic spatial and velocity ranges (DSR, DVR) are two parameters that represent the performance of the PIV measurement. These parameters are related to the spatial and velocity resolution and accuracy. The dynamic spatial range is the ratio of the largest to the smallest resolvable spatial variation in the measurement domain. The largest measurable scale is the size of the field of view in the object space, and the smallest corresponds to the interrogation window size. DSR is represented as.

$$DSR = \frac{ML_x}{W_s} = \frac{l_x}{W_s} \quad (3.10)$$

Where L_x and l_x are the linear field of view in object and image space, respectively. The dynamic velocity range is defined as the ratio between the largest measurable displacement (Δx_{max}) and the smallest resolvable displacement fluctuation ($\sigma_{\Delta x}$).

$$DVR = \frac{\Delta x_{max}}{\sigma_{\Delta x}} \quad (3.11)$$

Errors are defined as the difference between the measured velocity and the true value. For velocity measurements in PIV, the equation for measurement error in the velocity (which is determined by the particle displacement during the pulse separation time Δt) is defined as.

$$\varepsilon_u = u_{meas} - u = u_{meas} \cdot \sqrt{\left(\frac{\varepsilon_{\Delta x}}{\Delta x}\right)^2 + \left(\frac{\varepsilon_{\Delta t}}{\Delta t}\right)^2} \quad (3.12)$$

Where u and u_{meas} are the true and measured velocities. $\varepsilon_{\Delta x}$ and $\varepsilon_{\Delta t}$ are the errors on the measured displacement and pulse separation. The error on the pulse separation time is in the order of one nano second, whereas the separation time is greater the one microsecond which implies that error in time separation is below 0.1%. Therefore, the primary error in the velocity arises from the error in the displacement. The typical displacement of particles in PIV measurements is around 10 pixels, while the uncertainty on the displacement is of the order of 0.1 pixel. Therefore the relative error is about 1% (Raffel et al., 2018). This displacement error propagates into the derived quantities like Reynolds stress, vorticity and others. For a more indepth literature review on errors, the readers can refer to Raffel et al. (2018); Westerweel (1997).

The uncertainty U is an estimate of the interval likely to contain the magnitude of the error affecting the measurement. Coleman and Steele Jr (2009) defined standard uncertainty as an estimate of the standard deviation of the actual error distribution.

The expanded uncertainty U represents the error magnitude that falls within the interval $\pm U$ with probability P , referred to as the confidence level. The expanded uncertainty is calculated from the standard uncertainty as :

$$U = k U_s \quad (3.13)$$

The coverage factor k depends upon the error distribution and the confidence level. Assuming that the error has a Gaussian distribution, $k = 1$ and $k = 1.96$ yield a confidence level of 68.3% and 95%, respectively.

4

SKIN-FRICTION CONTROL BY SPANWISE WALL OSCILLATIONS

*A journey of a thousand miles
begins with one step.*

Lao Tzu

The current chapter investigates the active skin-friction control technique of spanwise wall oscillations. Planar and Tomographic PIV has been employed to quantify the skin-friction reduction and observe the effect of the wall oscillations on the 3-dimensional structures in the TBL. The high-resolution planar-PIV data enables the direct determination of the drag reduction from wall shear measurements. Maximum reductions of 15% are quantified, and the obtained trends of drag reduction agree well with the numerical studies reported in the literature. A hypothesis is introduced based on qualitative observations of the 3-dimensional velocity fields to explain the underlying mechanism for the skin-friction reductions obtained.

Parts of this chapter have been published in [Kempaiah et al. \(2020\)](#)

4.1. INTRODUCTION

Turbulent skin-friction drag is relevant to many natural processes and engineering applications. Several attempts to control turbulent drag have been reported using passive and active techniques (Gad-el Hak, 1996). Early studies of turbulent boundary layers (Driver and Hebbbar, 1987) showed that a fully-developed turbulent boundary layer, when subjected to a sudden spanwise pressure gradient, reduced turbulence production and Reynolds stresses. The Direct Numerical Simulation (DNS) study of Sendstad (1992) showed that skewing motion is necessary to weaken the quasi-streamwise vortices. Following this, spanwise wall oscillations received much attention, and the relevant literature has been discussed in Section 2.2.1.

Current literature states that the oscillations corresponding to $T_{osc}^+ \approx 100$ lead to maximum skin-friction drag reduction when A_{osc}^+ exceeds 100, which corresponds to the mean streak spacing (Kline et al., 1967). Further increasing the amplitude produces even higher drag reduction. Literature provides many possible explanations concerning the physical mechanisms of drag reduction (Section 2.2.1). One of the likely hypotheses is that the imposed spanwise wall motion affects the orientation of the streamwise vortices, in turn, disrupting the lift-up mechanism and thereby the production of turbulence (Di Cicca et al. (2002), Toubert and Leschziner (2012)). This disruption directly corresponds to reduced ejection and sweep events, which drive wall-normal momentum transport. These ejections are associated with the formation of hairpin or horseshoe vortices (Zhou et al., 1999), known to occur in packets and travel with similar velocities (Adrian et al., 2000). Therefore, it is interesting to understand and quantify the effect of spanwise wall oscillations on these coherent structures and the hairpin packets.

Though both DNS and experiments have provided evidence that spanwise oscillations can reduce skin-friction drag, there are many quantitative discrepancies when comparing the maximum drag reduction observed, as noted by Quadrio and Ricco (2004). Experiments on drag reduction by spanwise wall oscillations reported in the literature have widely employed hot wire anemometry (HWA), given the high accuracy, small probe size and high temporal resolution. Although it is beneficial for extracting spectral information, single-probe HWA measurements do not provide complete information on the behaviour of the different components of the Reynolds stresses. Quantifying the change in velocity fluctuations in streamwise and wall-normal directions within the boundary layer is essential, as they are connected to the turbulent shear stress and wall-normal momentum transport. In addition, turbulent kinetic energy (TKE) production, which is related to shear stress, can also explain the effects of wall oscillation. Knowledge of the Reynolds stresses would require multi-wire probes, and the study of the velocity gradient components (e.g. vorticity) would need multi-wire

arrays (Vukoslavčević et al., 1991), which adds complexity to the measurement system.

Planar particle image velocimetry (PIV) measurements provide quantitative information on the in-plane components of the Reynolds stress tensor and the spanwise component of the vorticity vector (Adrian et al., 2000) at a high resolution. The high-resolution data allows the measurement of the local shear at the wall directly, provided that the spatial resolution matches the scale of the viscous layer (Kähler et al., 2006). It can also be used to describe relevant properties in the boundary layer, such as the turbulent kinetic energy production and Reynolds shear stress (Kline et al., 1967). Direct measurement of wall shear by PIV has not yet been attempted over the spanwise oscillating wall because of the spatial resolution limits encountered in past experiments (Di Cicca et al., 2002). The lack of data in three dimensions (3D) experimental data over the oscillating wall can be overcome by employing tomographic PIV (Elsinga et al., 2006), which provides information on the instantaneous 3D organisation of the coherent structures in the turbulent boundary layer.

The present study describes the application of planar and tomographic PIV to study skin-friction drag reduction over a spanwise oscillating wall. The drag estimates are obtained employing high-resolution planar PIV to measure the near-wall velocity gradient, yielding an estimate of the wall shear. The method and its inherent uncertainties are discussed, and the findings are compared with existing data. The vortex dynamics in the boundary layer are investigated through vorticity analysis and by observing the instantaneous planar and 3D vorticity fields, which are used to infer the organisation of the turbulent structures, with a focus on hairpin packets.

4.2. EXPERIMENTAL SETUP AND PROCEDURE

4.2.1. WIND TUNNEL AND OSCILLATING WALL

The experiments were conducted in an open-return low-speed wind tunnel at the Aerospace Engineering laboratories of the Delft University of Technology. The tunnel features a contraction ratio of 9:1 with an exit cross-section of $40 \times 40 \text{ cm}^2$. The flow at the exit was confined within a 1.6 m long rectangular channel and a flat plate is installed 0.1 m above the channel floor. For the current experimental conditions, the turbulence intensity at the edge of the boundary layer was measured to be below 1.4%.

Table 4.1: Turbulent boundary layer properties.

Re_θ	Re_τ	U [m/s]	δ_{99} [mm]	δ^* [mm]	θ [mm]	u_τ [m/s]	l^+ [mm]	H
980	570	3.0	59	6.7	4.9	0.145	0.10	1.36

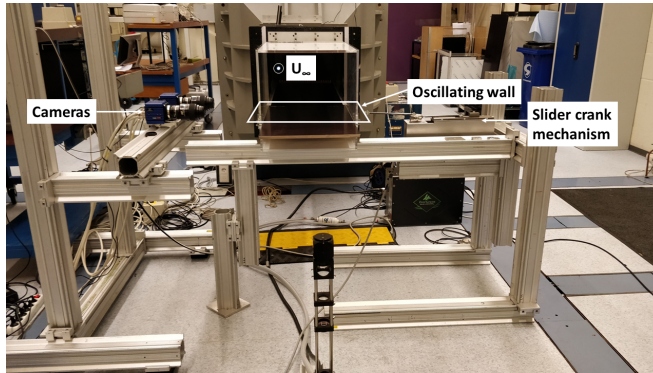
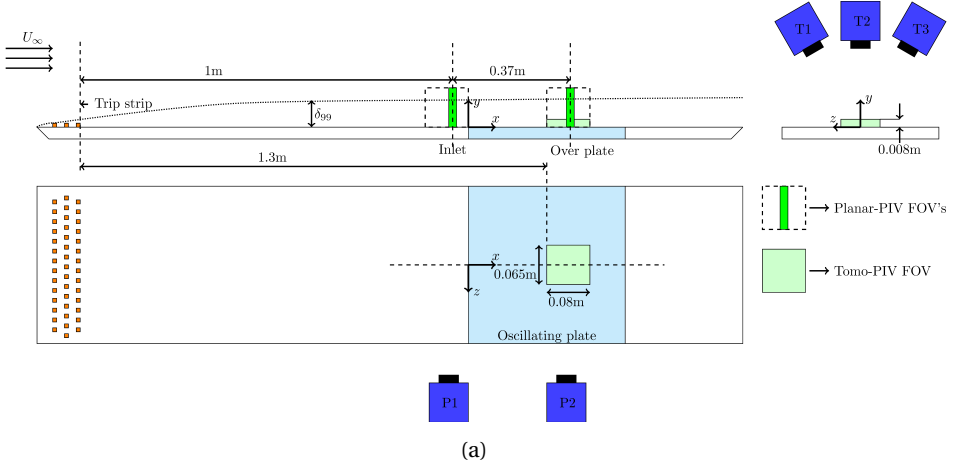


Figure 4.1: Schematic of the oscillating plate setup with acquisition locations for both planar and tomographic measurements shown (a, not to scale); Photo from the wind tunnel with the experimental setup (b).

The boundary layer was tripped at a distance of 5 cm after the leading edge of the plate using distributed roughness elements of 1.0 cm height (Lima Pereira et al., 2020). The schematic layout of the experiment is illustrated in Figure 4.1. The oscillating plate has a streamwise length of $L=0.4$ m and is installed 1.0 m downstream of the location where the boundary layer transition is forced. The

oscillations were obtained using a slider-crank mechanism capable of reaching up to 15 Hz oscillation frequency and with a peak-to-peak amplitude of 2 cm. A counterweight was introduced in the oscillation mechanism to minimise vibrations. The test section was realised in Plexiglas to provide optical access for PIV illumination and imaging. The measurements were performed at a free stream velocity of 3.0 m/s, corresponding to a momentum-thickness-based Reynolds number $Re_\theta \approx 10^3$. The properties of the undisturbed incoming boundary layer, immediately upstream of the oscillating plate, are described in Table 4.1, where Re_τ is the Reynolds number based on the friction velocity, U_∞ the free stream velocity, δ_{99} the boundary layer thickness, δ^* the displacement thickness, θ the momentum thickness, l^+ the length of one wall unit and H the shape factor.

4.2.2. PIV SETUP

The planar-PIV measurements were obtained using two LaVision Imager sCMOS cameras (2560×2160 pixels, 16 bits, 6.5 μ m pixel size) equipped with Nikon objectives of 105 mm focal length (P1 and P2, Figure 4.1(a)). The measurements were performed at two streamwise locations: ahead ($x/L=-0.075$) and over ($x/L=0.85$) the oscillating plate, at the wall-normal (xy) positions indicated in (Figure 4.1(a)). The non-dimensionalization of the streamwise location is done with the length of the oscillating plate with its leading-edge as reference. The flow was seeded with fog droplets of 1 μ m diameter produced with a SAFEX smoke generator. Illumination was provided by a Quantel Evergreen 200 laser (Nd:YAG, 2×200 mJ, 15 Hz). The digital synchronisation between laser, cameras and the image acquisition system was provided by a LaVision programmable timing unit controlled through DaVis 8.4. The light sheet was 2 mm thick, oriented parallel to the flow, aligned at the mid-plane through the reference axis providing measurements in the streamwise-wall normal plane. Hardware details and settings are listed in Table 4.2.

The tomographic measurements were performed at a streamwise distance of $x/L = 0.75$ downstream from the leading edge of the oscillating plate. The measurement volume encompassed a region of 80(x) × 65(z) × 8(y) mm³ which corresponds to 800 × 650 × 80 wall units over the surface of the oscillating wall, with the smallest dimension normal to the wall (Figure 4.1). The fog particles were used to obtain a particle image density of approximately 0.015 particles per pixel (ppp). The same illumination source was employed as for the planar experiment. A knife-edge slit was added to the path of the laser light sheet to obtain uniform light intensity over the measurement volume of 8 mm thickness above the wall. A dual-pass illumination (Ghaemi and Scarano, 2010) was obtained with a planar mirror placed at the opposite side of the light entrance, which intensified laser illumination and homogenized the light received by the cameras partly in

Table 4.2: Description of parameters for the PIV measurements.

	Planar-PIV	Tomographic-PIV
Seeding particles	Fog droplets ($d_p = 1\mu\text{m}$)	
Illumination	Nd:YAG, 2×200 mJ, 15Hz	
Recording device	sCMOS 2560 \times 2160 pixels, 16 bits 6.5 μm pixel pitch	
Recording method	Double frame/Single exposure	
Number of cameras	2 (P1, P2)	3 (T1, T2, T3)
Field of view	7.4 \times 6.2 cm^2	8.0 \times 6.5 \times 0.8 cm^3
Recording lens and aperture	105 mm, $f_{\#}=8.0$	105 mm, $f_{\#}=8.0$
Imaging resolution	30 pixels/mm	32 pixels/mm
Observation distance	0.4 m	0.4 m
Optical magnification	0.22	0.2
Image seeding density	0.03ppp	0.015 ppp
Recording frequency	15 Hz	13.5 Hz
Pulse delay	150 μs	150 μs
Number of recordings	2000	100 (at each phase)
Interrogation window and vector pitch (Wall shear meas.)	1.4 \times 0.35 mm^2 (48 \times 12 px) (75% overlap along y) 0.081 mm	48 \times 48 \times 48 voxels (75% overlap) 0.38mm
Interrogation window and vector pitch (Vorticity meas.)	0.94 \times 0.94 mm^2 (32 \times 32 px) (75% overlap) 0.23 mm	
Dynamic spatial range	180 (Wall normal direction)	50
Dynamic velocity range	200	200

back- and forward-scattering mode. The tomographic imaging system featured four LaVision imager sCMOS cameras (T1, T2 and T3, Figure 4.1). Three cameras subtended an arc with a total angle of 50° . The fourth camera monitored the position of the oscillating wall. The focal plane of each imaging unit was aligned with the median plane of the laser sheet by means of Scheimpflug adapters able to tilt the objectives relative to the image plane along oblique axes. The average imaging magnification was $M = 0.2$ with a digital resolution of 32 pixels/mm.

The recording rate was 13.5 Hz and the time separation between subsequent exposures was set at $150\mu\text{s}$.

4.2.3. DATA REDUCTION AND UNCERTAINTY ANALYSIS

For the planar-PIV measurements, the recorded sequences comprised 2000 double-frame images, with details given in Table 2. The image interrogation was performed using multi-pass cross-correlation with window refinement and deformation (Scarano and Riethmuller, 2000). Non-isotropic windows were used to increase the wall-normal resolution (Scarano, 2003). In the final iterations, windows of 48×12 pixels ($1.41 \times 0.35\text{mm}^2$) were used with an overlap factor of 75% (3:4) along the vertical direction. The resulting vector spacing was 0.081 mm (11.5 vec/mm) along the wall-normal direction, corresponding to approximately one wall unit (see Table 4.1). The size of the correlation window for the visualisation of velocity and vorticity was 32×32 pixels ($0.94 \times 0.94\text{mm}^2$), with a vector pitch of 0.23 mm. The dynamic spatial range, given as the ratio between the length of the measurement domain and the interrogation window (Adrian, 1997) was 180, considering the wall-normal direction. The dynamic velocity range given as the ratio of maximum velocity to the minimum resolvable velocity was 60, based on the diffraction limit criterion and the maximum particle displacement in the measurement domain (Adrian and Westerweel, 2011).

For the near-wall measurements, attention was posed first to accurately determine the position of the wall (Section II.0). Secondly, measurements within the viscous sub-layer ($y^+ < 5$) were obtained with 5 vectors in the first 0.5 mm, where the velocity was observed to follow a linear trend.

The measurement uncertainty of the velocity statistics was based on the convergence of the Gaussian dispersion based on 2,000 uncorrelated samples. A 95% confidence interval was considered, according to Equation 4.1 and 4.2. The data is presented in Table 4.2.

$$\epsilon_{\bar{u}} = \frac{1.96}{\bar{u}} \frac{\sigma_{\bar{u}}}{\sqrt{N-1}} \quad (4.1)$$

$$\epsilon_{u'} = \frac{1.96}{\sqrt{N-1}} \quad (4.2)$$

Table 4.3: Statistical uncertainty of mean velocity and turbulent fluctuations at $y^+ = 10$, (% with respect to mean free-stream velocity (\bar{u})).

Re_θ	Number of Samples	Uncertainty Mean $\epsilon_{\bar{u}}$ (%)	Uncertainty variance $\epsilon_{u'}$ (%)
980	2000	1.25	3.4

For the tomographic measurements, the object-to-image calibration was performed with a plate (LaVision Type 10) with 16×14 markings, imaged at three positions along the volume depth. After 3D self-calibration (Wieneke, 2008), the calibration disparity was reduced to approximately 0.02 pixels. The intensity distribution was reconstructed in a $80 \times 65 \times 8 \text{ mm}^3$ volume which corresponds to $800 \times 650 \times 80$ in wall units discretized with $2580 \times 2096 \times 258$ voxels using the CSMART reconstruction algorithm (Gan et al., 2012) with five iterations. Image pre-processing was performed to remove background intensity by subtracting the minimum value of intensity at each pixel. The cross-correlation analysis returned $215 \times 91 \times 11$ velocity vectors using an interrogation volume size of $48 \times 48 \times 48$ voxels (1.5 mm linear size), yielding a vector spacing of 0.375 mm with 75 % overlap (Table 4.3). For the case with the oscillating wall, specific values of the phase ϕ were examined, namely that of maximum transverse wall velocity ($\phi = 0, \pi$) and that of maximum transverse displacement, when the motion is inverted (zero velocity, $\phi = \pi/2, 3\pi/2$, Section III.d).

Table 4.4: Tomographic reconstruction processing parameters.

Image pre-processing	Subtract time averaged pixel intensity
3D calibration	3^{rd} order polynomial at 3 planes
Calibration correction	Volume self-calibration
Volume discretization	$2580 \times 2096 \times 258$ voxels
Reconstruction technique	CSMART (5 iterations)

When comparing the mean velocity profile from the tomo-PIV measurements to the high-resolution 2C-PIV and DNS data (Section III.a), agreeing values in the range $20 < y^+ < 80$ were obtained. Closer to the wall, laser light reflections hampered the measurements. Also, above 80 wall units from the wall, the illumination laser light intensity decays and particles were not detectable. The data from tomographic PIV was employed primarily for vorticity analysis. The accuracy of the velocity gradient was estimated from the analysis of the measured velocity divergence (Scarano and Poelma, 2009). The conservation of mass necessitates that the divergence of the velocity field to be zero in the domain. The distribution of the divergence exhibits a normal distribution around 0, with a standard deviation corresponding to 40 s^{-1} . Considering that instantaneous vorticity fluctuations are measured that attain a typical value of 200 s^{-1} (see for instance, Section III.e), the estimated relative uncertainty amounts to 20%. The errors are mostly ascribed to the truncation effects arising from the limited spatial resolution of the measurement, following Scarano and Poelma (2009).

4.2.4. DRAG REDUCTION EVALUATION

The time-averaged velocity profile measured by planar PIV features a symmetric shape with respect to the wall: the data points “inside the wall” being the result of the reflections of particle tracers. The symmetry axis can, therefore, be used to indicate with good accuracy the position of the mirroring wall. Figure 4.2 illustrates the velocity profile in proximity of the wall. The vertical axis, in this case, represents the wall-normal coordinate, with an arbitrary point of origin. From the symmetry of the profile, the wall position was inferred to be at $y = 2.47\text{ mm}$, with an uncertainty of 0.01 mm estimated from the discrepancy between the two linear fit from above the wall and the reflected image respectively.

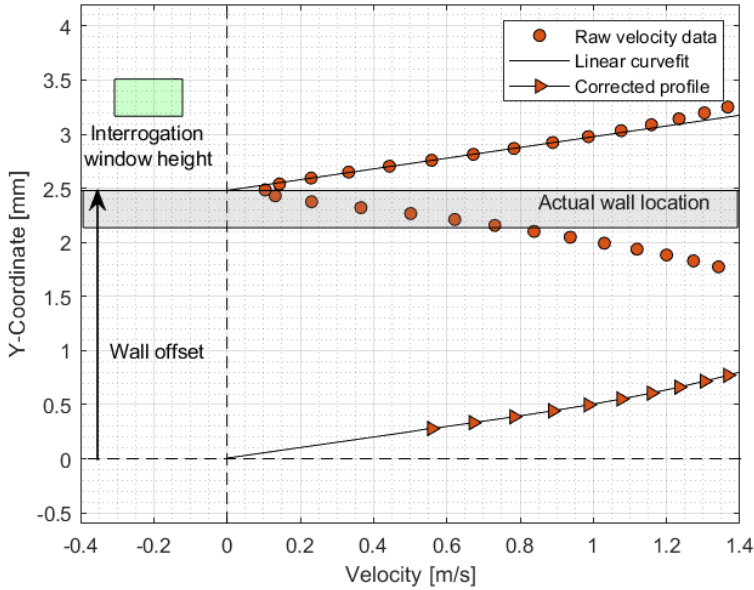


Figure 4.2: Wall position determination at $x=1.37\text{ m}$ from leading edge (over plate, Figure 4.1).

The slope $\left(\frac{\partial u}{\partial y}\right)_{y=0}$ at the wall is estimated from a linear fit in the data interval from 0.15 to 0.4 mm ($y^+ = 1.5 - 4$), where the velocity exhibits a linear behaviour within a correlation of 95%. The above provides a quantitative description of the shear stress τ_w , which is determined with an uncertainty of 1.5%. Accordingly, the friction velocity and skin-friction coefficient (C_f) are calculated as

$$u_\tau = \sqrt{\nu \left(\frac{\partial u}{\partial y}\right)} \quad (4.3)$$

$$C_f = 2 \left(\frac{u_\tau}{u_\infty} \right)^2 \quad (4.4)$$

Following [Quadrio and Ricco \(2004\)](#) the drag reduction is defined as:

$$\text{Drag reduction (DR) (\%)} = \frac{C_f^0 - C_f}{C_f^0} \times 100 \quad (4.5)$$

Where C_f^0 and C_f are the skin friction coefficients of the steady and the oscillating wall, respectively.

4.3. RESULTS AND DISCUSSION

4.3.1. TURBULENT BOUNDARY LAYER CHARACTERISTICS

The mean boundary layer velocity profile and the kinematic Reynolds stresses at the inlet plane just upstream of the oscillation plate (see [Figure 4.1](#)) were obtained by ensemble averaging of the PIV velocity data, and represented in wall-unit scaling. The velocity profile is compared with DNS data computed at $Re_\theta = 1,000$ and $Re_\tau = 360$ ([Schlatter and orlu, 2010](#)). The planar PIV data exhibit a good agreement in the inner region with a resolved viscous sublayer (Section II-c) as shown in the near-wall profile (inset [Figure 4.3](#)). The spatial range of the tomographic measurements was fairly limited in the wall normal direction $y^+ = [20 - 80]$, given that the tomographic data is intended to visualise the velocity and vorticity structures along the spanwise and streamwise directions. The reduced wake region is attributed to the influence of the strong tripping that is employed ([Vila et al., 2017](#)).

The Reynolds stresses obtained from 2C-PIV are in good agreement with the DNS data ([Figure 4.4](#)) with peak streamwise fluctuations $\langle u'u' \rangle^+$ slightly higher than DNS by 2%. A small shift of the data towards higher y^+ is suggested, however in the order of $1y^+$, which corresponds to the uncertainty in the location of the wall. The deviations observed in the outer regions of the boundary layer, where the intensity of the measured fluctuations persists at $y^+ \sim 500$, whereas the DNS results collapse to zero already at $y^+ \sim 400$ due to the difference in Re_τ of the data.

4.3.2. TURBULENT SKIN-FRICTION ANALYSIS

The experiments were conducted for different values of the oscillation frequency and with a constant amplitude, following [Table 5](#). The range of imparted oscillatory motions covers both favourable and unfavourable conditions and the trends are depicted in [Figure 5](#). A peak reduction of 15% is obtained at $T_{osc}^+ = 94$

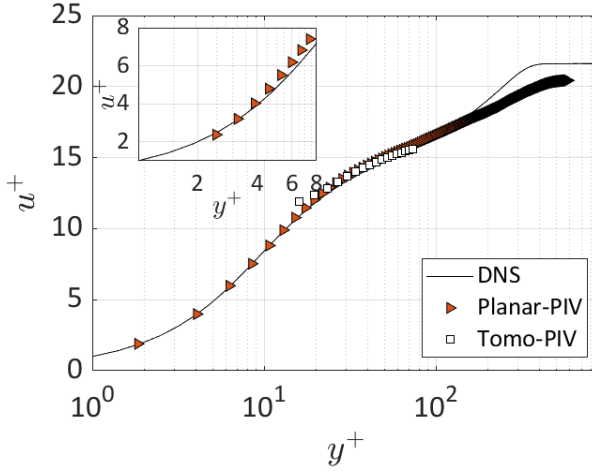


Figure 4.3: Measured mean streamwise velocity profile for the stationary wall with inner-layer scaling and comparison to DNS data from literature ($Re_\theta = 1,000$).

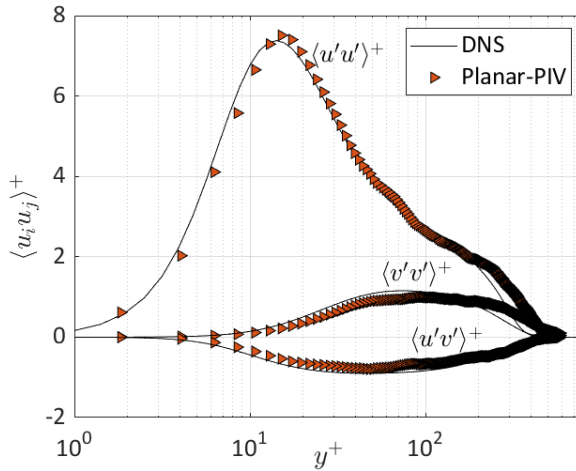


Figure 4.4: Measured wall-normal profiles of Reynolds stresses for the stationary wall and comparison to DNS data from literature ($Re_\theta = 1,000$).

and $A_{osc}^+ = 100$. The non-dimensional wall velocity ($W_m^+ = \pi A_{osc}^+ / T_{osc}^+$) corresponding to the above case is $W_m^+ = 3.34$ and the reported reduction from literature for a similar condition ($T_{osc}^+ = 100$ and $W_m^+ = 4.5$) is 17%, according to [Quadrio and Ricco \(2004\)](#). From [Table 4.4](#) it can be observed that the oscillations lead to significant drag reduction in the range of $T_{osc}^+ = [94 - 175]$. The effects of

the oscillating wall penetrate through the boundary layer up to a thickness estimated by $\delta_{st} = \sqrt{\frac{\nu T_{osc}}{\pi}}$, this region is denoted as the Stokes layer, in reference to the Stokes second problem (Schlichting and Kestin, 1961). Table 4.5 contains the inner-scaled Stokes layer thickness for the investigated range of T_{osc}^+ . Baron and Quadrio (1995) state that a Stokes layer of thickness less than $10l^+$, associated with the region where streaks are more prevalent, results in drag reduction as long as the A_{osc}^+ is greater than 100, corresponding to the mean streak spacing. The motion in the Stokes layer creates a relative displacement between the streaks and the streamwise vortices, which lie between $10 < y^+ < 50$. The results obtained here return drag reduction as long as $\delta_{st}^+ < 8$, while an increase in drag is observed for values of δ_{st}^+ above 11, which agrees with the observations from Baron and Quadrio (1995).

Table 4.5: Drag reduction inferred from wall shear measurements for $Re_\theta = 1000$.

T_{osc}^+	A_{osc}^+	W_m^+	Stokes layer δ_{st}^+	% DR (\small{'+ indicates reduction})
94 (15Hz)	100 (10 mm)	3.34	5.5	+14.6
107 (13Hz)		2.93	5.9	+9.9
140 (10Hz)		2.24	6.7	+8.7
175 (8Hz)		1.79	7.5	+4.6
350 (4Hz)		0.89	11	-1.2
700 (2Hz)		0.45	15	-4.1

4.3.3. REYNOLDS STRESS AND TURBULENCE PRODUCTION

The behaviour of the Reynolds stresses $\langle u_i' u_j' \rangle^+$ for the two cases representing highest drag reduction ($T_{osc}^+ = 94$) and drag increase ($T_{osc}^+ = 700$) are compared with the conditions encountered for the stationary wall, where normalization is performed with u_τ of the stationary wall. For the oscillations at $T_{osc}^+ = 94$ the normal stress in the streamwise direction $\langle u' u' \rangle^+$ is lowered, with a peak reduction of 23%. A large relative reduction is also observed in the normal stress along the wall-normal direction $\langle v' v' \rangle^+$ by 14% and the shear stress $\langle u' v' \rangle^+$ by 18% (Figure 4.6). Aside from the peak reduction, the streamwise fluctuations are reduced throughout the turbulent boundary layer, indicating that the effect of the oscillating wall is felt away from the wall up to approximately $y^+ \simeq 200$. The reduction of streamwise fluctuations is a consequence of the decreased wall-normal motions, dominated by ejections and sweeps. The spanwise displacement between the streaks and the streamwise vortices produced by the Stokes layer inhibits the lift-up mechanism, essential for maintaining turbulent energy production.

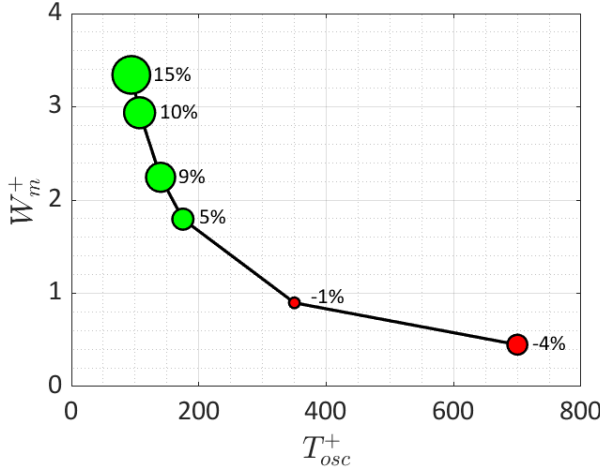


Figure 4.5: Drag reduction as a function of oscillation frequency and wall velocity (experimental data obtained at $A_{osc}^+ = 100$). Green for reduction and red for increase.

Apart from the reduction in the peak of the streamwise stress, the position of the peak is shifted towards larger wall-normal distance, where the shift is $4l^+$ for $\langle u'u' \rangle^+$, $23y^+$ for $\langle u'v' \rangle^+$, and $36l^+$ for $\langle v'v' \rangle^+$. For the oscillations at $T_{osc}^+ = 700$, a slight increase in all the components of Reynolds stress for the region corresponding to y^+ of 7 to 50 is observed (Figure 4.6). The results of Choi et al. (1998), also report large reductions (30%) in the streamwise velocity fluctuations in the near-wall region for the oscillated wall, while the outer region remains unaltered by the presence of the oscillations, in agreement to that reported in Choi et al. (1998).

The dominant term of the turbulent kinetic energy production is evaluated from the measured data. The pre-multiplied normalized production ($P^+ y^+ = -\frac{\nu}{u_t^4} \overline{u'v' \frac{\partial u}{\partial y}} y^+$) is shown for oscillations at $T_{osc}^+ = 94$ and 700 in comparison with that of the stationary wall. For $T_{osc}^+ = 94$, a significant reduction in peak pre-multiplied production of 20% is observed at a wall-normal distance of $10 - 25y^+$, close to the peak reduction in the streamwise Reynolds normal stress (Figure 4.6). A clear reduction is also observed upto $y^+ = 100$, corresponding to the region where hairpin vortices exist. For $T_{osc}^+ = 700$, a mild decrease in pre-multiplied production occurs for y^+ up to 25 (Figure 4.7), beyond which an increase is quantified. The oscillations at $T_{osc}^+ = 700$, are not sufficient to provide the required displacements of the streaks that leads to a reduction of the ejection and sweep events. Due to the lower time scale of these oscillations additional disturbances are imparted in the flow field which manifests as an increase in drag. Because of

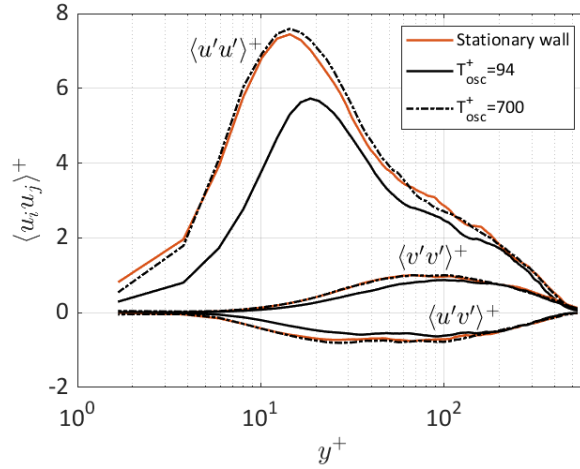


Figure 4.6: Comparison of the Reynolds stress distribution.

the small variation in the Reynolds stresses and TKE production (less than 2.5% in peak increase), the instantaneous flow organization is only analysed considering the stationary wall and oscillations at $T_{osc}^+ = 94$, which resulted in the most reduction in drag.

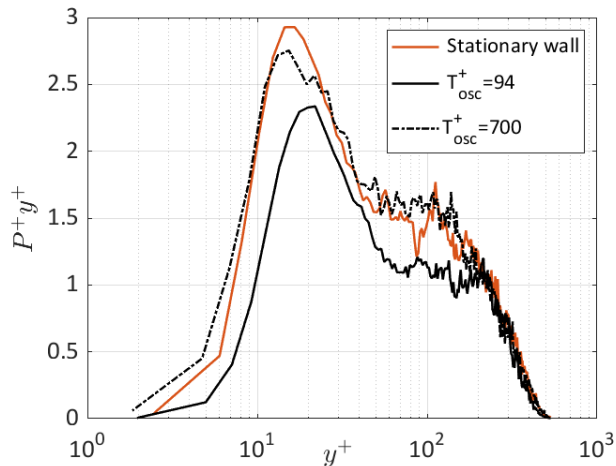


Figure 4.7: Comparison of pre-multiplied turbulence production distribution.

4.3.4. INSTANTANEOUS FLOW ORGANIZATION

The observation of coherent motions in the boundary layer is performed here taking into account the topology of vorticity fluctuations ($\omega_z^+ = \frac{\omega_z V}{u_\tau^2}$ from planar PIV) and the combination of velocity fluctuations with vortex detection (L2-criterion from the tomographic PIV data). Attention is put on the role of groups of hairpins (hairpin packets, Adrian et al. (2000)), which contribute significantly to the wall-normal momentum transport by focussed ejections and sweep motions. For the initial observation of the presence and behaviour of these structures, vorticity contours derived from the planar PIV data are used. The instantaneous structure of the vorticity field is scrutinised to determine the changes in the large-scale flow structures produced by wall oscillations (at $T_{osc}^+ = 94$ and $Z_{osc}^+ = 100$) with respect to those of the stationary wall.

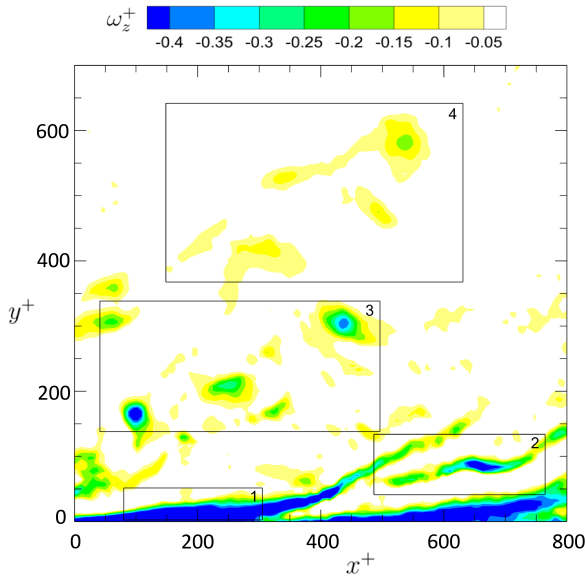


Figure 4.8: A sample of the instantaneous vorticity field obtained with stationary wall.

The inspection of a series of instantaneous vorticity fields allows the identification of several recurrent flow events, for the case of a stationary and oscillating wall. Figure 4.8 depicts as an example the vorticity contours of instantaneous structures typically observed. A series of visualisations is annexed in Figure 4.8. For the discussion boxed areas outline different flow features, numbered from 1 to 4 containing respectively: 1) regions of high shear close to the wall due to the no-slip condition; 2) inclined vorticity sheet structures, lifted-up from the wall region; 3) hairpin heads featuring a localized peak of vorticity – the structure of

a packet may be inferred too, with inclination to the wall between 25-45° (Adrian et al. 2000); 4) weaker vorticity signatures in the outer regions of the boundary layer ($y^+ > 300$), featuring a remnant structure of decaying large scale hairpin-like motions.

Following the parameters extracted from the statistical analysis (streamwise velocity gradient at the wall, trends of Reynolds shear stress and turbulent kinetic energy), spanwise wall oscillations at the optimum oscillating frequency and amplitude appear to simultaneously reduce skin-friction, the turbulence production and the wall-normal velocity fluctuations. The following analysis focuses on the organisation of the coherent flow structures under these conditions.

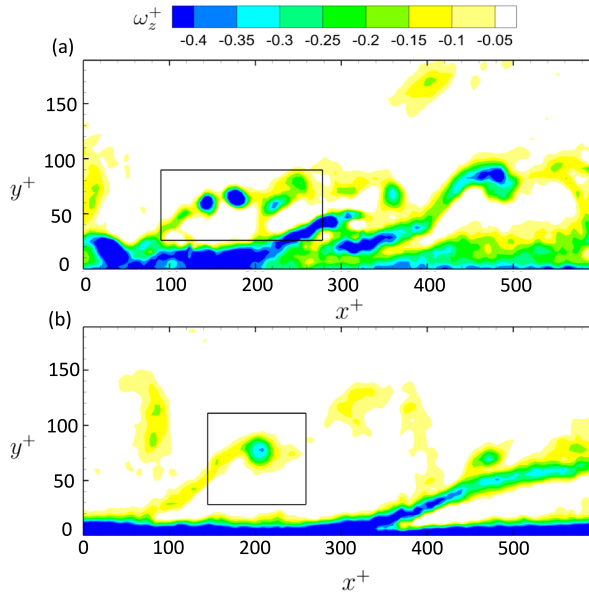


Figure 4.9: Instantaneous spanwise vorticity distribution up to $y^+ = 200$, revealing a compact arrangement of hairpins (packet signature) for the stationary wall (a) and separated structures for the oscillating wall (b).

A hairpin packet features the presence of multiple hairpin vortices with their heads aligned approximately along a 30°-degree slope from the wall and separated by approximately 120-160 wall-units in the streamwise direction (Adrian et al., 2000). The hairpins appear atop the low-speed streaks where they tend to auto-generate, which leads to the packets (Zhou et al., 1999). In the present experiments, it is observed that for the stationary wall, hairpin packets are observed to be most frequently composed of 3 – 5 vortices typically separated by 50 to 150 wall units.

A marked difference is found for the case of the oscillating wall, where the hairpins appear more frequently as isolated or in pairs, packets with more than 2 hairpins being only seldom observed. Figure 4.9 depicts a typical sample of this situation, whereas Figure 4.9 displays a sequence of vorticity measurements for the stationary and oscillating wall.

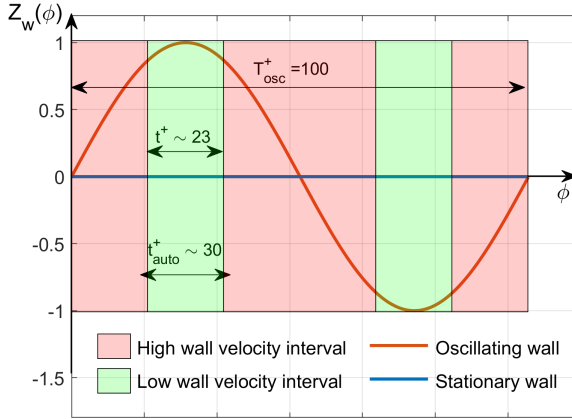


Figure 4.10: Schematic illustration of the wall oscillations time diagram and indication of hairpin packet formation time.

The smaller size of the hairpin packets observed in the boundary layer developing over the oscillating wall is ascribed to the rapid sideways motion of the wall affecting the flow structure underneath the hairpins. It is hypothesized that the sudden shift of the low- and high-speed streaks beneath the hairpins inhibits the auto-generation of vortices as a result of the relative lateral shift between the preceding hairpin and the newly forming one. For a stationary wall, the presence of the leading hairpin and its induced ejection leads to the formation of a following structure, resulting in the continuous growth of the hairpin packet (Jodai and Elsinga, 2016; Zhou et al., 1999). Figure 4.10 provides an illustration that combines the timing diagram of the spanwise oscillatory motion of the wall $Z_w(\phi)$, with a qualitative indication of hairpin formation and auto-generation period (t^+_{auto}). Given the linear relation between time and the oscillation phase ϕ , the latter is used in the remainder to refer to a specific condition within the oscillatory motion. The inhibition of auto-generation is expected to be most effective during the time interval of maximum wall velocity (red region in Figure 10), whereas during the time of motion inversion (green region) the low wall velocity produces a situation similar to the stationary case.

Based on the above, the dynamic behaviour in the regime of wall oscillations is expected to display hairpins mostly generated during the period of minimum lateral velocity (motion inversion, the green region in Figure 4.10). For an oscillating frequency of 15 Hz, which corresponds to a $T_{osc}^+ = 100$ (16.6 ms), the motion inversion time corresponds to a $t^+ = 23$. The latter is shorter than the auto-generation time $t_{auto}^+ \sim 30$ reported in the study of Jodai and Elsinga (2016) who estimated it from tomographic PIV measurements in a completely turbulent environment. Instead, Zhou et al. (1999) studied the case of auto-generation by observing the development of an initial perturbation to laminar flow with a mean turbulent velocity profile. In their work, values of t^+ one order of magnitude larger are reported compared to the observations in the turbulent regime. The time spent during motion inversion of the current experiments corresponds to approximately that taken for the auto-generation of a single hairpin, which possibly explains the occurrence of single hairpins or, at most, hairpin pairs in a packet.

Following the stage of motion inversion, the high rate of lateral shift causes the fluid adjacent to the wall (streaks) to move with it as discussed by Toubert and Leschziner (2012). The lower end of the hairpin vortices (legs) and in particular the newly generated hairpin is most affected by the lateral displacement as these parts are displaced away from the preceding hairpins and their induced ejection (low-speed region). This circumstance interrupts the auto-generation mechanism until the subsequent point of inversion when another low-velocity period allows auto-generation to some degree.

4.3.5. TOMOGRAPHIC PIV FLOW VISUALIZATIONS

The tomographic measurement volume encompasses primarily the buffer layer ($y^+ = 20 - 70$, section III a). Visualizations of the streamwise velocity distribution close to the stationary wall ($y^+ = 20$, Figure 4.11a) return the streaky pattern as a series of elongated low-speed regions with spanwise separation of approximately 100 wall units and a length varying from 600 to more than 850 wall units (current streamwise extent of the measurement domain). In agreement with the values widely reported in the literature Kähler (2004); Kline et al. (1967); Smith and Metzler (1983). Increasing the distance from the wall up to $y^+ = 80$ (Figure 4.11 b), the streamwise coherence of the streaks diminishes and these regions appear as wider and often interrupted. Also, these observations agree with the study of Jodai and Elsinga (2016), which indicates that the velocity fluctuations in these two regions are governed by different structures and they are convected at different speeds (Del Alamo and Jiménez, 2009).

The inspection of the streamwise velocity contours at a wall-normal height of $y^+ = 20$, for the stationary and the oscillating wall at $Z(\phi) = 0$ ($\phi = 0, \pi$, Figure

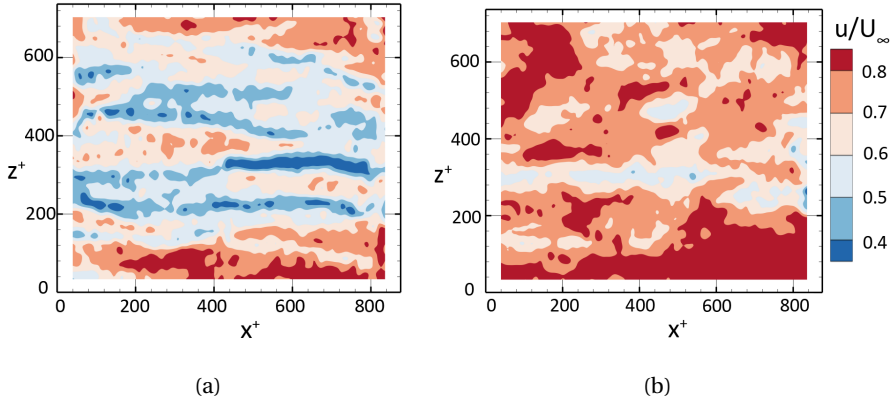


Figure 4.11: Streamwise velocity contours at two wall-normal distances, $y^+ = 20$ (a) and 80 (b).

4.12), shows that oscillations lead to a significant weakening of the streamwise coherence of the streaks, with elongated low-velocity regions being more prominent for the stationary wall case. There are also regions within the field of view which are devoid of streaks for the oscillating wall (Figure 4.12(b)), which has been also observed in the DNS study of [Touber and Leschziner \(2012\)](#). A thorough inspection of the occurrence of this flow phenomenon is possible in the series of visualisations of the velocity contours annexed in Figure 4.12. However, the DNS studies of oscillating wall ([Touber and Leschziner, 2012](#)) do not discuss the mechanism of drag reduction from the perspective of the hairpin packets. Rather, the drag reduction is ascribed to the weakening of the streaks. While the latter are important in near wall turbulence, their connection with the Reynolds shear stress, i.e. the turbulence contribution to the drag is weak, or indirect, at least. This can be inferred from the fact that the streamwise velocity fluctuations associated with the streaks are confined to a region very close to the wall ($y^+ \sim 15$), while the Reynolds shear stress peaks at a larger wall normal distance (Figure 4.4). Hairpins and packets, however, are correlated with Reynolds stresses ([Ganapathisubramani et al., 2003](#)), hence turbulent drag. So the development of hairpins (possibly from the streaks) provides a link between streak strength reduction very close to the wall and the reduction in Reynolds stresses farther from the wall.

A sample of the three-dimensional organisation of vortices (iso-surface of the λ_2 -criterion) and positive wall-normal velocity fluctuations v' is shown in Figure 13, along with the streamwise velocity u distribution over a plane at position $y^+ = 20$, which identifies the high- and the low-speed regions. The flow field for

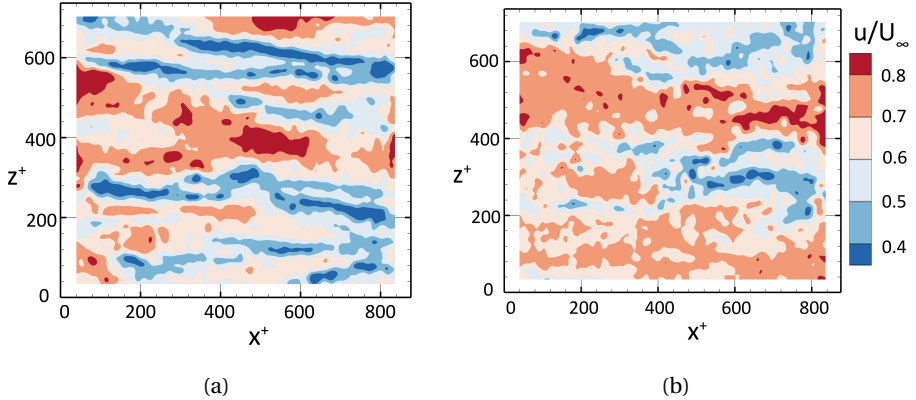


Figure 4.12: Streamwise velocity contours over a stationary (a) and oscillating wall ($T_{osc}^+ = 94$, b) at wall-normal distance of $y^+ = 20$.

the stationary wall case (Figure 4.13(a)) features several elongated regions with wall-normal velocity fluctuations (purple) surrounded by multiple vortical structures (green) enclosed in boxes (1 to 7 in Figure 4.13(a)). This arrangement is in accordance to the concept of the hairpin packets, where the primary hairpin vortex being formed develops downstream and gives rise to a secondary hairpin vortex (Adrian, 2007). This mechanism is ascribed to the interaction of the low-speed fluid in the streak (purple in Figure 4.13) that is ejected between the legs of the hairpin with the high-speed fluid above the legs causing the roll-up, in turn forming an arch-like structure (Jodai and Elsinga, 2016; Zhou et al., 1999). The supplementary material provided in Figure 13, illustrates in a more extended way the above experimental observations for the stationary and oscillating wall. For the oscillating wall, the data at $\phi = 0$ and $\phi = \pi$ are shown. In the sample showing the instantaneous flow field for the oscillating wall (Figure 4.13(b)), the presence of wall-normal velocity fluctuations is significantly smaller. The low-speed flow regions are less pronounced (Figure 4.13(b)), in turn inhibiting the process of hairpin formation and auto-generation. The organisation of vortical structures (Figure 4.13, enclosed in boxes) above the oscillating wall (1, 2 and 3 in Figure 4.13(b)) features mostly a streamwise orientation, and are significantly sparser, when compared to the stationary wall. Moreover, arch-like structures appear less frequently and seldom arranged into packets. This further inhibits hairpin formation, since isolated hairpins need to be much stronger to initiate auto-generation as compared to hairpins in a packet, which can be weak and still trigger auto-generation (Goudar et al., 2016). Such strong hairpins have a very low probability.

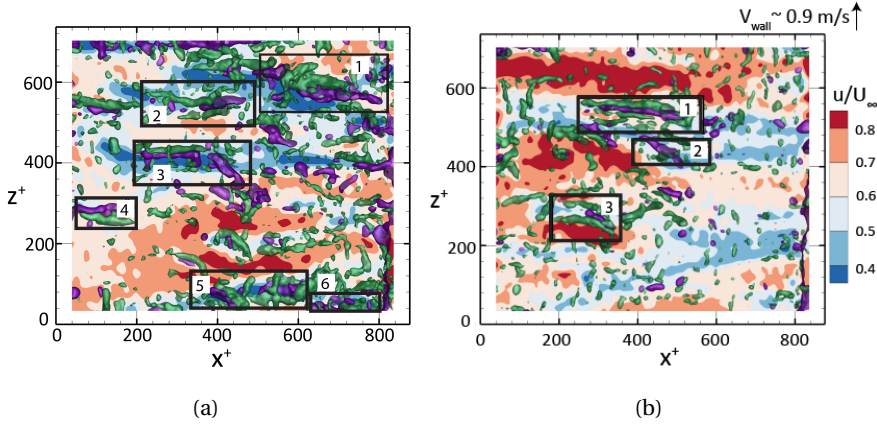


Figure 4.13: 3D-visualization of Tomographic-PIV data over a stationary (a) and oscillating wall ($T_{osc}^+ = 94$, b); iso-contours of $\lambda_2 = -20,000[1/s^2]$ (green) and $v = 0.1U_\infty$ (purple) at $y^+ = 20$.

Statistical evidence of this effect can be gathered considering the flow enstrophy ω^2 as an overall measure of the vorticity fluctuations over the domain of observation ($20 < y^+ < 80$) as shown in Table 4.6.

Table 4.6: Mean Enstrophy quantified in the Tomographic-PIV domain.

Stationary wall [s^{-2}]	Oscillating wall [s^{-2}]	
	$\phi = 0, \pi$	$\phi = 0.5\pi, 1.5\pi$
$1.98 \times 10^4 s^{-2}$	$1.54 \times 10^4 s^{-2}$	$1.65 \times 10^4 s^{-2}$

The mean value of ω^2 is $1.98 \times 10^4 s^{-2}$, for the stationary wall, whereas, while for the oscillating wall it reduces to $1.54 \times 10^4 s^{-2}$ at $\phi = 0, \pi$ (maximum velocity). A slightly higher value ($\omega^2 = 1.65 \times 10^4 s^{-2}$) is observed during motion inversion ($\phi = \pi/2, 3\pi/2$), indicating that the turbulent properties also depend upon the phase of the oscillatory motion. The latter correlates to the reduction in vortical structures described earlier and is consistent with the proposed mechanism of auto-generation inhibition. Albeit for a different geometry (circular pipe flow), [Coxe et al. \(2019\)](#) performed a DNS study, proposing a phase dependence of vorticity fluctuations with transverse wall oscillations too.

4.3.6. PROPOSED PHYSICAL MECHANISM

The proposed model for the effect of wall oscillation on hairpin packet formation is graphically conceptualised in the schematics of Figure 4.14.

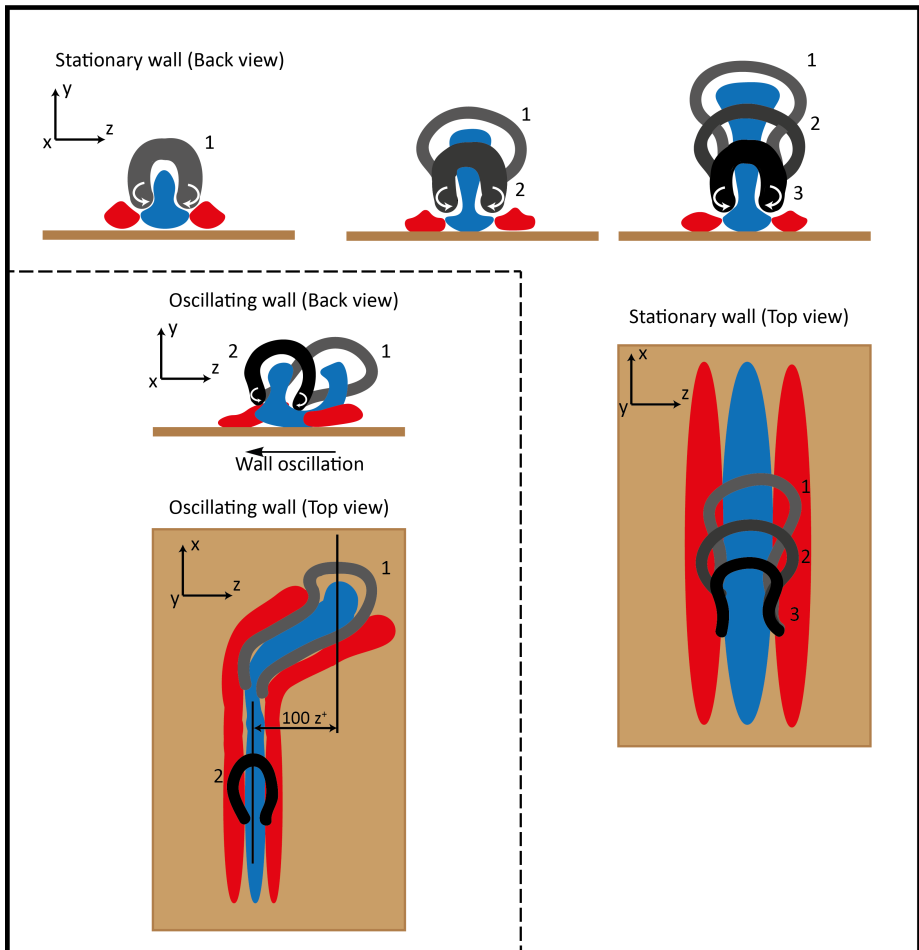


Figure 4.14: Illustration of hairpin auto-generation for stationary and oscillating wall (Red: high-speed streaks, Blue: low-speed streaks, shades of grey used to represent different hairpins and are numbered (1,2,3)).

The auto-generation of the hairpin packet is sketched for the stationary wall (Figure 4.14-top), the blue region corresponds to the low-speed streak, which is lifted up. The ejection is intensified as the hairpin packet grows in size, with the current illustration depicting the formation of a packet of 3 hairpins (1, 2 and 3 in 4.14-stationary wall). For the oscillating wall (4.14-oscillating wall) an initial hairpin (1, 4.14-oscillating wall) cannot auto-generate downstream due to the rapid lateral shift of the trailing flow region, at a lower distance from the wall. The transverse wall motion also distorts the streaks, however, this is not regarded as the main inhibition factor, compared to the increased distance between the

focused ejection from the preceding hairpin vortex and the trailing region. In turn, the formation and growth of the trailing hairpin (2, 4.14-oscillating wall) will occur independently and without the accelerating effect of auto-generation. As a result, the pattern of isolated hairpins reduces the collective focused ejection of the low-speed fluid, with a significant reduction of momentum mixing, which directly translates into a reduction in skin-friction drag.

4.4. CONCLUSION

The response of a turbulent boundary layer developing over a spanwise oscillating wall has been studied experimentally employing planar and tomographic PIV. High-resolution planar PIV allowed to accurately measure the wall shear stress directly from the velocity profile down to a wall-normal distance of $y^+ = 2$. A maximum drag reduction of 15% is quantified for the oscillating wall at $T_{osc}^+ = 94$ and $A_{osc}^+ = 100$, when compared to the stationary wall. The reductions obtained are found in agreement with previously reported DNS studies. A significant reduction of turbulent stresses as well as of pre-multiplied turbulent kinetic energy production is found up to $y^+ = 100$. The instantaneous vorticity fields visualized in the planar and tomographic-PIV measurements reveal marked differences between the stationary and the oscillating wall. Planar data provide evidence through the visualizations of the cross-sectional footprints of these highly three-dimensional coherent structures. A hypothesis is forwarded to provide an explanation for the observed reduction in near-wall vorticity and accompanying reduction of the number of hairpins in a hairpin packet when the wall is oscillated. According to the proposed mechanism, and existing literature on hairpin packet generation, the oscillation frequency may be associated to the size of the packet, whereas the amplitude of oscillation needs to be at least as large as the streaks spanwise separation to be effective. In line with this model, the hairpin packet formation depends on the motion of the oscillating wall and as such on the phase in the oscillation cycle. Quantitative information from the tomographic PIV data supports this assumption, where the enstrophy in the field reduces by 22% for the oscillating wall at $\phi = 0, \pi$ and by 16.7% for the oscillating wall at $\phi = \pi/2, 3\pi/2$.

5

DISTORTION OF COHERENT STRUCTURES IN TDR REGIME

*Ask the right questions,
and nature will open, the doors to her secrets.*

Sir CV Raman

The current chapter attempts to quantify the systematic distortions of the dominant turbulent structures by feature-analysis, intended to overcome the dispersion observed in pointwise statistics and correlation functions. Furthermore, data from tomographic particle image velocimetry is employed to clarify the mechanism that inhibits hairpin auto-generation, as described in [Kempaiah et al. \(2020\)](#) and Chapter 4.

Based on the instantaneous distribution of Reynolds stresses, a specific spatial template is defined for low-speed streaks and flow ejections. Events corresponding to this template are collected and parametrised with their occurrence, geometrical properties (length and orientation), and dynamics (intensity). The approach is compared with most practised statistical analysis to explain the significance of the features extracted by the detection algorithm in relation to the drag reduction mechanism.

Parts of this chapter have been published in [Kempaiah and Scarano \(2022\)](#).

5.1. INTRODUCTION

In chapter 4, direct wall-shear measurements were performed using high-resolution planar particle image velocimetry (PIV). Skin-friction reductions of up to 15% were quantified for a turbulent boundary layer (TBL) at $Re_\theta = 1000$. The quantitative visualisation of velocity and vorticity fields by planar and tomographic PIV suggested that the principal mechanism of such reduction lies in the inhibition of hairpin auto-generation near the wall due to the distortion of the low-speed streaks underneath. Furthermore, the availability of streamwise-wall normal velocity distribution from the fully 3-dimensional velocity field from tomographic PIV experiments provides the opportunity to quantitatively analyse the effect of wall oscillations on the coherent structures in the flow.

The observation of structures in a TBL is well documented in literature from flow visualisation experiments and DNS (Section 2.1). Kline observed streamwise elongated features of high and low velocity in the near-wall regions, termed streaks. The low-speed streaks were observed to oscillate as they were lifted from the wall leading to ejections and sweeps, which are ascribed to the production of Reynolds shear stresses (RSS) and turbulent kinetic energy (TKE). The first DNS simulations by Moin and Kim (1985) showed the presence of hairpins through the visualisations of vorticity lines in the vicinity of Q2 events, strengthening the interlink between hairpins and ejection events. The subsequent development of PIV enabled quantitative visualisations of two-dimensional instantaneous flow fields. Adrian et al. (2000) reported the existence of vortices that were interpreted as heads of hairpins which were previously observed to account for the Q2 and Q4 Reynolds shear stresses. The model of hairpin packets was proposed based on the findings from planar-PIV.

Furthermore, Tomographic PIV measurements by Jodai and Elsinga (2016) captured the hairpin auto-generation process through time-resolved measurements and reported that hairpin auto-generation time is 30 wall-scaled time units. Ganapathisubramani et al. (2003) used planar-PIV data in the wall parallel plane to implement a feature detection algorithm to assess the contribution to the RSS by a packet of hairpins. Recent work by Bae and Lee (2021) analysed the life cycle of streaks in the buffer layer by tracking streaks in spatially and temporally resolved flow fields by applying feature detection based on a threshold value. However, the literature does not report the response of streaks and ejections to wall oscillations. The combination of conditional sampling and the 3-dimensional experimental data enables the application of feature detection techniques tailored to identify and analyse the features to understand the effect of the wall oscillations.

From the mechanism proposed in Chapter 4 (Kempaiah et al., 2020), the rapid distortion of the streaks at their tail significantly inhibits the formation

and growth of new “younger” hairpins from a pre-existing packet. As a whole, this condition impedes hairpin auto-generation. Such distortion has been hypothesised and qualitatively visualised and illustrated. However, quantifying distorted features like streaks, ejections, and reduction in the number of hairpins occurring in a packet has not been afforded due to the complexity of their three-dimensional organisation and jittery occurrence. The present work employs the tomographic PIV data and compares a feature detection algorithm with the more commonly used spatial correlation operators. To this end, Tomographic PIV phase-locked data provides the opportunity to examine the details of the distortion mechanism by phase-averaged analysis during the oscillatory motion of the wall.

5.2. EXPERIMENTAL SETUP AND PROCEDURE

5.2.1. FLOW FACILITY AND BOUNDARY LAYER PROPERTIES

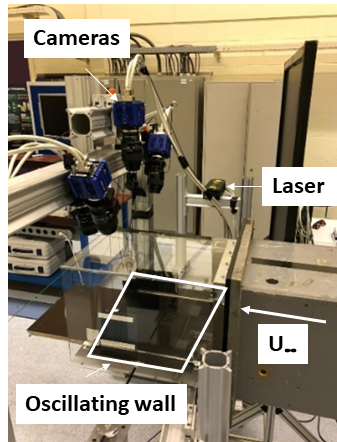


Figure 5.1: Photograph of the Tomographic-PIV setup in the W-tunnel.

The experiments were conducted in the open-return low-speed facility W-tunnel at the faculty of aerospace engineering at TU Delft (see Figure 5.1). For more details regarding the experimental setup, data acquisition and PIV processing parameters, the reader is referred to [Kempaiah et al. \(2020\)](#). The turbulent boundary layer properties were calculated from planar-PIV data and are summarised in Table 4.1 in Chapter 4.

5.2.2. TOMOGRAPHIC PIV AND ASSESSMENT OF MEASURED VELOCITY

The 3-dimensional velocity fields within the TBL were measured by tomographic PIV ([Elsinga et al., 2006](#)). The measurement volume for tomographic-PIV is placed

0.25 m (2500 wall units) downstream of the leading edge of the oscillating wall with the dimensions of $70 \times 60 \times 5.7 \text{ mm}^3$, corresponding to $700 \times 600 \times 57$ wall units in the streamwise, spanwise and wall-normal direction (refer Figure 5.2(a)). The average imaging magnification is $M = 0.2$, with a digital resolution of 32 pixels/mm. The instantaneous particle distribution was reconstructed by implementing the MART tomographic algorithm with five iterations (Elsinga et al., 2006). The cross-correlation analysis returns $293 \times 246 \times 24$ velocity vectors using an interrogation volume size of 323 voxels giving a vector spacing of 0.25 mm (2.5 wall units) with 75% overlap. Phase averaged acquisitions of the tomographic data were obtained at phases with a shift of $\pi/4$ in the sinusoidal oscillations ($Z(\phi) = A_{osc} \sin(\phi)$) of the wall at phase interval of $\pi/4$. The conditions $\phi = 0$ and $\phi = \pi$ are labelled as “high-speed”, $\phi = \pi/4$ and $\phi = 5\pi/4$ as “decelerating”, $\phi = \pi/2$ and $\phi = 3\pi/2$ as “low-speed”, and $\phi = 3\pi/4$ and $\phi = 7\pi/4$ as “accelerating”. Differently from the tomographic-PIV experiment, in the data from the planar-PIV, the phase of oscillation is not monitored.

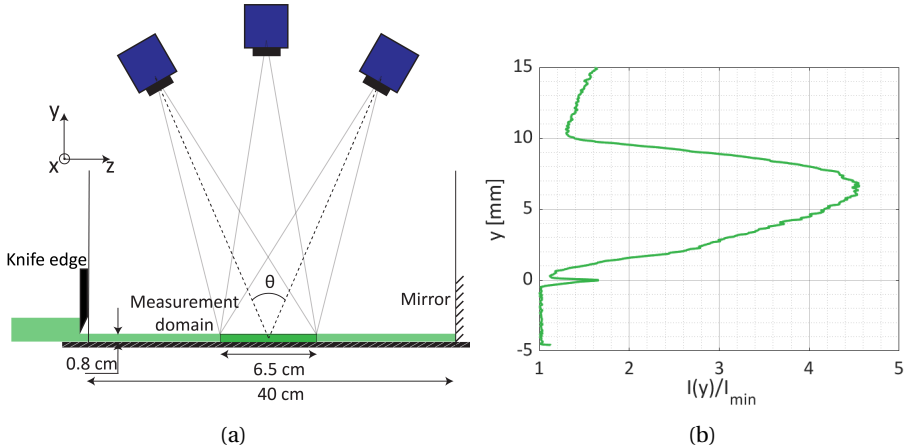


Figure 5.2: Illustration of the tomographic setup (a); Average particle light intensity reconstruction $I(y)$, in the wall-normal direction. (Normalized to the minimum intensity (I_{min})) (b).

The position of the wall within the measurement volume was determined by plotting the average particle light intensity reconstruction ($I(y)$) normalised to the minimum intensity (I_{min}) in the domain (Figure 5.2(b)). The error in the position of the wall was found to be $300 \mu\text{m}$ corresponding to 3 wall units, and has been corrected, leaving an uncertainty of $50 \mu\text{m}$. The mean velocity profile returned by tomographic PIV compares well with both the planar PIV measurements and the DNS data at $Re_\theta = 1000$ by Schlatter and Örlü (2010) (Fig-

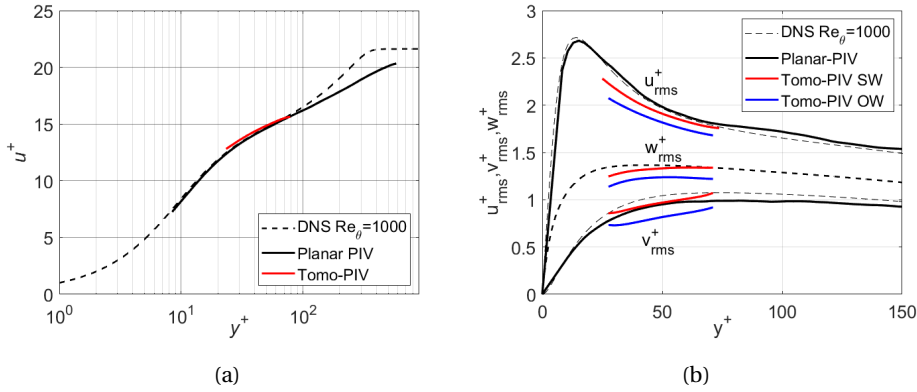


Figure 5.3: Mean (a) and r.m.s. (b) velocity profiles returned by tomographic PIV using cubic and elongated correlation volumes were compared against the DNS database of Schlatter and Örlü (2010), and the planar-PIV data from Kempaiah et al (2020) scaled with u_τ of the stationary wall (SW).

ure 5.3(a)). For the tomographic measurements, the inspected volume spanned a limited wall-normal range ($20 < y^+ < 70$) due to the light intensity decreasing close to the wall, leading to a more frequent occurrence of ghost particles. Therefore, the measurement volume is limited in the above range. The root mean square (r.m.s) fluctuations of the velocity components are presented and compared against the same DNS database in Figure 5.3(b). It is clear from the streamwise velocity component that the near-wall peak at $y^+ = 15$ has not been captured. The u_{rms}^+ profiles show lower values with respect to the DNS, but the difference remains within 6%, similar to other studies employing the same technique (Jodai and Elsinga, 2016). Based on the observations, the data is considered suited for the analysis of instantaneous flow features in the range of $20 < y^+ < 70$.

5.2.3. DATA REDUCTION

TWO-POINT CORRELATION

The statistical analysis of velocity fluctuations in turbulent boundary layers is most frequently performed by spatial two-point correlation (Tong et al., 2022). Early adoption of the technique for three-dimensional tomographic datasets is reported by Schröder et al. (2011). The two-point correlation R between two quantities A and B is defined as

$$R_{AB} = \frac{\overline{A(x, y)B(x + \Delta x, y + \Delta y)}}{\sigma_A \sigma_B} \quad (5.1)$$

Where the product $\sigma_A \sigma_B$ normalises the upper inner product by the standard deviation of the quantities, respectively. Given that the process of turbulent kinetic energy production is linked to the ejections ($u'v'$) and to the low-speed streaks (u'), the velocity fluctuations in the streamwise (u') and wall-normal (v') direction will be analysed.

FEATURE DETECTION ALGORITHM

As opposed to two-point correlations, feature detection is based on a segmentation of the spatial domain. Most commonly, the segmentation criterion requires defining a threshold value for the property of interest. Here, we refer to the level of velocity fluctuations (refer to Figure 5.5(a)) as obtained from tomographic-PIV. Streaks and ejections are the features of interest, and they are expected to be approximately aligned in the streamwise direction for the stationary wall. The sidewise motion propagating through the Stokes layer, instead, causes the lower portions of these features to move sideways, causing their side-tilt. It is expected, based on the hairpin-packets paradigm (Adrian, 2007; Adrian et al., 2000; Jodai and Elsinga, 2016), that the aft part of such ejection regions is also at a lower distance from the wall.

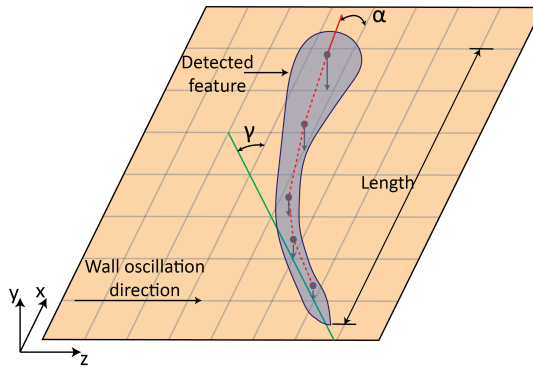


Figure 5.4: Schematic illustration of a turbulent structure undergoing distortion due to wall oscillation. Vertical arrows indicate the wall-normal distance. For the given condition, the tail is expected to be shifted sidewise producing an overall tilt (γ).

Detection functions are defined in Table 5.1 for the streamwise velocity fluctuations ($F_d^{u'}$, low-speed streaks) and the product of streamwise wall-normal fluctuations ($F_d^{u'v'}$, ejections). Such functions are normalised to the local fluctuation by the global root mean square value (u_{rms} , v_{rms} , w_{rms}) of the stationary wall. The detection algorithm adopted here is similar to that reported by Martins et al.

Table 5.1: Summary of the feature detection algorithm.

Coherent structure	Detection function	Condition	Threshold(F_t)
Low-speed streaks	$F_d^{u'} = \frac{u'(x,y,z)}{u'_{rms}(y)}$	$F_d^{u'} < F_t^{u'}$	-1
Ejections	$F_d^{u'v'} = \frac{u'v'(x,y,z)}{u'v'_{rms}(y)}$	$F_d^{u'v'} < F_t^{u'v'}$ AND $F_d^{u'} < 0$	

(2019). It is described in the following steps, and it is illustrated in Figure 5.5.

The quantities of interest for these features are their size (length), spatial occurrence and inclination. For the latter, the rotation with respect to the streamwise axis in the x-y plane is termed α (pitch), and in the x-z plane is termed γ (tilt). The above is schematically illustrated in Figure 5.4, where a detected feature is pictured while affected by the wall motion. A reference value for the tilt angle γ_0 can be inferred from the ratio of amplitude oscillation and the length of the distorted structure.

$$\gamma_0 = \tan^{-1} \frac{A}{L} \quad (5.2)$$

For the present conditions, $\gamma_0 = 25^\circ$, where the amplitude (A) is 100 wall units, and the average length (L) of a typical structure is 200 wall units (refer to Table 5.2). However, the latter may overestimate the actual tilt, which is reduced under the effect of streamwise convection and under the effect of the shear in the Stokes layer during the side oscillation.

The detection algorithm is summarised in the following three steps:

1. Definition of the fluid dynamic property

The velocity fluctuations in the 3D domain (u' , v' , Figure 5.5(a)) are chosen as a basis to define a detection function ($F_d^{u'}$: streaks, $F_d^{u'v'}$: ejections) as the ratio of the local velocity fluctuation with the r.m.s fluctuations ($u'_{rms}(y)$, $u'v'_{rms}(y)$) at the corresponding height for the stationary wall. Figure 5.5(b) and Figure 5.5(c) show such detection functions for the streamwise and streamwise-wall-normal fluctuations.

2. Detection criteria (thresholding)

A threshold value (F_t) for the detection function is used that identifies the boundary of the segmented region for the low-speed streaks ($F_d^{u'} < -1$) and ejections ($F_d^{u'v'} < -1$ AND $F_d^{u'} < 0$) events. Based on each criterion, the segmented domain is labelled by a logical (0,1) operator.

3. Ensemble of selected structures

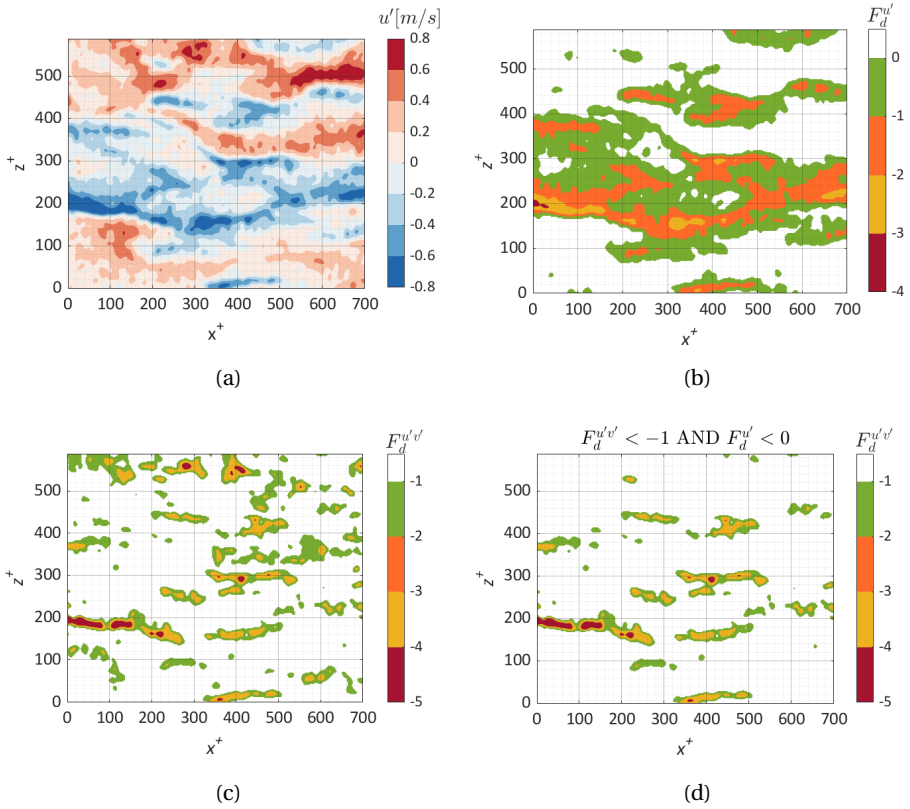


Figure 5.5: Illustration of the feature detection algorithm used for identification of streaks and ejection events from the u' velocity field (a), detection of the streaks (b) detection of the ejection and sweep events (c) and finally the identified ejection events based on the described detection function (d); The data is from the case of the stationary wall (SW) and corresponds to the wall parallel plane at $y^+ = 20$.

Regions that simultaneously satisfy the above two conditions are considered relevant to the analysis as they correspond to the physical mechanisms of interest, i.e. where the flow exhibits significantly retarded flow and considerable ejection activity. Figure 5.5(d) represents the detected ejection, sectioned at a given wall parallel plane. Table 5.1 summarises the algorithm and its parameters.

The ejection events detected in Figure 5.5(d) correspond to the flow regions where low-speed fluid is lifted away from the wall. To obtain quantitative information (length and spatial occupation) from these features in the wall parallel plane, the concept of connected components is employed as outlined by Haral-

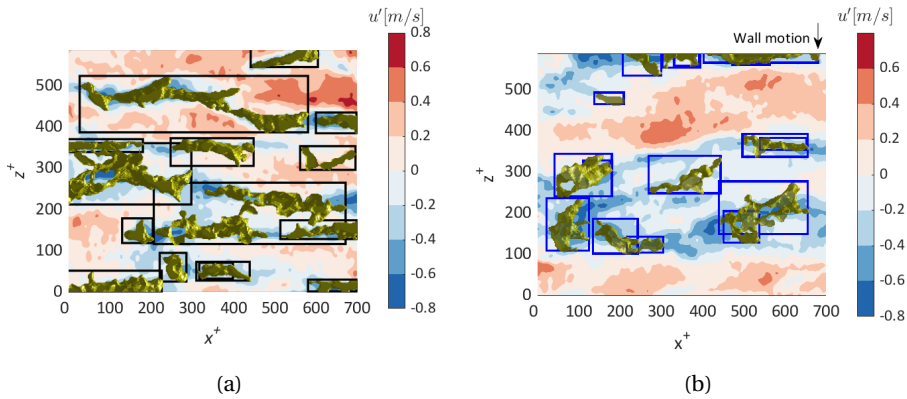


Figure 5.6: Iso-surface of ejection events detected through the 3D feature detection algorithm enclosed in boxes for the case of the stationary wall (a) and oscillating wall (OW). The isolated features enclosed in boxes are analysed further.

ick et al. (1992). The method is implemented through the Matlab function (`bwlabel`), which analyses a 2D binary field (i.e. within a specific plane). By such analysis, data points pertaining to the detected streaks and ejections (Figure 4d) are labelled as ones. Such points are clustered based on 8-neighbours connectivity (i.e. North(N), South(S), East(E), West(W), NE, NW, SE, SW). After this operation, each detected feature is accepted, and the specific information can be extracted. Intrinsic properties are the length and the angle, whereas global properties are their occurrence and spatial occupation. Both are reported and discussed in the next section.

The treatment of the features identified, however, is challenged by their highly three-dimensional features. Moreover, quantities of interest like length and inclination (as described in Figure 5.5) require the detection of the structures in the whole domain (i.e. in 3-dimensions). The 3D binary matrix consisting of features represented by ones is clustered by using the function `region3props`, which implements the same procedure described by Haralick et al. (1992) but for a 3D volumetric image regions by creating a 3D bounding box around the detected regions as shown in Figure 5.6(a) (SW) and Figure 5.6(b) (OW corresponding to $\phi = \pi/4$) for the stationary and oscillating wall conditions.

The length and inclination of these features are obtained by singular value decomposition of the detected regions. The resulting eigenvector (corresponding to the first mode) yields the orientation of the principal axis (red in Figure 5.7), which minimizes the orthogonal square distance (between the axis and the data points). An example is shown in Figure 5.7 for a chosen feature. It should be retained in mind, however, that the maximum values of vertical inclination (α)

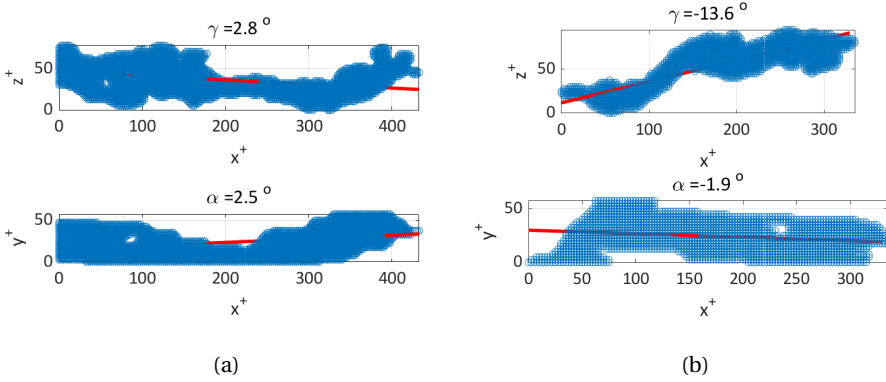


Figure 5.7: Detected features corresponding to an ejection event for the case of the stationary wall (a) and oscillating wall for $\phi = \pi/4$ (b) with the SVD Eigen vector (in red) which is used to extract the vertical inclination or pitch (α) and spanwise tilt (γ).

5

that can be detected are limited by the measurement domain wall normal range of 50 wall units. The individual features reported in Figure 5.7 show a smaller sidewise tilt angle of 2.8° for stationary wall, whereas the tilt increases to -13.6° when the wall oscillates (during downward motion, arrow in Figure 5.6(b)). The motion of the wall results in a rapid lateral distortion of the ejection events. Close to 500 structures were identified for each phase of the OW and 2000 for the SW. A collection of identified ejection structures is shown in Figure 5.7.

5.3. RESULTS AND DISCUSSION

5.3.1. ANALYSIS BY SPATIAL CORRELATION

The two-point statistical correlation of the streamwise velocity fluctuations (u') is a common tool to inquire about streamwise velocity coherence. This operator returns the pattern of the coherent fluctuations and gives an indication of the flow arrangement into low- and high-speed streaks. The mean result of the correlation analysis is shown here in a wall-parallel ($x - z$, $y^+ = 20$) and streamwise wall-normal plane ($x - y$). For the stationary wall, the normalised two-point correlation map of $R_{u'u'}$ (referred to as R_{St1} , Equation 5.1) at a height $y^+ = 20$ and wall-normal planes $R_{u'(y^+=20)u'(y^+)}$ (referred to as R_{St2}) are shown in Figure 5.8. The correlation map for the stationary wall (SW, Figure 5.8a) exhibits an elongated structure with two side-lobes along the span. The central structure is consistent with the streaky pattern of low-high velocity fluctuations. The result for the oscillating wall (OW, ensemble average irrespective of oscillation phase) is shown in Figure 5.8b. The differences to the SW case are rather minor: for

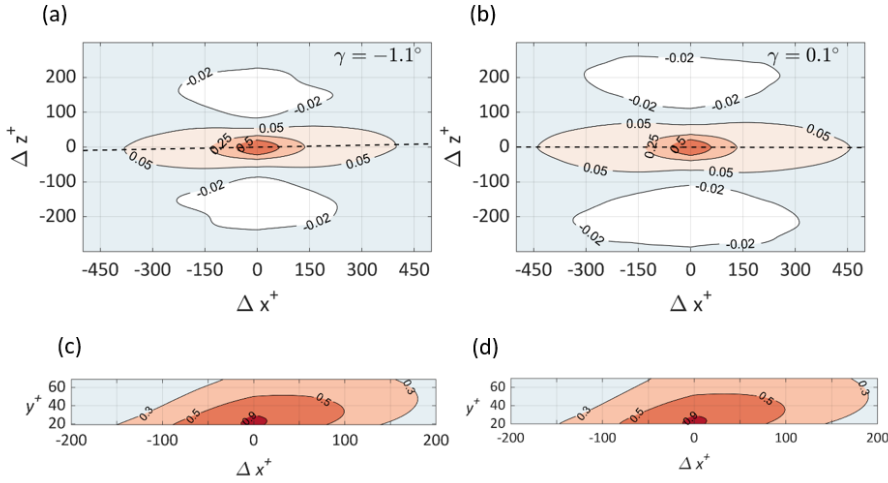


Figure 5.8: Two-point autocorrelation of streamwise velocity fluctuations (R_{St1} and R_{St2}) for stationary (SW, a and c) and oscillating (OW, b and d) wall at $y^+ = 20$.

$R_{St1} = 0.05$. The width of the correlation map is 100 wall units for SW compared to 140 for OW indicating a mild spanwise widening of the positive correlation region when the wall is oscillated. Furthermore, the corresponding length increases from 700 to 900 wall units for OW. Both observations may suggest that the wall oscillation has little to no effect on the length and spacing of the streaks, which is, however, in contrast with the instantaneous observations in Figure 5.6, where the streamwise coherence of ejection events is visibly reduced in the oscillating regime. It should be retained in mind that the correlation maps do not provide information about the intensity of these events, but inference can be made from Figure 5.3(b) where the OW is reported to have weakened fluctuations. The streamwise fluctuations at $y^+ = 20$ also correlate with the fluctuations at higher wall-normal planes (R_{St2}), as shown in Figure 5.8c and d. The correlation map indicates a region inclined with the streamwise direction in agreement with the observations of Sillero et al. (2014) corresponding to the lift up of the low-speed fluid in the head region.

The periodic nature of the wall oscillations permits the comparison of results in the $x - z$ plane for the corresponding phases of the wall oscillations. The phase dependence of the positive correlation regions corresponding to the different phases (refer to Figure 5.9) reveals minor differences. In particular, the side-angle γ lies between -1.5° and 1.5° , suggesting that the low-speed streaks

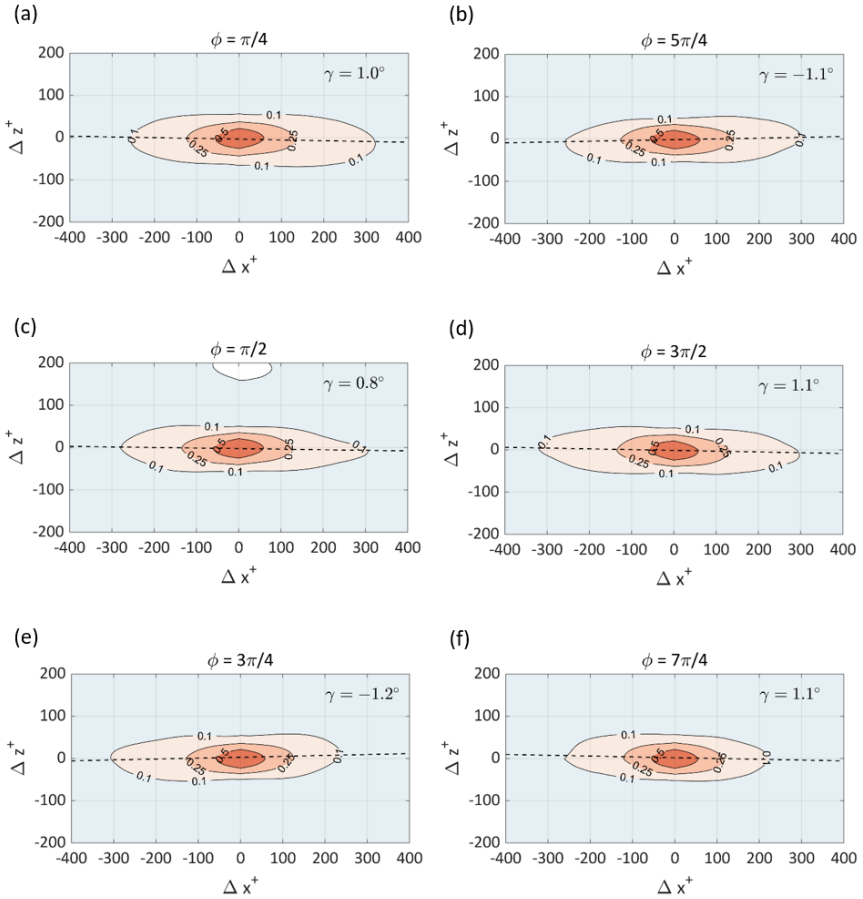


Figure 5.9: Comparison of the autocorrelation maps of the streamwise velocity fluctuations ($R_{S_{t1}}$) for the different phases of the oscillating wall. (a) $\phi = \pi/4$, (b) $\phi = 5\pi/4$, (c) $\phi = \pi/2$, (d) $\phi = \pi/2$, (e) $\phi = \pi/4$ and (f) $\phi = 7\pi/4$.

remain essentially aligned streamwise. Such a result is again in contrast with the instantaneous visualisations and may be ascribed to the statistical effect of ensemble averaging.

The analysis is extended to the product of the streamwise wall-normal velocity fluctuations $R_{(u'v')(u'v')}$ (referred as RE_{j1}) and in the wall-normal planes $R_{u'v'(y^+=20)u'v'(y^+)}$ (referred as RE_{j2}) that signify ejections events. The analysis in the streamwise spanwise plane is made by reporting the autocorrelation maps

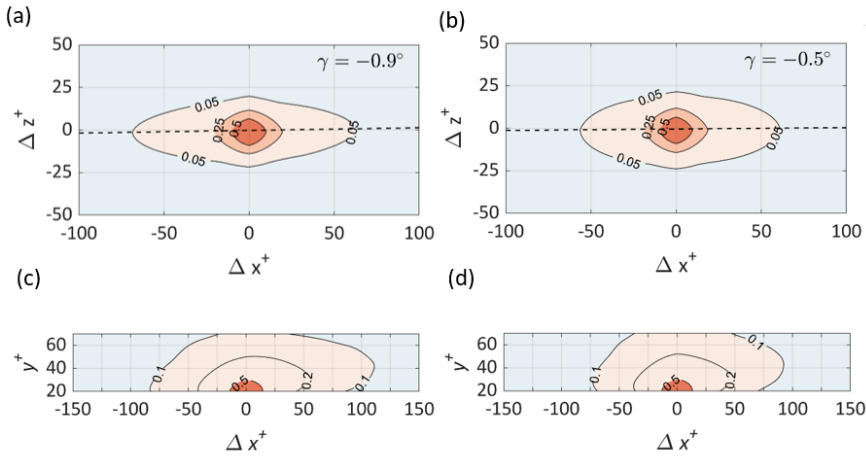


Figure 5.10: Autocorrelation map of streamwise-wall normal velocity fluctuations (R_{Ej1}) for stationary (SW, a) and oscillating (OW, b) wall at $y^+ = 20$; Correlation map of streamwise velocity fluctuations at $y^+ = 20$ with different wall-normal heights (R_{Ej2} for stationary (SW, c) and oscillating (OW, d) wall in the (wall normal x-y plane).

of R_{Ej1} at $y^+ = 20$ in Figure 5.10a (SW) and Figure 5.10b (OW). The correlation maps report a similar difference as seen for the streamwise velocity fluctuations, i.e. increase in width (Δz^+) and decrease in length (Δx^+) for the OW corresponding to $R_{Ej1} = 0.05$. The product of the streamwise wall-normal velocity correlations in the wall-normal plane follows the same procedure as that adopted for the streamwise velocity fluctuations. Figure 5.10c (SW) and Figure 5.10d (OW) report R_{Ej2} , indicating that SW ejections tend to be pitched up ($\alpha > 0$), whereas for OW a more symmetric shape suggests no pitch ($\alpha \sim 0$). The inclination is a characteristic feature of near-wall turbulence which arises due to the lift-up of low-speed fluid into higher layers. The phase averaged results in the x-z plane reveal some effects of the wall oscillations (Figure 5.11). The sidewise tilt (γ) follows the motion of the wall, as shown already in Figure 5.10, but the amplitude of the sidewise tilt is threefold higher (i.e. γ is close to 1° for streaks and 3° for ejections). At $\phi = \pi/4$ and $\pi/2$, the wall is displaced along z and reports a negative γ (-3.5° and -3°). Followed by motion inversion for $\phi = 3\pi/4$, where γ is 1.1° (Figure 5.11e). The side tilt is lowest at $\phi = \pi/4, \pi/2$ due to the re-orienting effect during motion inversion. The phase dependence of the autocorrelation maps of $u'v'$ at $y^+ = 20$ indicates that wall oscillations do affect ejections in a more pronounced way than the streaks.

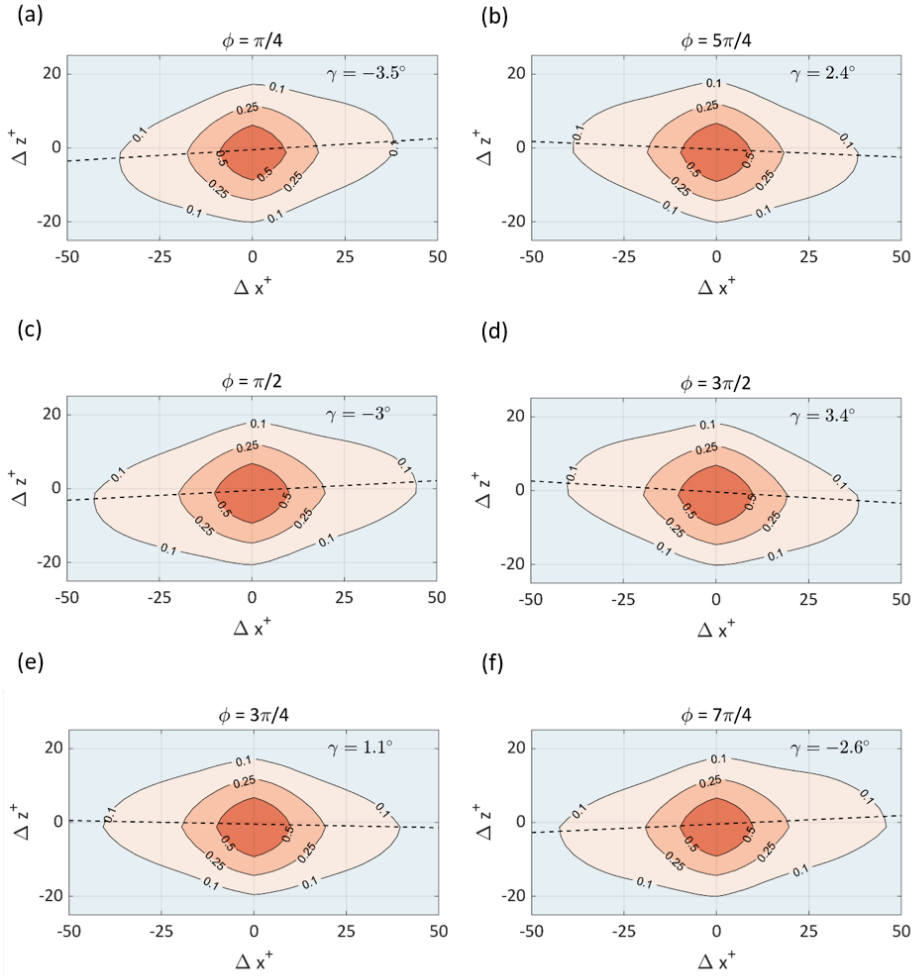


Figure 5.11: Comparison of autocorrelation maps of the streamwise-wall normal velocity fluctuations (R_{Ej1}) during the different phases of the oscillating wall. (a) $\phi = \pi/4$, (b) $\phi = 5\pi/4$, (c) $\phi = \pi/2$, (d) $\phi = \pi/2$, (e) $\phi = \pi/4$ and (f) $\phi = 7\pi/4$.

In conclusion, the analysis by two-point correlation yields some consistent trends of the distortions induced by wall oscillations. However, given the random occurrence of the turbulent structures and the diffusive nature of the correlation operator, this tool is seen as inadequate to yield detailed information on the distortion of turbulence in the presence of wall oscillation.

5.3.2. ANALYSIS BY FEATURE DETECTION

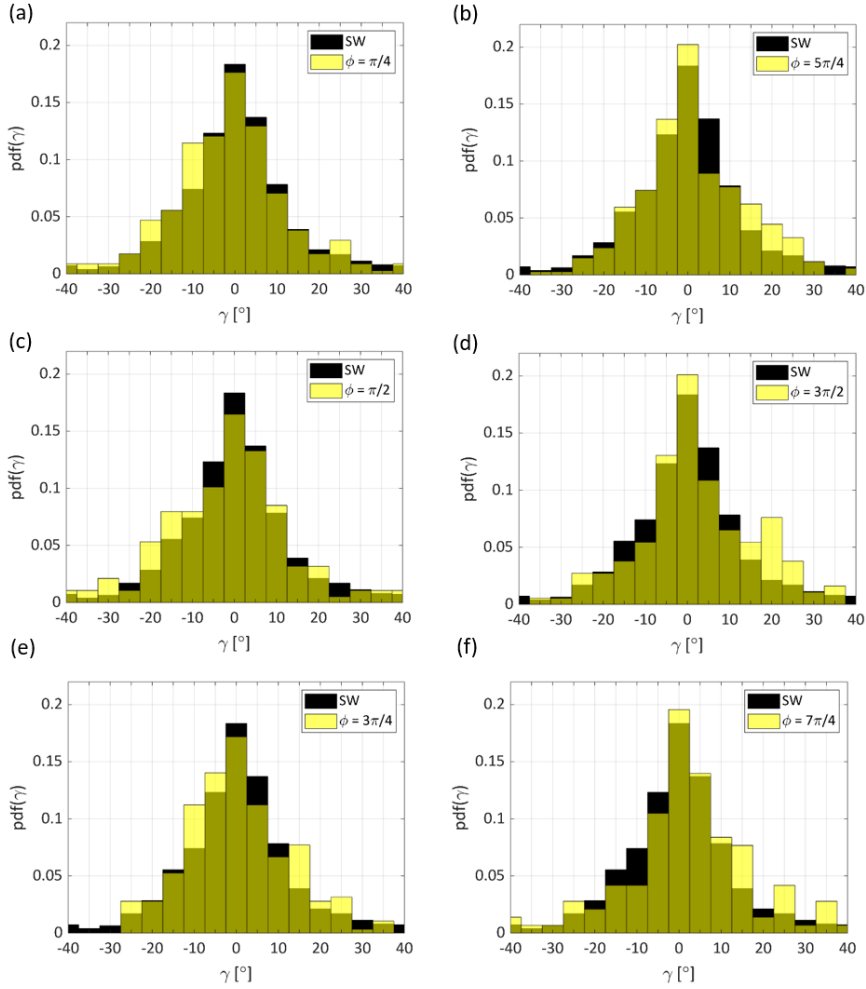


Figure 5.12: Probability distribution of sidewise tilt (γ) from detected streaks ($F_d^{u'} < -1$) at six phases of wall oscillation (a) $\phi = \pi/4$, (b) $\phi = 5\pi/4$, (c) $\phi = \pi/2$, (d) $\phi = 3\pi/2$, (e) $\phi = \pi/4$ and (f) $\phi = 7\pi/4$.

The feature detection algorithm aims to increase the observability of distortion events and infer the phase-dependent behaviour. In particular, it is expected that structure's occurrence, length, intensity and orientation be deduced more clearly from the instantaneous measurements. A more significant statistical structure is expected to emerge when performing ensemble operations after

detection and classification. The tilt angle γ is expected to be correlated to the direction of the wall oscillations, with positive and negative values corresponding to the phase of the wall oscillation. The phase-averaged occurrence of γ for the detected structures (based on streamwise velocity fluctuations) is reported in Figure 11 and compared to the stationary wall condition. The latter exhibits a symmetrical distribution around $\gamma = 0$.

The conditions for the oscillating wall are examined at six values of the phase: $\phi = \pi/4, \pi/2, 3\pi/4, 5\pi/4, 3\pi/2, 7\pi/4$. Structures exhibit excess in tilt angle consistent with the oscillation direction at typical values significantly larger than that observed with the correlation analysis. Yet, a tilt of 10 to 20 degrees is consistent with the instantaneous visualisations. Peaks in the histograms are also observed consistently during the two opposite phases of the oscillation cycle, with positive and negative values of γ accordingly. The overall effect is that the histograms representing the occurrence of structure tilt becomes asymmetric and features a hump corresponding to the sidewise wall motion. When the same analysis is performed considering the joint condition of low-speed and ejection, the data scatter increases, and the correlation of tilt occurrence with the phase of oscillation becomes less evident (Figure 5.13). This may also be interpreted as ejections mostly corresponding to the head regions, which have already lifted up in the range $y^+ > 50$, and as such, they are less affected by the wall oscillatory motion. The latter should, however, not lead to the conclusion of ejection motions not being altered by wall oscillation. In fact, they are overall significantly reduced in number and intensity as a result of the shorter extent of such regions caused by the smaller number of hairpins being autogenerated.

Figure 5.14 shows the distribution of the pitch angle α for the detected ejection events. The differences between stationary and oscillating wall here are marginal. The distribution of γ , instead, yields a significantly wider spread for OW, indicating a higher probability for larger tilt states compared to the stationary wall. Considering the spanwise motion of the wall with an amplitude of 1 cm and frequency of 15 Hz, the maximum spanwise wall velocity can be approximated to 1m/s. The mean streamwise velocity in the tomographic domain is close to 2 m/s. The corresponding inclination that is expected to be in the region is close to 25° , which can be observed in the increased probabilities of γ in Figure 5.14b. The latter estimate based on kinematic properties falls near the previous estimate of γ_0 based on oscillation amplitude and streak length. It can be concluded that the wall oscillations act by tilting the turbulent structures that contribute to the large Reynolds stresses in the near-wall region. The latter results in the suppression of the near-wall cycle of hairpin autogeneration, ultimately leading to reductions in the local skin-friction drag.

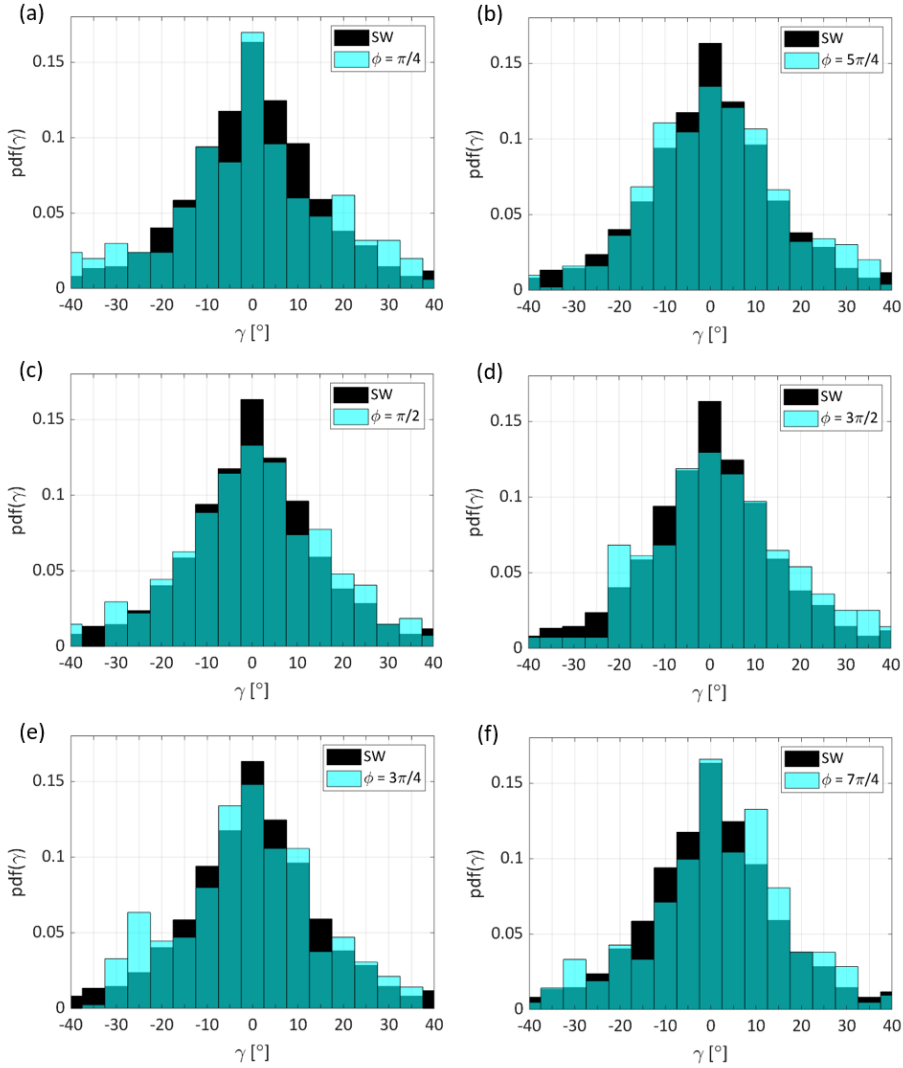


Figure 5.13: Probability distribution of sidewise tilt (γ) from detected ejections ($F_d^{u'v'} < -1$ AND $F_d^{u'} < 0$) at six phases of wall oscillation (a) $\phi = \pi/4$, (b) $\phi = 5\pi/4$, (c) $\phi = \pi/2$, (d) $\phi = 3\pi/2$, (e) $\phi = 3\pi/4$ and (f) $\phi = 7\pi/4$.

5.3.3. PROPERTIES, PHASE STATISTICS AND CONCEPTUAL MODEL

With the above data, the statistical occurrence and properties of streaks and ejections will be presented, with a comparison between the oscillating and stationary wall. Furthermore, the phase-dependent behaviour is accounted for. The

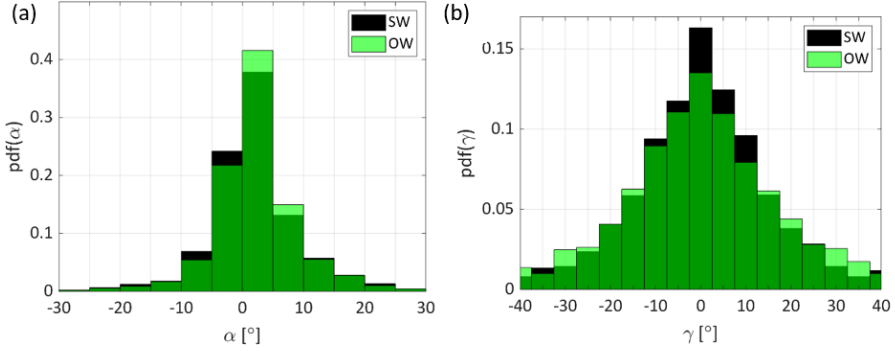


Figure 5.14: Comparison of the probability distribution function of α (a) and γ (b) for the stationary and oscillating wall cases of the detected ejection features.

5

section closes with a visual description of a conceptual model that expands on that previously presented by the authors [Kempaiah et al. \(2020\)](#), including some hypotheses on phase dependence.

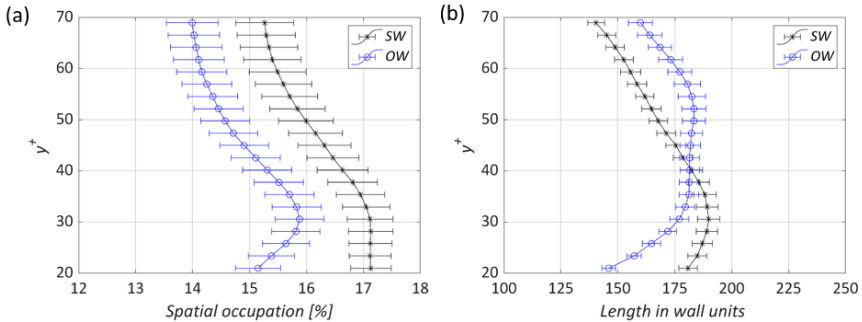


Figure 5.15: Distribution of spatial occupation (a) and streamwise length (b) of the detected streaks in the measurement domain from the implementation of feature detection algorithm in each $x-z$ plane corresponding to the wall-normal location.

Figure 5.15 depicts the spatial occupation and streamwise length of the streaks identified by feature detection. The analysis is conducted at several heights to infer their occurrence across the boundary layer ($x-z$ plane, refer to Figure 5.5). The analysis of spatial occupation of the streaks identified from the detection function ($F_d^{u'} < -1$) yields a presence of 17% for the stationary wall at a height up to $y^+ = 35$. The same structures have a significantly lower occurrence, peaking

at $y^+ = 30$ with 16% and generally remaining below the stationary wall case of approximately 10%. In this analysis, the results of the OW have been phase averaged as the phase dependence is small and not discernible through the feature detection algorithm. The length of the streaks is 10% to 20% shorter for the oscillated wall in the near wall region with a crossover at $y^+ = 40$, after which an inversion in length occurs, i.e. the streaks increase in length for the oscillated wall to an extent of 10%. This increase in length of the streaks above 40 wall units suggests that far from the wall, the streaky structure becomes more stable. This is ascribed to the reduced activity of ejection events. The latter hypothesis is consistent with the intensity of the u' fluctuations being lower in the case of the oscillating wall, as reported earlier (refer to Figure 5.3(b)).

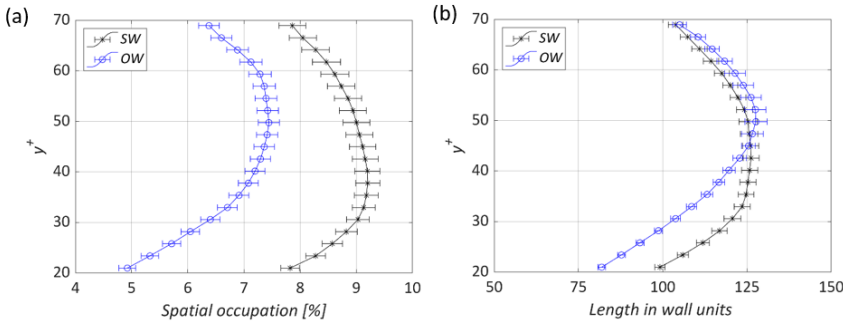


Figure 5.16: Distribution of spatial occupation (a) and streamwise length (b) of the detected ejections in the measurement domain from the implementation of feature detection algorithm in each x - z plane corresponding to the wall-normal location.

The ejection events reported in Figure 5.16 show a more marked difference between the stationary and oscillating wall. This supports the observation that the wall oscillations significantly weaken vertical velocity fluctuations, in turn attenuating sweeps and skin-friction. The spatial occupation of ejections is reduced from 20% to 40% over the examined domain. The streamwise length of these events exhibits a behaviour similar to that of the streaks, with a 10% to 20% shorter length up to 45 wall units. Above this height, an inversion is taking place, but the difference is not discernible. The ejection events in the region above 45 wall units have the same length scales, but the spatial occupation is reduced along with the intensity of these events, which can be observed in Figure 5.16b. For completeness, the phase dependence of these structures, i.e., the low-speed streaks and ejections, are examined, and results are reported in Table 5.2.

Table 5.2: Length and number of events for streaks and ejections from 3D feature detection.

Case		Streaks		Ejections	
		Length [wall units ⁺]	Number of Events [per field]	Length [wall units ⁺]	Number of Events [per field]
SW		279±7	7.3	194±4	11.2
OW	$\phi = 0, \pi$	273±12	7.0	179±6	10.3
	$\phi = \pi/4, 5\pi/4$	255±8	6.9	174±4	10.3
	$\phi = \pi/2, 3\pi/2$	258±11	7.4	165±6	11.0
	$\phi = 3\pi/4, 7\pi/4$	258±10	7.2	171±6	10.8

The results of the 3D algorithm (Table 5.2) show that the length of the streaks is the least when the position of the wall corresponds to $\phi = \pi/4, 5\pi/4$ with reductions in length of 10%, whereas the average number of detected events remains the same. The length of the streaks moves close to that of the stationary wall when $\phi = 0, \pi$. The same trend is observed for the ejection events, with reductions in the length by 15% in the $\phi = \pi/2, 3\pi/2$. The phase dependence in the coherent structures analysed is observable, although with a delay due to the wall-normal location of the measurement volume. The process of turbulent kinetic energy production is linked directly to the ejections ($u'v'$) and indirectly to the low-speed streaks (u'). The low-speed streaks are known to oscillate and break up, leading to ejection events. As a result, a primary hairpin vortex is created, which is followed by the formation of a hairpin packet through the auto-generation process.

The dynamical behaviour recently hypothesised by the authors [Kempaiah et al. \(2020\)](#) hinges on the combined condition of pitched structures subject to a sidewise wall motion. This condition ultimately results in a sidewise tilt (γ) of the elongated structure and its rapid distortion as a result of the varying lateral friction induced by the moving wall. It is argued that not all phases of the oscillatory motion are effective in producing such distortion, the stages of maximum lateral velocity being most responsible for this mechanism. Instead, during the phase of motion inversion, when the wall can be considered stationary for a given time interval (approximately one/quarter of the total oscillation period), structure distortion remains minimal. The duration of such phase at $T^+ = 100$ is approximately 25 viscous time units and is comparable to the time reported for hairpin auto-generation ($t_{auto}^+ = 30$). Therefore, the motion inversion phase is characterised by an increase in the number of hairpins. In contrast, the rapid motion of the wall during the phase of maximum lateral velocity inhibits the auto-

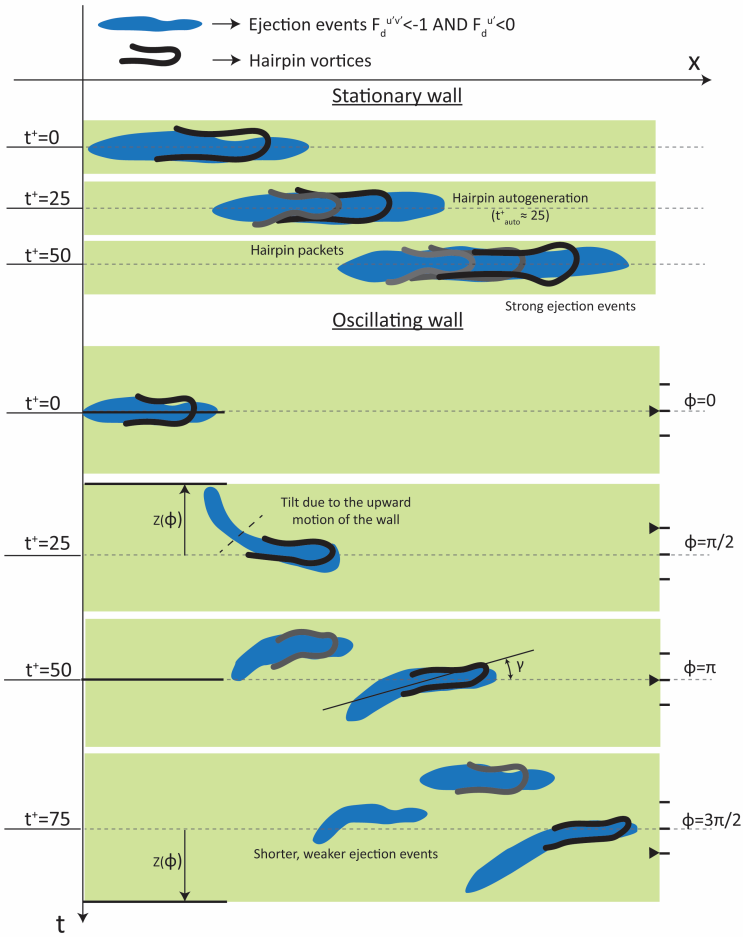


Figure 5.17: Illustration of the distortion mechanism responsible for inhibiting hairpin auto-generation based on wall oscillation. The structure side-tilt results in shorter and less coherent ejections. The process is symmetrical around $\phi = \pi$.

generation process, due to the displacements of the streaks from the streamwise vortices, under the effect of the Stokes layer (Figure 5.17).

From the obtained results, it is clear that the spanwise tilt of the identified structures is linked to the motion of the wall. This tilt imparted in the structures leads to a reduction in the length and spatial occupation of the ejection events (refer to Figure 5.6 for quantitative visualisation of the detected structures for SW and OW). The reduction in the intensity, length and spatial occupation of the mixing events leads to a benefit in skin friction and a reduction in turbulent kinetic energy production. The above discussion is summarised and exemplified

in the illustration, where the process of hairpin autogeneration in a turbulent boundary layer with a stationary wall is compared to that of an oscillating wall. For the latter, the salient features characterising the different stages of the oscillation process are schematically illustrated.

5.4. CONCLUSION

The low-speed streaks and ejection events in the near-wall region of a turbulent boundary layer at $Re_\theta = 1000$ subjected to spanwise wall oscillation have been investigated. Experimental data collected with tomographic-PIV is examined to infer the statistical properties of turbulence. Spatial auto-correlation is compared with a feature-based technique to highlight the difference w.r.t the coherent structures. The former returns limited information on the structure's properties and arrangement, which is due to wide spatio-temporal variations in their occurrence. Feature detection isolates the individual features of interest and is based on the instantaneous distribution of the Reynolds stress, in particular streamwise and wall-normal fluctuations. The spatial occupation and length of ejections are significantly reduced in the wall oscillation regime, 40% and 20%, respectively. Overall, the feature-based analysis appears to be more robust in these conditions and less affected by data dispersion during averaging.

The dependence of the turbulent motions on the phase of the wall motion has been further investigated. A clear phase dependence is observed between the sidewise tilt and the wall motion for the identified ejection events. Furthermore, a significantly higher probability for events with larger tilt is observed as a result of wall oscillation. The maximum observed tilt angle of approximately 20° is consistent with proposed estimates based on geometric or kinematic criteria. The streamwise length and spatial occurrence of streaks and ejections, instead, do not exhibit a specific correlation with the phase of the oscillation. The overall behaviour and properties of streaks and ejections observed here are consistent with the conceptual model whereby wall oscillations successfully weaken the early formation of hairpins in the near-wall cycle of the turbulent boundary layer by inhibiting hairpin auto-generation and, in turn, reducing the occurrence of energetic lift-up events.

6

PLASMA BASED SURROGATE OF THE OSCILLATING WALL

*You cannot cross the sea merely
by standing and staring at the water*

Rabindranath Tagore

To transition from the mechanical system of wall oscillation, which has challenges like high inertial forces that limit the scalability and implementation of wall oscillations. The current chapter investigates the possibility of surrogating the wall oscillations with plasma actuators. Various unsteady AC-DBD plasma actuator configurations, defined by the electrode dimensions, input voltage signal and actuation frequency, have been manufactured and investigated in quiescent conditions with PIV. The topology of the unsteady jets is characterised to establish a suitable design that closely surrogates the conditions achieved in Chapter 4 and Kempaiah et al. (2020).

Subsequently, the actuator is immersed in a turbulent boundary layer, where the TBL's effect on the plasma's flow topology is investigated along with the impact of the plasma forcing on the TBL dynamics. In addition, the learnings from the unsteady actuator motivated the development and investigation of a steady spatially varying plasma forcing, which overcomes the challenges of the unsteady forcing.

Parts of this chapter have been published [Scarano et al. \(2022\)](#).

6.1. INTRODUCTION

The use of plasma actuators for boundary layer control has received considerable interest in the last 20 years. Plasma actuators have been used for a diverse set of applications like pitch and roll control (He et al., 2009), separation control (Yu et al., 2023) and skin-friction reduction (described in Section 2.2.3). Plasma actuators are active flow control devices that produce a discharge-based body force in the vicinity of the wall. The body force of an AC-DBD plasma actuator is imparted to the surrounding air, mostly tangent to the wall along the anode-cathode direction. Early experimental characterisation of the body force field is due to Kotsonis et al. (2011), followed by a field review (Kotsonis, 2015). A complete overview of the literature on plasma actuators for skin-friction reduction is made in Section 2.2.3.

The use of AC-DBD to manipulate skin friction has been practised numerous times. Furthermore, reproducing experiments among different laboratories has proven challenging, and the debate is still open on the working principles of plasma actuators for skin friction control. Some works in literature have attempted to surrogate the wall oscillations. For example, Jukes et al. (2006) alternately activated two opposing sets of electrodes of the plasma actuators to produce the desired near-wall oscillating conditions. The results reported that a reduction of skin-friction by 45% was obtained downstream of the actuator. However, the topology of the forcing consisted of streamwise vortices in the inner region of the boundary layer and is in stark contrast to the Stokes layer produced by the oscillating wall. Therefore, the drag reductions can be ascribed to a different mechanism.

Similarly, many efforts reported in the literature, like the travelling wave (Whalley and Choi, 2014) and pulsed DC plasma actuation (Su et al., 2021; Thomas et al., 2019; Zong et al., 2022), rely on different underlying principles that are associated with the skin-friction behaviour. Whalley and Choi (2014) investigated an array of plasma actuators in two different forcing configurations: uni-direction travelling wave and bi-directional forcing, similar to Jukes et al. (2006). In the uni-directional case, the actuator creates a single streamwise vortex sequence, which moves as a single vortex engulfing the neighbouring vortices from the previous phases. As in Jukes et al. (2006), the bi-directional forcing leads to a complex interaction of co and counter-rotating vortices. Reductions in streamwise velocity by 10% and 20% are observed at a $y^+ = 20$, but drag reductions have not been reported. Hehner et al. (2019) used the burst mode of actuation to mimic the spanwise wall oscillation, using four groups of electrodes and three independently operated high-voltage power supplies. Furthermore, Hehner et al. (2020) successfully used the beat frequency concept to produce a spanwise oscillating flow in close agreement with the topology of wall oscillations. The dif-

ference is the absence of the tangential velocity at the wall. The configurations, forcing conditions and interpretation of plasma actuators for skin-friction reduction reported are diverse, as reported in Table 2.3 in Section 2.2.3.

Therefore, the current work attempts to produce an unsteady AC-DBD actuator with the desired near-wall forcing to surrogate the effect of the oscillating wall. The main questions that will be investigated through this work are

- At what spatial layout and operating conditions does the AC-DBD array produce similar flow fields as the oscillating wall?
- What are the differences in the flow topology produced by the actuator in quiescent conditions and when immersed in a turbulent boundary layer?
- Is skin-friction reduction obtained through the designed surrogate?

Multiple actuator configurations corresponding to the electrode lengths, dielectric thickness, and input AC signal have been analysed in quiescent conditions and the presence of an incoming turbulent boundary layer using PIV. The chapter concludes with the design and characterisation of a steady AC-DBD actuator that is expected to overcome the challenges of the unsteady mode of operation.

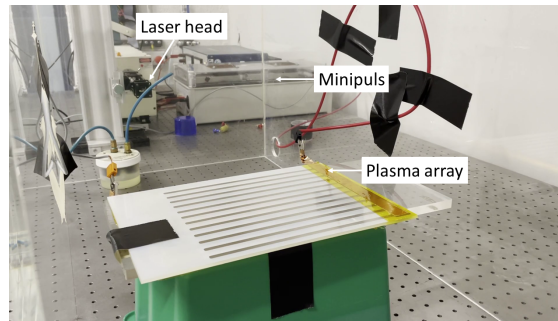
6.2. EXPERIMENTAL SETUP AND PROCEDURE

Experiments were performed following two scopes: at first, the plasma actuator in several configurations and modes of operation was investigated in a quiescent environment. Then, further to that, the plasma actuator is installed in a low-speed wind tunnel, where a turbulent boundary layer develops.

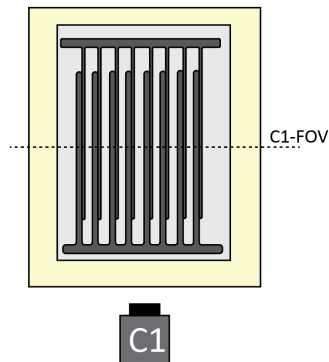
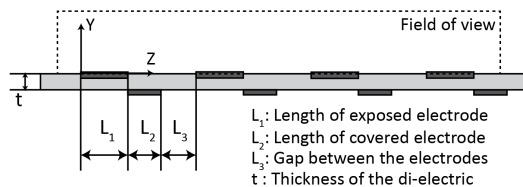
6.2.1. CHARACTERISATION IN QUIESCENT CONDITIONS

The characterisation of the unsteady AC-DBD plasma actuator was performed in a transparent closed chamber of size $40 \times 40 \times 80 \text{ cm}^3$. The actuator is installed on a platform of height 10 cm from the bottom floor (see Figure 6.1). High-speed time-resolved planar PIV was employed to characterise the flow in the vicinity of the plasma actuator. The adopted system enables the spatial and temporal resolution required to analyse the transient behaviour of the thin wall jet induced by the actuator array. The planar PIV system consisted of a high-speed CMOS camera (Photron FastCAM SA1) with a lens of focal length 105 mm, providing a field of view of $45 \times 10 \text{ mm}^2$. Refer to Table 6.1 for the details of the PIV. For the light source Quantronix Darwin Duo Nd:YLF laser was used, and a light sheet of thickness 2 mm was produced using a combination of cylindrical and spherical

lenses. Atomised droplets of olive oil were used as seeding particles as they were not affected by the electrical field near the actuator.



(a)



(b)

Figure 6.1: Photograph (a) and schematic (b) of the experimental setup in the quiescent environment. Acquisition planes of the PIV measurements and camera placements are also indicated (not to scale).

AC-DBD actuators with varying exposed (L_1), covered (L_2) electrode lengths, spacing (L_3) and sheet thickness (t) were analysed (refer to Figure 6.1). The actuators were produced using an inkjet printer loaded with micron-sized silver

ink particles. The exposed and covered electrodes were printed on two separate polyethylene terephthalate (PET) foil sandwiched between a sheet of Perspex of a varying thickness (t) which acts as the di-electric. With the aim to report the best combination of these parameters that act as a surrogate to the oscillating wall conditions reported in [Kempaiah et al. \(2020\)](#). The variables that determine the actuator configuration are

- Geometric parameter: L_1, L_2, L_3 and t
- Input signal: Voltage (V), frequency (f) and waveform

Table 6.1: Description of parameters for the PIV measurements in the quiescent conditions.

Seeding Particles	Olive oil droplets ($d_p = 1\mu m$)
Illumination	Quantronix Darwin Duo Nd:YLF ($2 \times 25mJ$ at 1KHz)
Recording device	Photron FastCAM SA1 (CMOS, 1204×1204 pixels, pitch of $20 \mu m$)
Recording method	Double frame/Single exposure
Number of camera	1 (C1 in Figure 6.1)
Field of view	$45 \times 10 mm^2$
Recording lens and aperture	105 mm, $f_{\#}=8$
Image resolution	1024×400
Optical magnification	21.40 px/mm
Recording frequency	2kHz
Pulse delay	$120 \mu s$
Number of recordings	7000
Interrogation window and vector pitch	12×12 px, 75% overlap 0.2 mm

Table 6.2: Configurations of the arrays used for determining the di-electric thickness (t) and the configuration (L_1, L_2, L_3), Phase 1.

Di-electric thickness (t, mm)	Configuration ($L_1-L_2-L_3$, mm)	
1.5	1-3-1	1-3-2
	2-4-1	2-4-2
2.0	2-3-4	2-3-8
3.0	5-3-8	6-3-6

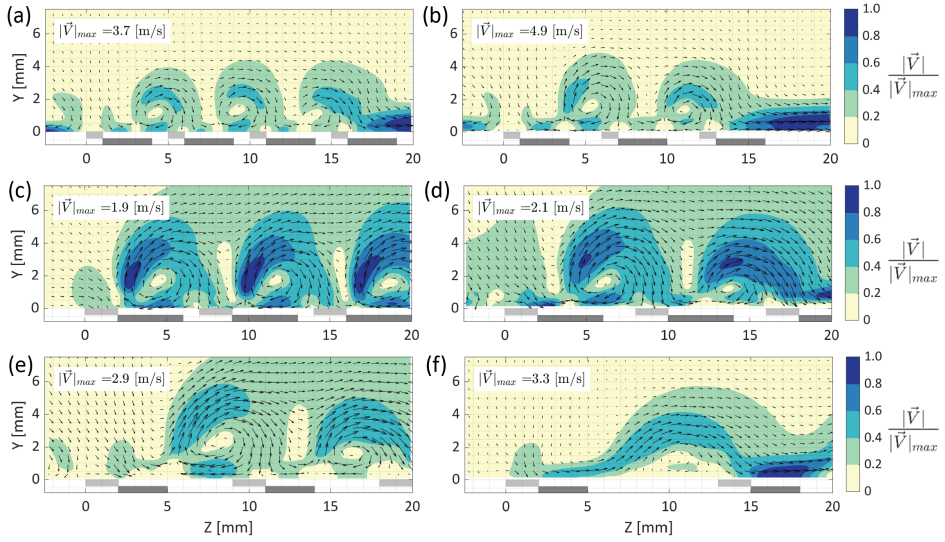


Figure 6.2: Velocity fields obtained from the continuous operation (DC100) of the actuator configurations 1-3-1 (a), 1-3-2 (b), 2-4-1 (c), 2-4-2 (d), 2-3-4 (e) and 2-3-8 (f) corresponding to di-electric material thickness of 1.5 (a-d) and 2.0 mm (e-f) in Table 6.3; Velocity magnitude contour is scaled with the maximum velocity in the field which is indicated at the top left of the plot, the quiver arrows shows the flow direction.

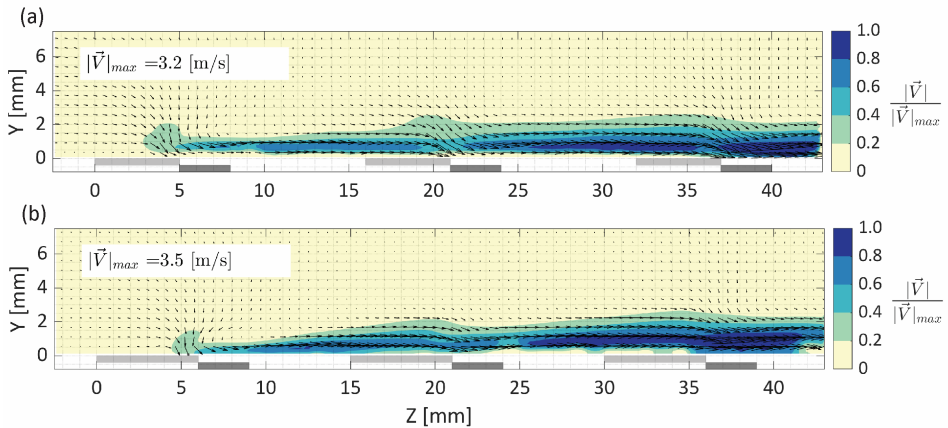


Figure 6.3: Velocity fields obtained from the continuous operation (DC100) of the actuator configurations 5-3-8 (a) and 6-3-6 (b) corresponding to di-electric material thickness of 3.0 mm in Table 6.3; Velocity magnitude contour is scaled with the maximum velocity in the field which is indicated at the top left of the plot, the quiver arrows shows the flow direction.

To assess the di-electric's thickness and the actuators' suitable lengths. Perspex sheets of thickness 1.5, 2.0 and 3.0 mm and rectangular dimensions of 200 mm \times 50 mm were used for a varying configuration of the actuator reported in Table 6.2. The input signal for the arrays was provided by a GBS Elektronik Minipuls 4 high-voltage amplifier controlled by LabView at 100% duty-cycle at 30kV to analyse the continuous operation.

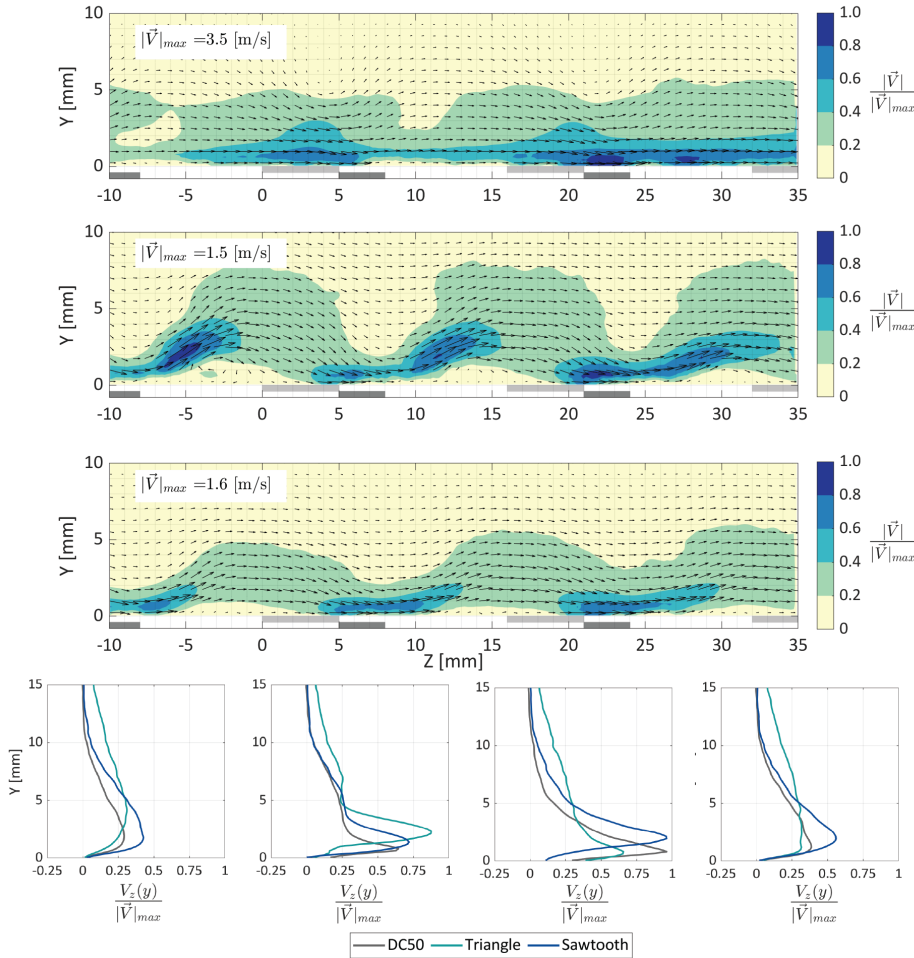


Figure 6.4: Instantaneous velocity fields corresponding different waveform like DC50 square wave (a), triangle (b), sawtooth (c) at $t = T/4$ and comparison of the scaled velocity profiles at $t=0$ (d), $T/4$ (e), $T/2$ (f) and $3T/4$ (g).

From the analysis, Perspex sheets of thickness 3 mm were chosen to be the

di-electric material due to their extended performance during longer operating cycles. Thinner di-electrics resulted in burnout and overheating of the array over multiple operation cycles. The flow fields obtained from the actuators described in Table 6.2 showed that most arrays, i.e. (1-3-1, 1-3-2, 2-4-1, 2-4-2, 2-3-4) exhibited flow reversal and lift-up of the oncoming jet due to the small exposed electrode lengths and gaps (refer Figure 6.2). These features are deemed undesirable due to their ability to enhance the mixing in the near-wall boundary layer flow. Following this, the dimensions of the electrodes were increased, and the subsequent arrays, i.e., 5-3-8 and 6-3-6 with a di-electric thickness of 3 mm, resulted in a near wall jet without any lift (refer Figure 6.3). Based on the results, a choice was made for a suitable array with exposed and covered electrode lengths of $L_1=5$ mm and $L_2 = 3$ mm, the spacing L_3 as 8 mm.

With the array's configuration, finalised new actuators were manufactured with Perspex sheets of thickness 3 mm and size 297 mm \times 210 mm. Larger-sized arrays could not be achieved due to the manufacturing capabilities in the laboratory. The remaining parameter that controls the forcing is the input signal. Due to the unsteady nature of the forcing, different input signals were analysed. The chosen input waveforms, i.e., the DC50 wave corresponding to 28kHz, were provided by Minipuls 4. Due to the inability of the Minipuls 4 to modulate the input waveform, an AC voltage Amplifier was used to produce sawtooth and triangular waveforms. Figure 6.4 reports the scaled velocity fields from the three waveforms at $t = T/4$ during the actuation cycle. It can be observed from the plots and the corresponding multimedia file that the plasma force produced by the Minipuls at DC 50 is confined to the near-wall region, and no lift-up is observed. This is expected to play an essential role in the ability of the actuator to surrogate the motion of the oscillating wall. However, the instantaneous spanwise velocity distribution in Figure 6.4a indicates that owing to the inhomogeneity and the unsteady nature of the actuation, the formation of the starting vortex cannot be avoided. Therefore, the drag reduction experiments will employ an actuator array of size 297 mm \times 210 mm with a configuration of 5-3-8 and DC50 forcing from the Minipuls.

6.2.2. BOUNDARY LAYER ENVIRONMENT

The chosen actuator was placed in the W-tunnel in the faculty of Aerospace Engineering at TU Delft, to study the effect of the plasma forcing on the dynamics of the TBL. The size of the actuator corresponding to TBL thickness is $5 \times 3.5(\delta_{99})$ and the viscous scales is $2970 \times 2100(l^+)$. The experimental setup for the configuration is shown in Figure 6.5. Low-speed Planar (P1 in Figure 6.5) and Stereo-PIV (S1, S2 in Figure 6.5) measurements were performed using LaVision sCMOS cameras equipped with 105 mm focal length Nikon objectives. The measurements were performed downstream of the plasma actuator. The corresponding PIV parameters for the experiment are shown in Table 6.3.

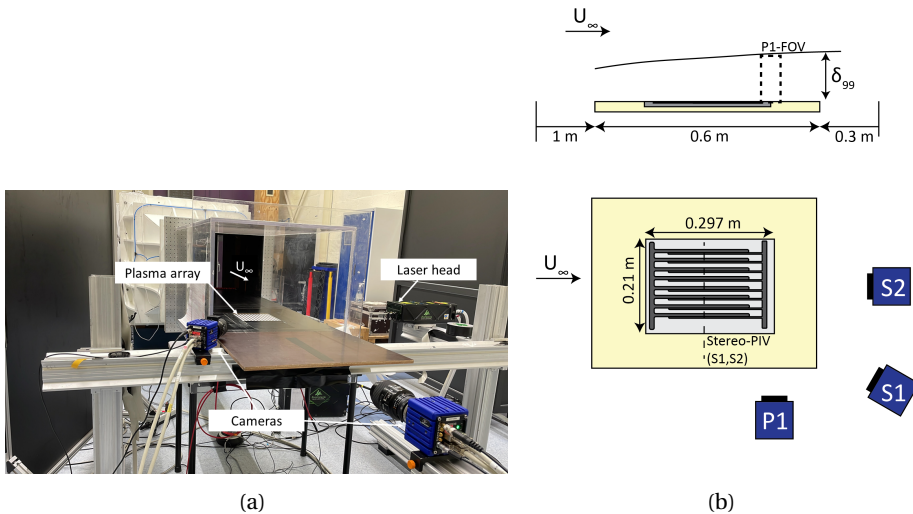


Figure 6.5: Schematic of the experimental setup for the measurements in the W-tunnel . Acquisition planes of the PIV measurements and camera placements are also indicated (not to scale).

The mean boundary layer velocity profile and the Reynolds stresses were obtained by ensemble averaging the PIV velocity data and represented in wall units. The velocity profile is compared with DNS data computed at $Re_\theta = 1000$ (Schlat-ter and Örlü, 2010). The planar PIV data exhibit good agreement in the inner region with a well-resolved viscous sublayer (see Figure 6.6(a)). The Reynolds stresses obtained are in good agreement with the DNS data with peak streamwise fluctuations $\langle u' u' \rangle^+$ lower than DNS by 2%, refer to Figure 6.6(b). The deviations are observed in the outer regions of the boundary layer, where the intensity of the measured fluctuations persists at $y^+ \sim 500$, whereas the DNS results collapse

to zero already at $y^+ \sim 400$ due to the difference in Re_τ of the data.

Table 6.3: Description of parameters for the PIV measurements in the wind tunnel conditions.

	Planar-PIV	Stereo-PIV
Seeding particles	Fog droplets ($d_p = 1\mu\text{m}$)	
Illumination	Nd:YAG, 2×200 mJ, 15 Hz	
Recording device	sCMOS (2560×2160 pixels, 16 bits, $6.5\mu\text{m}$ pixel pitch)	
Recording method	Double frame/Single exposure	
Number of cameras	1 (P1)	2 (S1, S2)
Field of View	$40 \times 80\text{ mm}^2$	$80 \times 15\text{ mm}^2$
Recording lense and aperture	105 mm, $f_\# = 8.0$	
Imaging resolution	30 px/mm	20 px/mm
Recording frequency	13.5 Hz	13.5 Hz
Pulse delay	$180\mu\text{s}$	$150\mu\text{s}$
Number of recordings	2400	500
Interrogation window and vector pitch	32×32 75% overlap	16×16 75% overlap

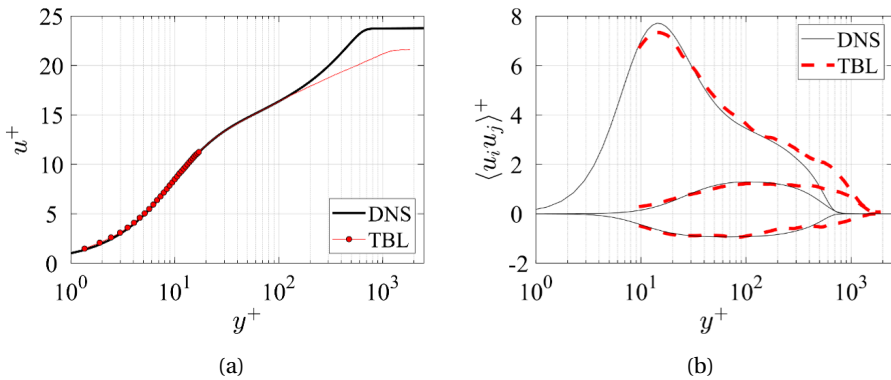


Figure 6.6: Measured mean streamwise velocity profile (a) and Reynolds stresses (b) with inner-layer scaling and comparison to DNS data from literature ($Re_\theta = 1000$).

Table 6.4: Turbulent boundary layer properties.

Re_θ	Re_τ	U_∞ [m/s]	δ_{99} [mm]	δ^* [mm]	θ [mm]	u_τ [m/s]	l^+ [mm]	H
980	570	3.0	59	6.7	4.9	0.145	0.10	1.36

6.3. RESULTS AND DISCUSSION

6.3.1. PLASMA FIELD COMPARISON

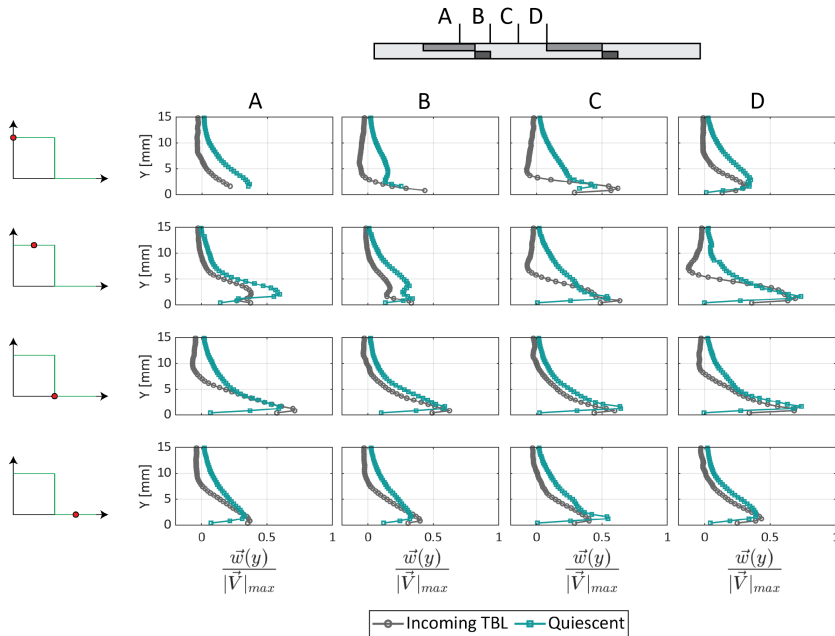


Figure 6.7: Comparison of the near-wall velocity profiles produced by the plasma array in quiescent and in the presence of TBL.

The topology of the plasma produced by the actuator in the presence of the TBL needs to be compared with that observed in the quiescent environment. Figure 6.7 reports the phase-averaged velocity profiles for the chosen actuator at four spatial locations and four-time instances. Interestingly, the spatial evolution of the velocity profile at the near wall region is similar for both external conditions. On the other hand, away from the wall ($y > 5\text{mm}$), the spanwise velocity is zero for the plasma forcing in the presence of the TBL, indicating that the streamwise velocity prevents the spanwise convection that occurs in the quiescent conditions. The reduction in spanwise momentum in the region away from the wall

due to the TBL implies that the plasma forcing is better confined to the near-wall region, due to the streamwise convection.

When comparing the topology of the flow produced by the actuator and the oscillating wall, the flow velocity is averaged in the spanwise direction and is compared with the oscillating wall at $t = 0, T/4, T/2, 3T/4$ (refer Figure 6.8). The velocity produced by the plasma actuator peaks at 2.5 m/s ($W(y)_{max}$), which is larger than that of the oscillating wall at $T_{osc}^+ = 95$ and $A_{osc}^+ = 100$, which peaks at 1 m/s at the wall. However, two main differences can be observed: first, the velocity at the wall remains null; secondly, the sideways velocity features a wall jet with a peak between 1 and 3 mm off the wall.

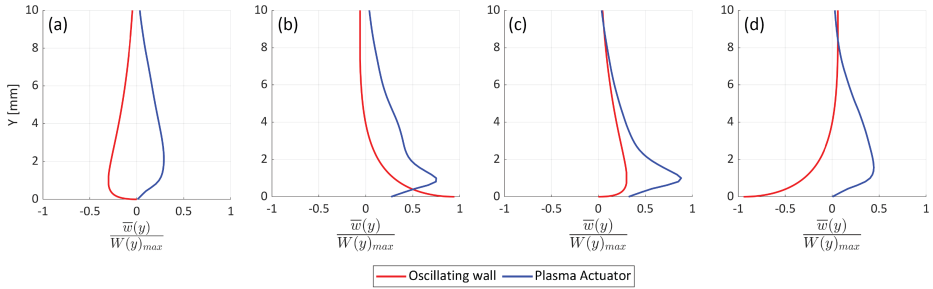


Figure 6.8: Modelled velocity profile during mechanical wall oscillation (red) and the velocity measured during plasma actuation (blue) at $t = 0$ (a), $T/4$ (b), $T/2$ (c) and $3T/4$ (d).

6.3.2. EFFECT OF PLASMA ACTUATOR ON TBL

The effect of the plasma actuator on the velocity distribution in the TBL is shown in Figure 6.9, where the deficit in streamwise velocity for three duty cycles is shown. From the contour plot, it can be observed that the spanwise inhomogeneity amplifies with the increase in duty cycle from 25 to 75%. Downstream of the plasma array, however, the spanwise inhomogeneity is not present, as seen in the velocity profile near the wall in Figure 6.10.

The velocity profile of the TBL subjected to the plasma forcing results in a significant deficit in momentum in the log region. A detailed analysis near the wall reveals that the wall shear force is not decreased but increases visibly. The latter effect is ascribed to the formation of additional flow structures (streamwise vortices) resulting from the unsteady and inhomogeneous actuation. Therefore, the role of unsteady streamwise vortices on skin-friction control requires further understanding, possible to guide towards approaches that avoid their occurrence. The latter cannot be overcome due to the physical principle of plasma body forces being formed by a discrete electrode. Some potential is seen in adopt-

ing the steady actuation procedure, which still mimics the effects observed with the mechanical oscillation

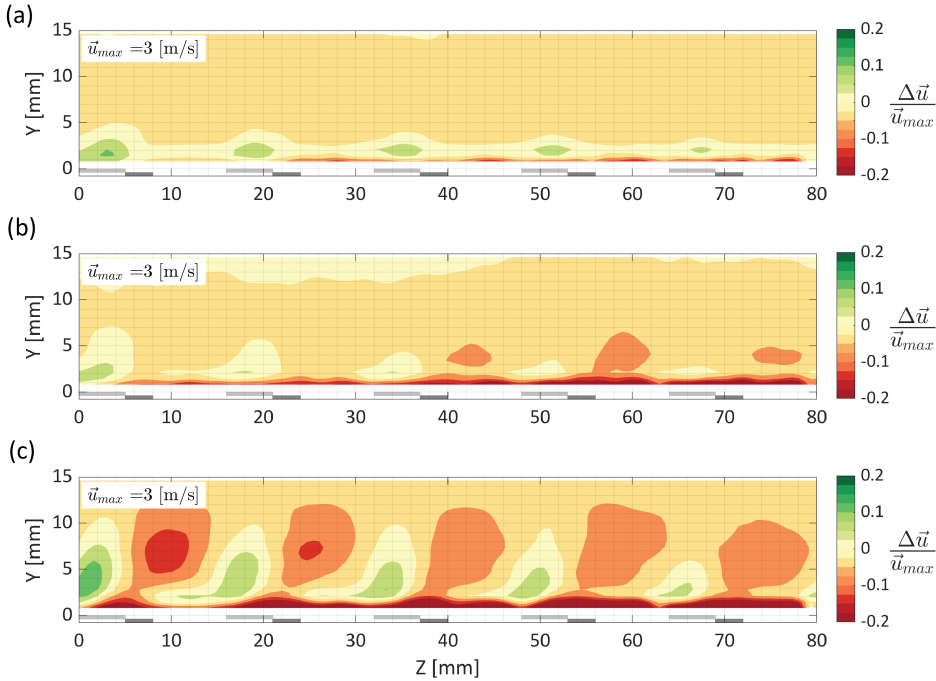


Figure 6.9: Contour plot depicting the deficit in the streamwise velocity between the plasma forcing at a duty cycle of 25%(a) 50%(b) and 75%(c) with the unforced conditions over the centreline of the actuator as indicated in Figure 6.5.

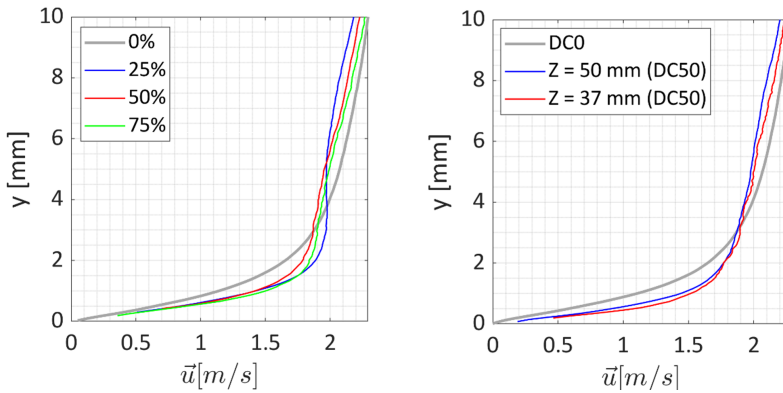


Figure 6.10: Velocity profiles of the TBL subjected to input signal of DC0, DC25, DC50 and DC75 at $Z = 50$ mm (a) and the effect of the spanwise location for DC0 and DC50 at $Z = 37$ and 50 mm (b), the data is obtained downstream of the plasma array as indicated in Figure 6.5.

6.4. STEADY ACTUATOR AS A SURROGATE

From the observation of the velocity profile and the trends in the skin-friction, the unsteady and inhomogeneous nature of the forcing leads to enhanced mixing and results in a larger deficit of momentum in the turbulent boundary layer. Therefore, the implementation of the unsteady uni-directional AC-DBD plasma actuator, which appears to surrogate the spanwise forcing of the wall oscillation, fails to produce skin-friction reductions. To overcome this challenge, a steady spatially varying standing wave forcing similar to the discussions in Section 2.2.2 will be designed and characterised in this section.

Viotti et al. (2009) investigated the effect of the distribution of spanwise velocity that alternates in the streamwise direction. The spatial forcing of a standing wave was observed to be more efficient when compared to the temporal forcing at the same conditions. Drag reductions of 52% were obtained for $A^+ = 20$ and $\lambda^+ = 1250$. For all amplitudes, the forcing wavelength that yields the maximum DR has been found to correspond to the optimal period if the oscillating wall is converted in length through the convection velocity $U_c^+ = 10$.

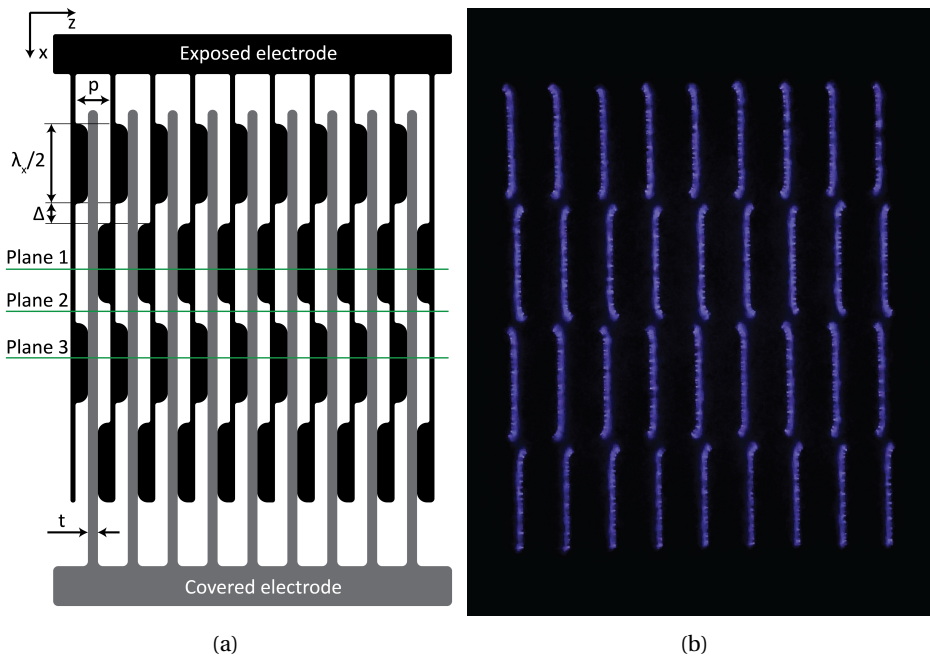


Figure 6.11: Steady AC-DBD actuator configuration corresponding to Array 002 in table 6.5, and Planar-PIV measurement planes indicated as Plane 1,2,3.

Using the conditions of the TBL described in Chapter 4, the actuators de-

signed are described in Table 6.5. The dimensions were arrived at based on the limitations of the current setup where the maximum size of the actuator is limited by the printer which is the size of an A4 sheet.

Table 6.5: Configurations of the steady AC-DBD actuators developed.

Array Number	Wavelength		No of cycles	Pitch (p, cm)	Thickness of covered electrode (t, cm)	Gap (Δ , cm)
	λ [cm]	λ^+				
001	4.0	400	4	2.0	1.0	1.5
002	9.5	950	2			1.5
003	2.0	200	8			0.25

The actuators were tested in the quiescent conditions as described earlier in Section 6.2. The design of the actuator and the corresponding plasma field captured by the camera qualitatively are shown in Figure 6.11. In the current form, the body force alternates direction, and the produced forcing was characterised using planar PIV at three locations, as indicated in Figure 6.11.

- Plane 1: Forcing to the left over the centre of the electrode.
- Plane 2: In the gap between the two forcing regions.
- Plane 3: Forcing to the right over the centre of the electrode.

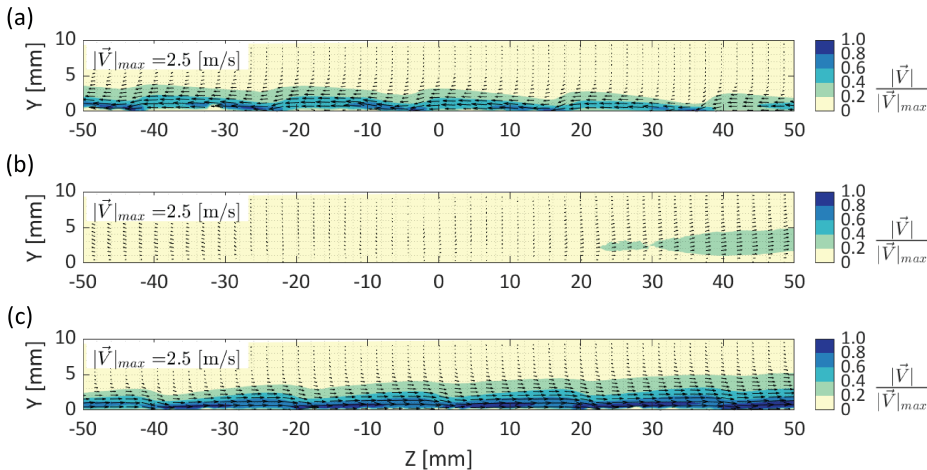


Figure 6.12: Mean velocity fields corresponding to Plane 1 (a), Plane 2 (b) and Plane 3 (c) corresponding to Array 002 with AC voltage at 40kV peak-peak and 12.5KHz.

The actuator in Figure 6.11, produces a steady jet that alternates in the streamwise direction. The velocity profile of the plasma jet due to the steady nature, peaks at $y = 2\text{mm}$. The velocity profile resembles the profile produced as a result of the Stokes 1st problem (which corresponds to the constant motion of the wall in the spanwise direction with constant velocity). Arrays 001 and 002 result in clean alternation in direction, whereas the forcing in the case of Array 003, which has a shorter wavelength leads to flow reversal and lift up due to the interaction in the opposite direction. However, the forcing observed in Array 001, 002 show good promise as possible method to achieve the standing wave forcing using plasma actuators.

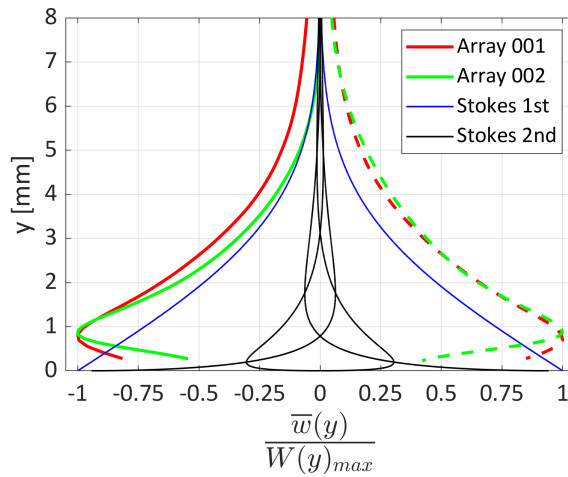


Figure 6.13: Spanwise averaged velocity profile for Array 001 and 002 at Plane 1 (solid) and 3 (dashed) corresponding to Figure 6.12, scaled by the maximum velocity of $W(y)_{max} = 2.5\text{m/s}$ and the corresponding profiles from the Stokes 1st and 2nd problem (Stokes, 1851)

6.5. CONCLUSION

The results discussed in this chapter indicate that using unsteady uni-directional forcing through plasma actuators poses challenges while surrogating wall oscillations. The resulting body force leads to a consistent increase in skin-friction and momentum deficit throughout the boundary layer. The two main features that appear to limit this actuation method are spatial discreteness and the unsteadiness of the forcing. The unsteadiness leads to the formation of starting vortex, which cannot be avoided and leads to complex non-linear interactions with the flow in the TBL. As a result, the near-wall dynamics are not affected

through the mechanism hypothesised for spanwise wall oscillations.

Therefore, the development of the steady actuator described in the latter part of the chapter, Section 6.4, indicates the potential to overcome the challenges of the earlier forcing configuration. Furthermore, the forcing corresponds well with Stoke's first problem with the peak velocity closer to the wall ($y = 0.8\text{mm}$) than the unsteady actuator ($y = 3.0\text{ mm}$), leading to better confinement of the jet near the wall. However, Further investigations are needed to understand the effect of this forcing on the skin-friction.

7

TBL CONTROL BY AN ARRAY OF ROTATING DISCS

Somewhere, something incredible is waiting to be known.

Carl Sagan

While the previous chapter focused on surrogating the wall oscillations with plasma actuators, the results indicated that the nature of the plasma body force has limitations due to the body force being above the wall compared to the wall motion afforded in spanwise wall oscillation.

This chapter investigates the concept of a flush-mounted array of rotating discs, which overcome the challenges of high inertial and vibrational forces experienced in spanwise wall oscillations. This work experimentally assesses the flow manipulation of this wall-based actuation method using planar and stereoscopic particle image velocimetry (PIV). Experiments were conducted in a developing turbulent boundary layer, at $Re_\tau \approx 910$, and with an optimized viscous-scaled sizing and layout of the discs following the direct numerical simulation (DNS) study of [Ricco and Hahn \(2013\)](#).

Parts of this chapter have been published in [Kempaiah et al. \(2022\)](#)

7.1. INTRODUCTION

An active flow control method for turbulent friction drag reduction, relying on transverse wall-oscillation at time scales matching the most energetic temporal scales of the near-wall turbulence ($t^+ \approx 100$), has been studied extensively for over 30 years (Leschziner, 2020). In the DNS study of Quadrio and Ricco (2004), a reduction in friction drag of up to 45% was reported, albeit this study was limited to a friction Reynolds number of $Re_\tau = 200$ (note that $Re_\tau \equiv \delta u_\tau / \nu$ or δ^+ is the ratio of the channel half-width or boundary layer thickness δ , to the viscous length scale ν / u_τ). In Chapter 4, experiments were conducted on a transverse oscillating wall and explored an oscillating time-scale down to $t^+ = 94$ at a Reynolds number of $Re_\tau = 570$; the results were in line with the earlier DNS studies of Quadrio and Ricco (2004). Since the working mechanism of this global actuation method relies on a motion that scales with the viscous time-scale, an experimental implementation of this actuation method is practically challenging when moving towards higher Reynolds numbers, primarily due to high inertial and vibrational forces required to sustain the high-frequency oscillation.

Recently, Marusic et al. (2021) postulated that a more effective drag reduction at high Reynolds number conditions can be achieved with wall-oscillation frequencies on the order of large, outer-scaled flow features. Still, the current work focuses on relatively low Reynolds number conditions and follows the control concept of Keefe and Keefe (1997). They proposed a wall-normal vorticity-forcing through an array of flush-mounted discs within the wall, each rotating at a constant angular velocity (top view in Figure 7.1c). That is, each disc belonging to a spanwise row in a streamwise–spanwise array, rotates with the same orientation but alternates from row-to-row. In this way, the convective flow encounters a degree of spanwise wall-oscillation. The wave motion is perpendicular to the flow and maximum in amplitude when considering the spanwise centre of a streamwise line of discs. Note that a practical implementation of this actuation method is relatively straightforward: it does not require any oscillatory, linear motion but is only based on rotational motion. This control concept was examined using DNS of channel flow by Ricco and Hahn (2013), who inferred maps of friction drag reduction as a function of the viscous-scaled disc diameter ($D^+ \equiv D u_\tau / \nu$) and edge velocity ($W^+ \equiv W / u_\tau$ with $W = 0.5D\Omega$, in which Ω is the angular rate-of-rotation); a maximum wall-drag reduction of 23% was found at a friction Reynolds number of $Re_\tau = 180$.

The current work explores the wall-based actuation method of turbulent boundary layer (TBL) flow at Reynolds numbers higher than the ones available in the literature and uses an experimental implementation of the technique. To the authors' knowledge, this is the first practical realization of this type of flow control method. A description of the hardware and the PIV-based velocity measure-

ments for assessment of the large-scale flow organization are covered next.

7.2. EXPERIMENTAL METHODOLOGY

7.2.1. WIND TUNNEL AND ARRAY OF ROTATING DISCS

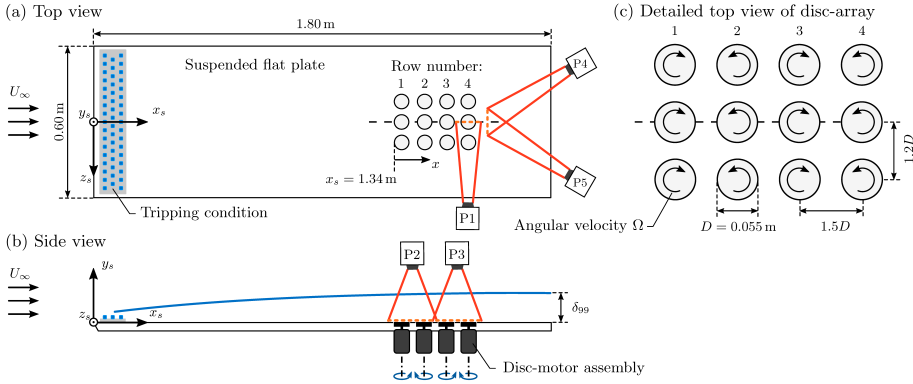


Figure 7.1: Schematic of the experimental TBL flow setup, with the array of rotating discs flush-mounted in a flat plate. Acquisition planes of PIV measurements and camera placements are also indicated (not to scale).

Experiments were conducted in an open-return low-speed wind tunnel at the Faculty of Aerospace Engineering of the Delft University of Technology. A boundary layer with a slight favorable pressure gradient was generated using a flat plate comprising a width of 0.60 m and a length of 1.80 m (Figure 7.1) The boundary layer was tripped using distributed roughness elements of 1.0 cm in height, following the work of [Kempaiah et al. \(2020\)](#). TBL parameters are listed in Table 7.1 and were determined from the measured velocity profile of the uncontrolled flow (Figure 7.3, described later).

Table 7.1: TBL parameters at $x_s = 1.535$ m.

Re_τ	Re_θ	δ	θ	u_τ	H
910	1950	87 mm	8.8 mm	0.15 m/s	2.03

An array of 4×3 flush-mounted rotating discs (refer Figure 7.2) was designed per the optimal case in terms of the largest drag reduction identified by [Ricco and Hahn \(2013\)](#): a disc diameter of $D^+ = 550$ and a disc-edge velocity of $W^+ = 10$. Even though their Reynolds number was relatively low ($Re_\tau = 180$), this type of actuation method targets the near-wall cycle turbulence and should therefore adhere to a viscous scaling. With the current boundary layer parameters of Ta-

ble 7.1, the disc diameter became $D = 0.055$ m. The array was constructed with streamwise and spanwise spacings of 0.083 m ($1.5D$) and 0.065 m ($1.2D$), respectively, to allow mounting of the DC electric motors to the bottom side of the plate. Each motor contained a double ball-bearing shaft to which the discs were directly mounted. All motors were powered with a single power supply and their angular velocities, Ω , were measured using a tachometer. Variations in Ω of each individual disc were less than 3% of the mean Ω . This work includes results corresponding to two different edge velocities, $W^+ = 10$ and $W^+ = 25$. So the former corresponds to the largest friction drag reduction, while the latter should result in an increase of friction drag (see Figure 2b of [Ricco and Hahn, 2013](#)).



Figure 7.2: Picture of the disc array as viewed from the top and bottom, the white tape on the discs was used to measure the angular velocities using a tachometer.

7.2.2. PIV SETUP

Planar-PIV measurements were performed in two configurations, being (1) a streamwise wall-normal (x, y) -plane, and (2) a wall-parallel (x, z) -plane. The (x, y) -plane measurements were conducted over the centreline of the most downstream disc, and were imaged using a single camera, labelled as ‘P1’ in Figure 7.1. The (x, z) -plane measurements were performed using two cameras (‘P2’ and ‘P3’ in Figure 7.1) and the total field-of-view (FOV) covered the entire disc-array. The exact height of the wall-parallel plane ($y^+ = 70$) was determined a-posteriori by comparing the mean velocity in the plane to the mean velocity profile extracted from the (x, y) -plane measurements. Finally, stereo-PIV measurements were performed in a wall-normal-spanwise (y, z) -plane, downstream of the aft-centre disc at $x_s = 1.67$ m (roughly $0.45D$ behind the disc-array). Two cameras were employed (‘P4’ and ‘P5’ in Figure 7.1) and were situated outside of the flow, placed at a stereoscopic angle of 55° .

For PIV acquisition, the flow was seeded with fog droplets of $1 \mu\text{m}$ diameter,

produced with a SAFEX fog generator. Illumination was provided by a Quantel Evergreen 200 laser (Nd:YAG, 2×200 mJ, 15 Hz) and the laser sheet thickness was on the order of 1 mm. Images were captured using LaVision Imager sCMOS cameras (2560×2160 px², 16 bits and $6.5 \mu\text{m}$ pixel size) equipped with Nikon lenses of 105 mm focal length. Post-processing employed an image interrogation using the multi-pass cross-correlation including window refinement and deformation; non-isotropic windows were used for the (x, y) -plane measurements to increase the wall-normal resolution. Further details of the PIV processing and resolutions of the velocity fields are provided in Table 7.2.

Table 7.2: Summary of PIV measurements (note: different configurations were not acquired simultaneously).

Type	# of cameras	Field-of-view	Image res.	Interrog. window	Vector pitch
Planar (x, y)	1 (P1)	$75 \times 63 \text{ mm}^2$	34 px/mm	$32 \times 8 \text{ px}^2$	0.12 mm
Planar (x, z)	2 (P2 & P3)	$250 \times 210 \text{ mm}^2$	10 px/mm	$24 \times 24 \text{ px}^2$	0.25 mm
Stereo (y, z)	2 (P4 & P5)	$55 \times 55 \text{ mm}^2$	30 px/mm	$64 \times 64 \text{ px}^2$	0.50 mm

7.3. RESULTS

7.3.1. BOUNDARY LAYER ASSESSMENT

Figures 7.3(a) and 7.3(b) present profiles of the mean velocity and the Reynolds stresses, respectively. Profiles are generated by streamwise averaging the (x, z) -plane PIV data over the streamwise extent of the aft disc. First, the profiles of the uncontrolled case ($W^+ = 0$) are compared to profiles of DNS data of TBL flows, extracted from Schlatter and Örlü (2010). The wall-normal trends from the experimental data, of both the mean velocity u and the Reynolds stresses $\langle u'_i u'_j \rangle^+$, show a good agreement with the DNS data in the inner region. Discrepancies in the outer-region are described to the favorable pressure gradient of the experimental flow (constant cross-sectional area wind tunnel in which the flat plate is suspended).

For the case of optimal control ($W^+ = 10$), velocity data is available only for $y^+ < 100$. That is, the FOV was decreased in size to achieve a higher near-wall resolution. When inspecting the mean velocity profile (scaled by the u_τ of the uncontrolled case), it is evident that the velocity decreases below $y^+ \approx 10$. This indicates a reduction of the average friction drag at the centre-spanwise loca-

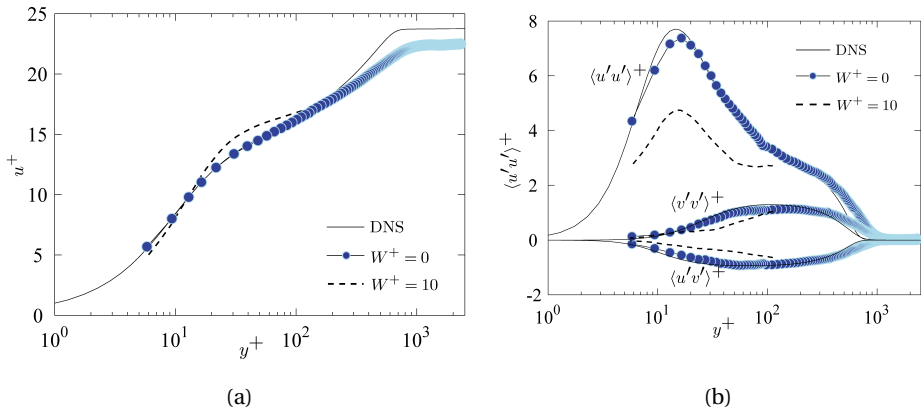


Figure 7.3: (a) Streamwise mean velocity profile for the uncontrolled ($W^+ = 0$) and controlled ($W^+ = 10$) cases, and (b) the corresponding profiles of all Reynolds stresses in the (x, y) -plane. Only every 2nd PIV data point is shown for clarity of the graphs, and DNS profiles are taken from [Schlatter and Örlü \(2010\)](#).

tion where the measurement was taken. Moreover, a peak-to-peak reduction of 30% in $\langle u'u' \rangle^+$ occurs, together with significant reductions in the magnitudes of $\langle u'v' \rangle^+$ and $\langle v'v' \rangle^+$ below $y^+ \approx 100$. A reduction of the mean velocity and turbulence intensities is associated with a reduction in turbulent friction drag generation ([Baron and Quadrio, 1995](#)). Note that our study is the first demonstration-experiment, but that a direct determination of the reduction in friction drag was not reliable, due to wall-reflections of the rotating discs and minor vibrations in the setup. As a consequence of the non-uniform actuation in the span, the wall-drag modification also depends strongly on the z location (and x), as detailed in the work of [Ricco and Hahn \(2013\)](#). Nevertheless, we here continue with a description of how the rotating disc-array affects the large-scale flow organization. For this we inspect the other two PIV measurement configurations, described next.

7.3.2. LARGE SCALE FLOW ORGANIZATION

The normalised streamwise velocity in the wall-parallel plane at a height of $y^+ = 70$ (Figure 7.4a-c) shows low- and high-momentum pathways, in streamwise-aligned regions over the centre of the discs and in between them, respectively. For the case of optimal control ($W^+ = 10$), the flow over the spanwise-centred disc most aft in the array has a higher velocity, being consistent with Figure 7.3(a). It is evident that the increase and decrease of the velocity in these low- and high-momentum pathways is strengthened when moving towards the case of $W^+ = 25$

(Figure 7.4c). For all cases, the mean velocity slightly decreases towards the end of the measurement region ($x/D \rightarrow 7$) because of the streamwise development of the TBL flow. The effect of control also increases significantly with downstream distance, due to the relatively short extent of the array in x .

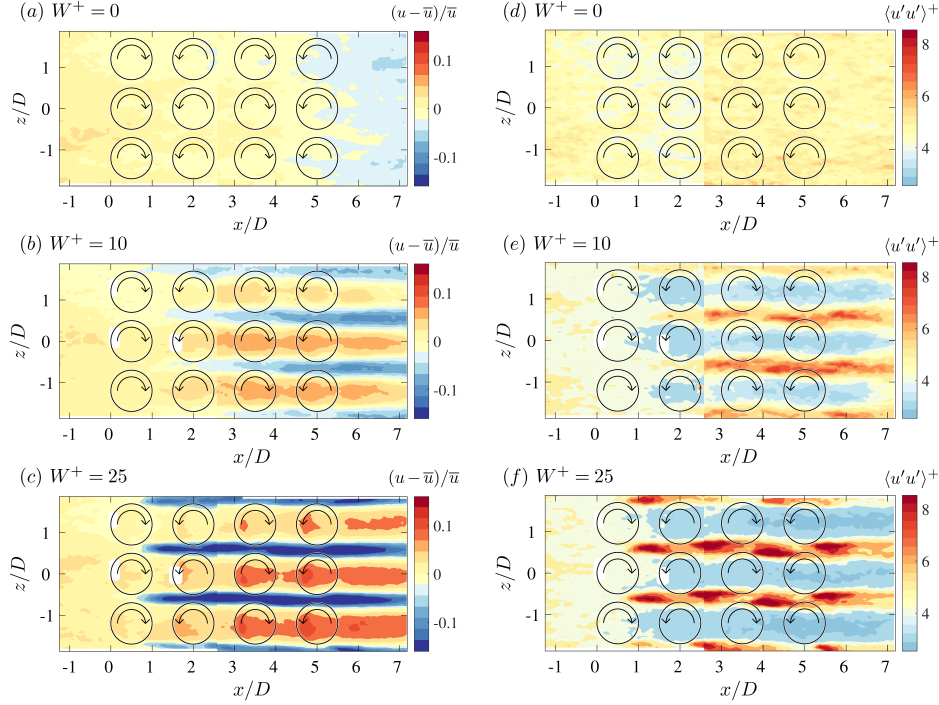


Figure 7.4: (a-c) Contours of the in-plane streamwise velocity, where \bar{u} is the mean velocity of the entire wall-parallel plane of the uncontrolled case, $W^+ = 0$. (d-f) Contours of the streamwise Reynolds stress, all normalized with the u_τ in table 7.1. Edges of the discs, and their rotation direction, are drawn in black; small white regions mask spurious vectors, which were a consequence of laser reflections on the discs.

Recall that a relatively high-speed region at $y^+ = 70$ corresponds to a relatively low-speed region lower in the boundary layer. In this context, the occurrence of low-momentum pathways very close to the wall, over the spanwise centre of the discs, was attributed to a viscous sub-layer being produced by a radial flow from the von Kármán pumping effect that is highly pronounced in the regions between the discs (Wise et al., 2014). Wall-parallel planes of velocity at lower heights are challenging to acquire, due to laser wall-reflections and alignment issues and the current planes are therefore a surrogate of the trends very near-the-wall, when interchanging the low- and high-momentum pathways. In order to make a qualitative comparison of how the mean flow is organized in

the spanwise direction, the wall-parallel planes are streamwise-averaged in the region downstream of the aft row of discs, in the range $5.5 \leq x/D \leq 7$. The spanwise profiles for all cases of W^+ are shown in Figure 7.5. Notably, the regions of a velocity deficit in the case of control is narrower than the region of velocity surplus, but is more intense. Averaging the spanwise velocity over one periodic-unit of the flow ($-0.6 \leq z/D \leq 0.6$) yields the three vertical lines in Figure 7.5, indicating a monotonic trend towards a higher mean velocity when W^+ increases. Only when the wall-normal profiles (varying along the span) collapse in outer-scaling (adhering to a so-called ‘outer-layer similarity’), at this wall-normal height, the spanwise trend and thus the average can be a surrogate for the spanwise variation in friction drag. An interpretation of Figure 7.5 in this context is too speculative, given that the outer-layer similarity has not been confirmed, because of the relatively low acquisition location of the wall-parallel plane (below the onset of the logarithmic layer at $y^+ = 100$), and because of the streamwise development still taking place at the aft end of the array. Regardless, the current results show that the actuation method using rotating discs can establish low- and high-momentum pathways; the implications of this for future studies of this control technique are further discussed in the next section considering the cross-planes of velocity.

A final remark about the data in the wall-parallel plane is concerned with the regions of high and low Reynolds stress $\langle u' u' \rangle^+$, in comparison to the uncontrolled case. When focusing on the intense (red) patches of $\langle u' u' \rangle^+$ in Figure 7.4e,f, it is observed that these are located just downstream of each row of discs. When accepting that coherent turbulent structures are inclined by roughly 20° relatively to the wall, the observations at $y^+ = 70$ originated from the wall at a distance of $\Delta x^+ = 70 / \tan(20^\circ)$ upstream, equating to $\Delta x/D \approx 0.36$. This upstream shift would align the red patches of intense $\langle u' u' \rangle^+$ with the ‘narrow passages’ in between the discs. Their spanwise location depends on the rotation-direction of each row of discs.

Figure 7.6 displays data of the cross-plane stereo-PIV field, located just aft of the array. For both the uncontrolled ($W^+ = 0$) and optimal control case, the fields of the mean streamwise velocity u and Reynolds stress $\langle u' u' \rangle^+$ are shown. Note that the spanwise range covers the span of the disc located at $z = 0$. In comparison to the spanwise-invariant mean flow of the uncontrolled case, a clear spanwise modulation of the velocity iso-contours appears in the case of $W^+ = 10$. This reflects the same observations that were made in Figure 7.5 (the wall-normal height of the wall-parallel plane is shown with the horizontal dashed line in all sub-plots of Figure 7.6): for a given height above the viscous sublayer, a higher mean velocity occurs in the disc centre, while the flow velocity is lower at the edges of the disc. Thus, the flow over the centre of the disc exhibits less

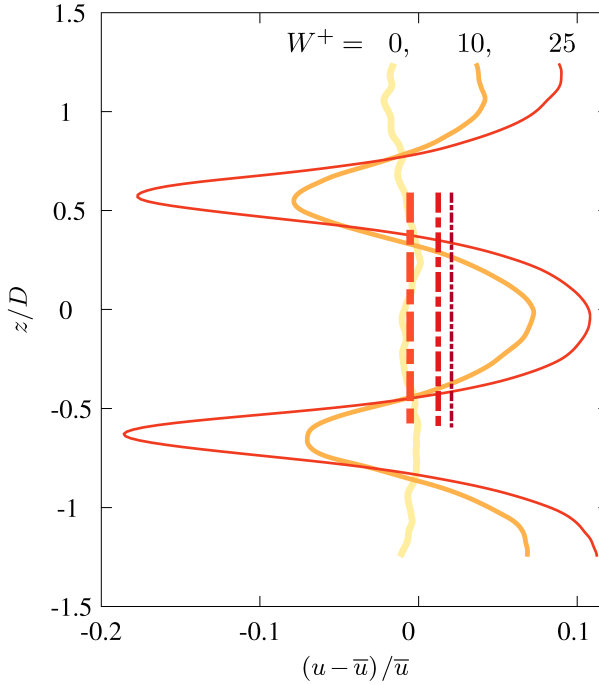


Figure 7.5: Spanwise profiles of the streamwise-averaged u -velocity component of Figure 7.4a-c, in the range $5.5 \leq x/D \leq 7$. Spanwise averages of these profiles, for one periodic-unit, are shown with the vertical lines for the range $-0.6 \leq z/D \leq 0.6$.

momentum-deficit. From the topology of $\langle u'u' \rangle^+$ it is evident that for approximately $-0.25 \leq z/D \leq 0.25$, the streamwise Reynolds stress is constant in span and suppressed in comparison to the uncontrolled case.

At this stage it is worth mentioning that the large-scale flow organization over the disc array is strongly reminiscent of the one found over other wall-bounded turbulent flows with spanwise varying surface conditions. Specifically, wall-bounded turbulence convecting over walls with streamwise-aligned patches of (various degrees of) roughness, with a spanwise periodicity, are known to include large-scale secondary flows and the low- and high-momentum pathways discussed earlier with the aid of Figure 7.4. Details of such flows can be found elsewhere (Barros and Christensen, 2014; Nugroho et al., 2013; Vanderwel and Ganapathisubramani, 2015, among others). A main difference between those flows and the one currently studied is that our actuation method achieves the spanwise varying friction drag with hydrodynamically-smooth rotating discs (having no pressure drag). To the contrary, the aforementioned studies in the literature comprise

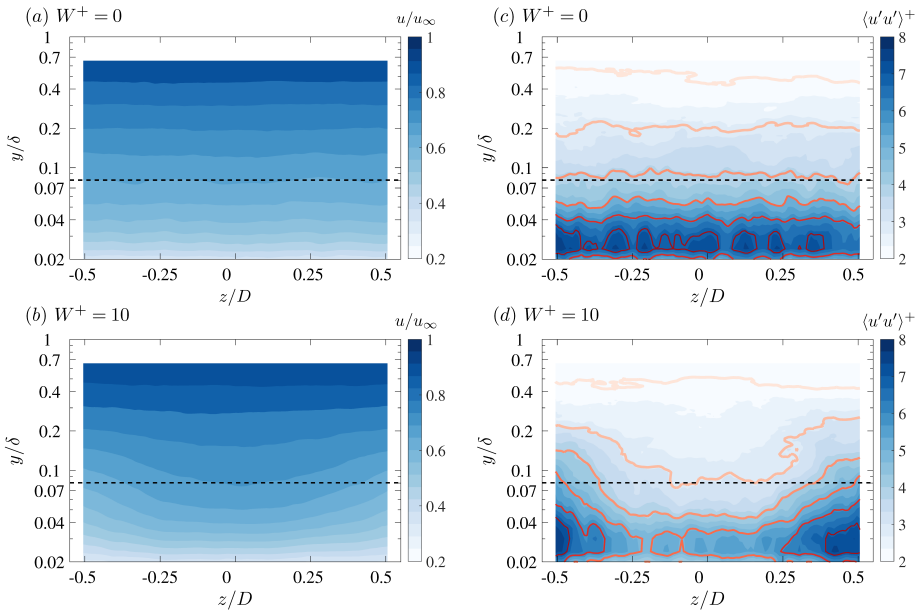


Figure 7.6: Contours of (a,b) the streamwise velocity and (c,d) the streamwise Reynolds stress for both $W^+ = 0$ and $W^+ = 10$. Note that the ordinate has a logarithmic scale. For clarity, the set of red-shaded lines on (c,d) are iso-contours at $\langle u'u' \rangle^+ = 2:1:7$.

7

walls with pressure drag (e.g., streamwise-aligned roughness-patches of a certain width). The actuation method with the rotating disc does come however with a non-negligible power requirement for rotating the discs (Ricco and Hahn, 2013). All in all, having demonstrated that this actuation method is capable of establishing large-scale flow (re)organization, the variation in control ‘authority’ in terms of disc sizing, layout, and rate-of-rotation makes this actuation method an attractive candidate when exploring control of high Reynolds number flows. Those conditions remain unexplored with DNS and the current experimental work is a step towards this.

7.4. CONCLUSION

An experimental investigation of the large-scale flow organization over an array of flush-mounted rotating discs under a turbulent boundary layer was conducted. Different configurations of PIV measurements were employed to reveal (and confirm in relation to the available literature on the topic) that low- and high-momentum pathways are established in the flow, due to the spanwise varying friction drag. It was recently found in a study with a fixed spanwise varying surface treatment that the spanwise wavelength (or disc size) governs the

size and strength of the secondary flows (Wangsawijaya and Hutchins, 2022). In that study, the authors interpreted the secondary flows as spanwise-locked large-scale turbulent structures that are present even in smooth-wall turbulent boundary layers (but without preferred spanwise positioning). It is postulated that the actuation method using flush-mounted rotating discs will have a large control authority for the organization of large-scale flow features; this can be beneficial in terms of friction drag reduction technologies at high Reynolds number conditions. Particularly due to the total absence of pressure drag with this control system (but, the power for spinning the discs should be accounted for). In the future, it will be interesting to examine if discs can be sized/laid out to increase the benefit of the reduced flow-induced friction in the centre area of the discs, so that it leads to a global friction drag reduction.

8

CONCLUSION

*Change is inevitable.
Growth is optional.*

John C. Maxwell

The current chapter summarizes the main results and findings from the investigations undertaken in the current dissertation. The methodologies and the underlying physical mechanisms are discussed, with a focus on the outcomes that are relevant for further investigation, possible paths towards practical implementation and the inherent drawbacks.

8.1. MECHANICAL WALL OSCILLATIONS

From the investigations reported in Chapter 4, the response of a turbulent boundary layer developing over a mechanically oscillating wall has been successfully investigated experimentally using planar and tomographic PIV. High-resolution planar PIV enabled accurate measurement of the wall shear stress directly from the velocity profile. As a result, a maximum drag reduction of 15% was quantified for the oscillating wall at optimum operating conditions. The reductions obtained agreed well with previously reported literature employing DNS. The results discussed are the first direct experimental verifications of the computational studies.

An in-depth analysis showed a significant reduction of turbulent stresses and pre-multiplied turbulent kinetic energy production in the near-wall regions. The instantaneous vorticity fields visualised in the planar and tomographic-PIV measurements revealed marked differences between the stationary and the oscillating wall. Planar-PIV data provided evidence by visualising the cross-sectional footprints of the highly three-dimensional coherent structures.

Based on the qualitative observations of the coherent structures, a hypothesis was forwarded to explain the observed reduction in near-wall vorticity and the accompanying reduction of the number of hairpins in a hairpin packet during wall oscillation. In line with this model, the hairpin packet formation depends on the motion of the oscillating wall and the phase in the oscillation cycle.

The corresponding results, observations and hypothesis necessitated the implementation of the feature detection algorithm to provide the relevant quantitative results to verify the hypothesis, which was the focus of Chapter 5.

However, as elaborated in the discussions, it is clear that spanwise wall oscillation is only relevant to a laboratory environment for exploratory analysis and at low Reynolds numbers. Therefore, a possible path towards practically implementing this technique is to develop alternate surrogate methods that produce similar underlying forcing. For example, plasma actuators (Hehner et al., 2020; Thomas et al., 2019), Kagome lattice (Bird et al., 2018), electroactive polymers (Gatti et al., 2015; Gouder et al., 2013).

However, several challenges associated with near-wall control at more significant Reynolds numbers exist. The near wall region where the forcing is desired will be in the μm scale, leading to additional challenges. Therefore, using the above techniques to control large and very-large-scale structures in the logarithmic and outer region of the TBL is expected to lead to successful implementations.

8.2. MECHANISM OF SKIN-FRICTION REDUCTIONS

Adopting a feature detection algorithm in Chapter 5 enabled quantifying the effect of wall oscillations on the streaks and ejections in the near wall region of a turbulent boundary layer subjected to spanwise wall oscillations. Experimental data in the near-wall region $y^+ = [20 - 80]$ collected with tomographic-PIV was examined to infer statistical properties. The developed feature detection algorithm was compared with the more standard correlation techniques. The latter appears to return limited information on the properties and arrangement due to the spatial averaging effect. On the other hand, the feature detection algorithm isolates the individual features of interest and is based on the instantaneous distribution of Reynolds stress. As a result, the feature detection algorithm quantified a decrease in the spatial occupation and length of the ejection events by 40% and 20%, respectively. Furthermore, due to the discrete nature of the feature detection algorithm, it appears to be more robust and less affected by data dispersion during the averaging.

The results from the inclinations of the streaks and ejections show a clear phase dependence, as hypothesised in Chapter 4, between the sidewise tilt and the wall motion for the identified events. Furthermore, a significantly higher probability of events with larger tilt is observed as a result of the wall oscillation. The maximum observed tilt angle of approximately 20° is consistent with proposed estimates based on geometric or kinematic criteria. The overall behaviour and properties of streaks and ejections observed here are consistent with the conceptual model whereby wall oscillations successfully weaken the early formation of hairpins in the near-wall cycle of the turbulent boundary layer by inhibiting hairpin auto-generation and, in turn, reducing the occurrence of energetic lift-up events.

8.3. EXTENSION TO LARGE REYNOLDS NUMBERS

8.3.1. PLASMA SURROGATE OF WALL OSCILLATIONS

Chapter 6 documents the attempt to surrogate the spanwise wall oscillations with AC-DBD-based unsteady, uni-direction plasma actuators. The jet topology, thickness, and maximum induced velocity were chosen to be the parameters that dictated the choice of the actuator. Initial testing in quiescent conditions resulted in the development of an A4-sized actuator array, with 5 mm and 3mm dimensions for the exposed and covered electrode with a gap of 8 mm. The input signal chosen to be the best surrogate for the SWO was the square wave at a duty cycle of 50% actuated at 15Hz. In addition, the plasma-induced flow topology showed differences in the region away from the wall when actuated in the presence of the oncoming turbulent boundary layer.

Skin-friction measurements immediately downstream of the unsteady, uni-directional AC-DBD plasma actuator reported a consistent increase in the skin-friction and momentum deficit throughout the boundary layer. The two features that appear to limit the successful surrogation of the SWO were found to be the discrete and unsteady nature of the forcing. The unsteadiness leads to the formation of a starting vortex, which cannot be avoided and leads to a complex non-linear interaction with the flow in the near-wall regions of the turbulent boundary layer. As a result, it is concluded that the chosen form of the actuator cannot be used to surrogate the SWO, and skin-friction changes that are observed cannot be ascribed to the mechanism of inhibition of hairpin auto-generation.

Therefore, a steady AC-DBD actuator is developed based on the learnings of the earlier attempt. The steady actuator attempts to surrogate the standing wave concept proposed through the DNS simulations of [Viotti et al. \(2009\)](#). Standing wave forcing with wavelengths (λ^+) in the range of [200-950] were developed in the quiescent conditions. The forcing obtained from these actuators corresponds well with Stoke's first problem ([Stokes, 1851](#)) with peak velocity achieved very close to the wall ($y = 0.8$ mm) compared to the unsteady, uni-direction actuator ($y = 3.0$ mm). This leads to better confinement of the jet near the wall and indicates a potential for further investigations.

8.3.2. ARRAY OF FLUSH MOUNTED ROTATING DISCS

In Chapter 7, an alternative path for the practical scalability of spanwise wall oscillations is attempted using an array of flush-mounted rotating discs. The practical implementation of this actuation method is relatively easy as it does not require any oscillatory, linear motion but is based on steady rotational motion. The array of discs was designed and manufactured based on the optimal case in terms of the largest drag reduction, as identified by [Ricco and Hahn \(2013\)](#).

Flow field investigations of the array in the wall-normal plane showed low and high momentum pathways that were established in the flow due to the spanwise varying friction drag. In addition, patches of the increased streamwise Reynolds stresses were quantified, located just downstream of each row of discs and dependent on the rotational direction of each row of discs. Quantifying the local skin friction was unsuccessful due to challenges with reflection and the inhomogeneity in the spatial variation. The motion of the discs appears to create a suction effect for the flow over them. Thus, the flow over the centre of the discs exhibits less momentum deficit and is most evident for z/D between -0.25 and 0.25.

The large-scale flow organisation over the disc array is similar to that found over other wall-bounded turbulent flows with spanwise varying surface conditions. A primary difference between those flows and the one currently studied is

that our actuation method achieves the spanwise variable friction drag with hydrodynamically smooth rotating discs (having no pressure drag). All in all, having demonstrated that this actuation method can establish large-scale flow (re)organisation, the variation in control ‘authority’ in terms of disc sizing, layout, and rate-of-rotation makes this actuation method an attractive candidate when exploring control of high Reynolds number flows. Those conditions remain unexplored with DNS, and the current experimental work is a step towards this. In the future, it will be interesting to examine if discs can be sized/laid out to increase the benefit of the reduced flow-induced friction in the centre area of the discs so that it leads to a global friction drag reduction.

REFERENCES

- Abbas, A., Bugeđa, G., Ferrer, E., Fu, S., Periaux, J., Pons-Prats, J., Valero, E., and Zheng, Y. (2017). Drag reduction via turbulent boundary layer flow control. *Science China Technological Sciences*, 60(9):1281–1290.
- Adrian, R. (1997). Dynamic ranges of velocity and spatial resolution of particle image velocimetry. *Measurement Science and Technology*, 8(12):1393.
- Adrian, R. J. (2007). Hairpin vortex organization in wall turbulence. *Physics of fluids*, 19(4):041301.
- Adrian, R. J., Meinhart, C. D., and Tomkins, C. D. (2000). Vortex organization in the outer region of the turbulent boundary layer. *Journal of fluid Mechanics*, 422:1–54.
- Adrian, R. J. and Westerweel, J. (2011). *Particle image velocimetry*. Number 30. Cambridge university press.
- Agostini, L., Toubert, E., and Leschziner, M. A. (2014). Spanwise oscillatory wall motion in channel flow: drag-reduction mechanisms inferred from dns-predicted phase-wise property variations at. *Journal of Fluid Mechanics*, 743:606–635.
- Altıntaş, A., Davidson, L., and Peng, S.-H. (2020). Direct numerical simulation of drag reduction by spanwise oscillating dielectric barrier discharge plasma force. *Physics of Fluids*, 32(7):075101.
- Anderson, J. (2011). *EBOOK: Fundamentals of Aerodynamics (SI units)*. McGraw Hill.
- Auteri, E., Baron, A., Belan, M., Campanardi, G., and Quadrio, M. (2010). Experimental assessment of drag reduction by traveling waves in a turbulent pipe flow. *Physics of Fluids*, 22(11):115103.
- Bae, H. J. and Lee, M. (2021). Life cycle of streaks in the buffer layer of wall-bounded turbulence. *Physical Review Fluids*, 6(6):064603.
- Baron, A. and Quadrio, M. (1995). Turbulent drag reduction by spanwise wall oscillations. *Applied Scientific Research*, 55(4):311–326.

- Barros, J. M. and Christensen, K. T. (2014). Observations of turbulent secondary flows in a rough-wall boundary layer. *Journal of Fluid Mechanics*, 748:R1.
- Bernard, P. S., Thomas, J. M., and Handler, R. A. (1993). Vortex dynamics and the production of reynolds stress. *Journal of Fluid Mechanics*, 253:385–419.
- Bird, J., Santer, M., and Morrison, J. F. (2018). Experimental control of turbulent boundary layers with in-plane travelling waves. *Flow, turbulence and combustion*, 100(4):1015–1035.
- Bradshaw, P. and Pontikos, N. (1985). Measurements in the turbulent boundary layer on an ‘infinite’ swept wing. *Journal of Fluid Mechanics*, 159:105–130.
- Chen, D., Rojas, M., Samset, B., Cobb, K., Diongue Niang, A., Edwards, P., Emori, S., Faria, S., Hawkins, E., Hope, P., et al. (2021). Framing, context, and methods. *Climate change*.
- Cheng, X., Wong, C., Hussain, F., Schröder, W., and Zhou, Y. (2021). Flat plate drag reduction using plasma-generated streamwise vortices. *Journal of Fluid Mechanics*, 918.
- Choi, H., Moin, P., and Kim, J. (1994). Active turbulence control for drag reduction in wall-bounded flows. *Journal of Fluid Mechanics*, 262:75–110.
- Choi, K.-S. (1989). Near-wall structure of a turbulent boundary layer with riblets. *Journal of fluid mechanics*, 208:417–458.
- Choi, K.-S. (2002). Near-wall structure of turbulent boundary layer with spanwise-wall oscillation. *Physics of Fluids*, 14(7):2530–2542.
- Choi, K.-S., DeBisschop, J.-R., and Clayton, B. R. (1998). Turbulent boundary-layer control by means of spanwise-wall oscillation. *AIAA journal*, 36(7):1157–1163.
- Coleman, H. and Steele Jr, W. (2009). Uncertainty in a result determined from multiple variables. *Experimentation, Validation, and Uncertainty Analysis for Engineers*, 3:61–83.
- Coles, D. (1962). The turbulent boundary layer in a compressible fluid, rand corp.
- Corino, E. R. and Brodkey, R. S. (1969). A visual investigation of the wall region in turbulent flow. *Journal of Fluid Mechanics*, 37(1):1–30.
- Corke, T. C., Enloe, C. L., and Wilkinson, S. P. (2010). Dielectric barrier discharge plasma actuators for flow control. *Annual review of fluid mechanics*, 42:505–529.

- Coxe, D. J., Peet, Y. T., and Adrian, R. J. (2019). Vorticity statistics and distributions in drag reduced turbulent pipe flow with transverse wall oscillations. In *Turbulence and shear flow phenomena*.
- Del Alamo, J. C. and Jiménez, J. (2009). Estimation of turbulent convection velocities and corrections to Taylor's approximation. *Journal of Fluid Mechanics*, 640:5–26.
- Di Cicca, G. M., Iuso, G., Spazzini, P. G., and Onorato, M. (2002). Particle image velocimetry investigation of a turbulent boundary layer manipulated by spanwise wall oscillations. *Journal of Fluid Mechanics*, 467:41–56.
- Djenidi, L., Anselmet, F., Liandrat, J., and Fulachier, L. (1994). Laminar boundary layer over riblets. *Physics of Fluids*, 6(9):2993–2999.
- Dong, H., Zhang, Y., Deng, F., and Liu, W. (2019). The research on fluid properties with spanwise-wall oscillation by LES model. In *2019 IEEE 4th International Conference on Advanced Robotics and Mechatronics (ICARM)*, pages 966–969. IEEE.
- Driver, D. M. and Hebbbar, S. K. (1987). Experimental study of a three-dimensional, shear-driven, turbulent boundary layer. *AIAA journal*, 25(1):35–42.
- Elsinga, G. E., Scarano, F., Wieneke, B., and van Oudheusden, B. W. (2006). Tomographic particle image velocimetry. *Experiments in fluids*, 41(6):933–947.
- Gad-el Hak, M. (1996). Modern developments in flow control.
- Gad-el Hak, M. and Bandyopadhyay, P. R. (1994). Reynolds number effects in wall-bounded turbulent flows.
- Gan, L., Cardesa-Duenas, J., Michaelis, D., and Dawson, J. (2012). Comparison of tomographic PIV algorithms on resolving coherent structures in locally isotropic turbulence. In *Proceedings of the 16th International Symposium on Applications of Laser Techniques to Fluid Mechanics, Lisbon, Portugal*, pages 9–12.
- Ganapathisubramani, B., Longmire, E. K., and Marusic, I. (2003). Characteristics of vortex packets in turbulent boundary layers. *Journal of Fluid Mechanics*, 478:35–46.
- García-Mayoral, R. and Jiménez, J. (2011). Drag reduction by riblets. *Philosophical transactions of the Royal Society A: Mathematical, physical and engineering Sciences*, 369(1940):1412–1427.

- Gatti, D., Güttler, A., Frohnäpfel, B., and Tropea, C. (2015). Experimental assessment of spanwise-oscillating dielectric electroactive surfaces for turbulent drag reduction in an air channel flow. *Experiments in Fluids*, 56(5):1–15.
- Gatti, D. and Quadrio, M. (2013). Performance losses of drag-reducing spanwise forcing at moderate values of the reynolds number. *Physics of Fluids*, 25(12):125109.
- Gatti, D. and Quadrio, M. (2016). Reynolds-number dependence of turbulent skin-friction drag reduction induced by spanwise forcing. *Journal of Fluid Mechanics*, 802:553–582.
- Gatti, D., Stroh, A., Frohnäpfel, B., and Hasegawa, Y. (2018). Predicting turbulent spectra in drag-reduced flows. *Flow, Turbulence and Combustion*, 100(4):1081–1099.
- Ghaemi, S. and Scarano, F. (2010). Multi-pass light amplification for tomographic particle image velocimetry applications. *Measurement science and technology*, 21(12):127002.
- Goudar, M. V., Breugem, W.-P., and Elsinga, G. (2016). Auto-generation in wall turbulence by the interaction of weak eddies. *Physics of Fluids*, 28(3):035111.
- Gouder, K., Potter, M., and Morrison, J. F. (2013). Turbulent friction drag reduction using electroactive polymer and electromagnetically driven surfaces. *Experiments in fluids*, 54(1):1–12.
- Hamilton, J. M., Kim, J., and Waleffe, F. (1995). Regeneration mechanisms of near-wall turbulence structures. *Journal of Fluid Mechanics*, 287:317–348.
- Haralick, R. M., Shapiro, L. G., et al. (1992). *Computer and robot vision*, volume 1. Addison-wesley Reading.
- He, C., Corke, T. C., and Patel, M. P. (2009). Plasma flaps and slats: An application of weakly ionized plasma actuators. *Journal of Aircraft*, 46(3):864–873.
- Head, M. and Bandyopadhyay, P. (1981). New aspects of turbulent boundary-layer structure. *Journal of fluid mechanics*, 107:297–338.
- Hehner, M. T., Gatti, D., and Kriegseis, J. (2019). Stokes-layer formation under absence of moving parts—a novel oscillatory plasma actuator design for turbulent drag reduction. *Physics of Fluids*, 31(5):051701.

- Hehner, M. T., Gatti, D., Mattern, P., Kotsonis, M., and Kriegseis, J. (2020). Virtual wall oscillations forced by a dbd plasma actuator operating under beat frequency—a concept for turbulent drag reduction. In *AIAA Aviation 2020 Forum*, page 2956.
- Hurst, E., Yang, Q., and Chung, Y. M. (2014). The effect of reynolds number on turbulent drag reduction by streamwise travelling waves. *Journal of fluid mechanics*, 759:28–55.
- Hutchins, N. and Marusic, I. (2007). Evidence of very long meandering features in the logarithmic region of turbulent boundary layers. *Journal of Fluid Mechanics*, 579:1–28.
- Jentsch, A. and Beierkuhnlein, C. (2008). Research frontiers in climate change: effects of extreme meteorological events on ecosystems. *Comptes Rendus Geoscience*, 340(9-10):621–628.
- Jeong, J., Hussain, F., Schoppa, W., and Kim, J. (1997). Coherent structures near the wall in a turbulent channel flow. *Journal of Fluid Mechanics*, 332:185–214.
- Jiang, X., Lee, C., Smith, C., Chen, J., and Linden, P. (2020). Experimental study on low-speed streaks in a turbulent boundary layer at low reynolds number. *Journal of Fluid Mechanics*, 903.
- Jiménez, J., Hoyas, S., Simens, M. P., and Mizuno, Y. (2010). Turbulent boundary layers and channels at moderate reynolds numbers. *Journal of Fluid Mechanics*, 657:335–360.
- Jiménez, J. and Pinelli, A. (1999). The autonomous cycle of near-wall turbulence. *Journal of Fluid Mechanics*, 389:335–359.
- Jodai, Y. and Elsinga, G. (2016). Experimental observation of hairpin auto-generation events in a turbulent boundary layer. *Journal of Fluid Mechanics*, 795:611–633.
- Joslin, R. D. (1998). Aircraft laminar flow control. *Annual review of fluid mechanics*, 30(1):1–29.
- Jukes, T., Choi, K.-S., Johnson, G., and Scott, S. (2004). Turbulent boundary-layer control for drag reduction using surface plasma. In *2nd AIAA flow control conference*, page 2216.
- Jukes, T., Choi, K.-S., Johnson, G., and Scott, S. (2006). Turbulent drag reduction by surface plasma through spanwise flow oscillation. In *3rd AIAA Flow Control Conference*, page 3693.

- Jung, W.-J., Mangiavacchi, N., and Akhavan, R. (1992). Suppression of turbulence in wall-bounded flows by high-frequency spanwise oscillations. *Physics of Fluids A: Fluid Dynamics*, 4(8):1605–1607.
- Jux, C. (2022). Development of robotic volumetric piv: with applications in sports aerodynamics.
- Kähler, C. (2004). Investigation of the spatio-temporal flow structure in the buffer region of a turbulent boundary layer by means of multiplane stereo piv. *Experiments in Fluids*, 36:114–130.
- Kähler, C. J., Scholz, U., and Ortmanns, J. (2006). Wall-shear-stress and near-wall turbulence measurements up to single pixel resolution by means of long-distance micro-piv. *Experiments in fluids*, 41:327–341.
- Keefe, L. and Keefe, L. (1997). A normal vorticity actuator for near-wall modification of turbulent shear flows. In *35th Aerospace Sciences Meeting and Exhibit*, page 547.
- Kempaiah, K. U. and Scarano, F. (2022). Feature-based analysis of a turbulent boundary layer under spanwise wall oscillation. *Physics of Fluids*, 34(11):115152.
- Kempaiah, K. U., Scarano, F., Elsinga, G. E., Van Oudheusden, B. W., and Bermel, L. (2020). 3-dimensional particle image velocimetry based evaluation of turbulent skin-friction reduction by spanwise wall oscillation. *Physics of Fluids*, 32(8):085111.
- Kempaiah, K. U., Sem, J., and Baars, W. J. (2022). Large-scale flow organization of wall-bounded turbulence over flush-mounted rotating discs. In *12th International Symposium on Turbulence and Shear Flow Phenomena (TSFP12) Osaka, Japan, July 19–22, 2022*.
- Kim, J. (2012). Progress in pipe and channel flow turbulence, 1961–2011. *Journal of Turbulence*, (13):N45.
- Kim, J., Moin, P., and Moser, R. (1987). Turbulence statistics in fully developed channel flow at low reynolds number. *Journal of fluid mechanics*, 177:133–166.
- Kim, K. C. and Adrian, R. J. (1999). Very large-scale motion in the outer layer. *Physics of Fluids*, 11(2):417–422.
- Kline, S. and Robinson, S. (1990). Turbulent boundary layer structure: Progress, status, and challenges. *Structure of Turbulence and Drag Reduction*, pages 3–22.

- Kline, S. J., Reynolds, W. C., Schraub, F., and Runstadler, P. (1967). The structure of turbulent boundary layers. *Journal of Fluid Mechanics*, 30(4):741–773.
- Koch, H. and Kozulovic, D. (2013). Drag reduction by boundary layer control with passively moving wall. In *Fluids Engineering Division Summer Meeting*, volume 55553, page V01BT15A004. American Society of Mechanical Engineers.
- Kotsonis, M. (2015). Diagnostics for characterisation of plasma actuators. *Measurement Science and Technology*, 26(9):092001.
- Kotsonis, M., Ghaemi, S., Veldhuis, L., and Scarano, F. (2011). Measurement of the body force field of plasma actuators. *Journal of Physics D: Applied Physics*, 44(4):045204.
- Kriegseis, J., Simon, B., and Grundmann, S. (2016). Towards in-flight applications? a review on dielectric barrier discharge-based boundary-layer control. *Applied Mechanics Reviews*, 68(2).
- Laadhari, F., Skandaji, L., and Morel, R. (1994). Turbulence reduction in a boundary layer by a local spanwise oscillating surface. *Physics of Fluids*, 6(10):3218–3220.
- Lee, J., Kwon, Y., Hutchins, N., and Monty, J. (2012). Spatially developing turbulent boundary layer on a flat plate. *arXiv preprint arXiv:1210.3881*.
- Leschziner, M. A. (2020). Friction-drag reduction by transverse wall motion—a review. *Journal of Mechanics*, 36(5):649–663.
- Likhanskii, A. V., Shneider, M. N., Macheret, S. O., and Miles, R. B. (2007). Modeling of dielectric barrier discharge plasma actuators driven by repetitive nanosecond pulses. *Physics of plasmas*, 14(7):073501.
- Lim, J. and Kim, J. (2004). A singular value analysis of boundary layer control. *Physics of Fluids*, 16(6):1980–1988.
- Lima Pereira, L. T., Ragni, D., Avallone, F., and Scarano, F. (2020). Pressure fluctuations from large-scale piv over a serrated trailing edge. *Experiments in Fluids*, 61:1–17.
- Mahfoze, O. and Laizet, S. (2017). Skin-friction drag reduction in a channel flow with streamwise-aligned plasma actuators. *International Journal of Heat and Fluid Flow*, 66:83–94.

- Martins, F. J., Foucaut, J.-M., Stanislas, M., and Azevedo, L. F. A. (2019). Characterization of near-wall structures in the log-region of a turbulent boundary layer by means of conditional statistics of tomographic piv data. *Experimental Thermal and Fluid Science*, 105:191–205.
- Marusic, I., Chandran, D., Rouhi, A., Fu, M. K., Wine, D., Holloway, B., Chung, D., and Smits, A. J. (2021). An energy-efficient pathway to turbulent drag reduction. *Nature communications*, 12(1):1–8.
- Melling, A. (1997). Tracer particles and seeding for particle image velocimetry. *Measurement science and technology*, 8(12):1406.
- Millikan, C. B. (1939). A critical discussion of turbulent flow in channels and circular tubes. In *Proc. 5th Int. Congress on Applied Mechanics (Cambridge, MA, 1938)*, pages 386–392. Wiley.
- Moin, P. and Kim, J. (1985). The structure of the vorticity field in turbulent channel flow. part 1. analysis of instantaneous fields and statistical correlations. *Journal of Fluid Mechanics*, 155:441–464.
- Moreau, E. (2007). Airflow control by non-thermal plasma actuators. *Journal of physics D: applied physics*, 40(3):605.
- Nieuwstadt, F., Westerweel, J., and Boersma, B. J. (2016). *Introduction to Theory and Applications of Turbulent Flows*. Springer.
- Nugroho, B., Hutchins, N., and Monty, J. P. (2013). Large-scale spanwise periodicity in a turbulent boundary layer induced by highly ordered and directional surface roughness. *International Journal of Heat and Fluid Flow*, 41:90–102.
- Olivucci, P., Ricco, P., and Aghdam, S. K. (2019). Turbulent drag reduction by rotating rings and wall-distributed actuation. *Physical Review Fluids*, 4(9):093904.
- Olivucci, P., Wise, D. J., and Ricco, P. (2021). Reduction of turbulent skin-friction drag by passively rotating discs. *Journal of Fluid Mechanics*, 923.
- Panton, R. L. (2001). Overview of the self-sustaining mechanisms of wall turbulence. *Progress in Aerospace Sciences*, 37(4):341–383.
- Pastor, R., Vela-Martin, A., and Flores, O. (2020). Wall-bounded turbulence control: statistical characterisation of actions/states. In *Journal of Physics: Conference Series*, volume 1522, page 012014. IOP Publishing.

- Perry, A. and Chong, M. (1982). On the mechanism of wall turbulence. *Journal of Fluid Mechanics*, 119:173–217.
- Prandtl, L. (1904). Über flüssigkeitsbewegung bei sehr kleiner reibung. *Verhandl. III, Internat. Math.-Kong., Heidelberg, Teubner, Leipzig, 1904*, pages 484–491.
- Prandtl, L. (1925). *Applications of modern hydrodynamics to aeronautics*. US Government Printing Office.
- Quadrio, M. and Ricco, P. (2003). Initial response of a turbulent channel flow to spanwise oscillation of the walls. *Journal of Turbulence*, 4(1):007.
- Quadrio, M. and Ricco, P. (2004). Critical assessment of turbulent drag reduction through spanwise wall oscillations. *Journal of Fluid Mechanics*, 521:251–271.
- Quadrio, M. and Ricco, P. (2011). The laminar generalized stokes layer and turbulent drag reduction. *Journal of Fluid Mechanics*, 667:135–157.
- Quadrio, M., Ricco, P., and Viotti, C. (2009). Streamwise-travelling waves of spanwise wall velocity for turbulent drag reduction. *Journal of Fluid Mechanics*, 627:161–178.
- Raffel, M., Willert, C., Scarano, F., Kähler, C., Wereley, S., and Kompenhans, J. (2018). Particle image velocimetry, a practical guide 3rd ed. springer int. publishing.
- Ragni, D., Schrijer, F., Van Oudheusden, B., and Scarano, F. (2011). Particle tracer response across shocks measured by piv. *Experiments in fluids*, 50:53–64.
- Ricco, P. and Hahn, S. (2013). Turbulent drag reduction through rotating discs. *Journal of Fluid Mechanics*, 722:267–290.
- Ricco, P. and Quadrio, M. (2008). Wall-oscillation conditions for drag reduction in turbulent channel flow. *International Journal of Heat and Fluid Flow*, 29(4):891–902.
- Ricco, P., Skote, M., and Leschziner, M. A. (2021). A review of turbulent skin-friction drag reduction by near-wall transverse forcing. *Progress in Aerospace Sciences*, 123:100713.
- Ricco, P. and Wu, S. (2004). On the effects of lateral wall oscillations on a turbulent boundary layer. *Experimental Thermal and Fluid Science*, 29(1):41–52.
- Ritchie, H., Roser, M., and Rosado, P. (2020). Co2 and greenhouse gas emissions. *Our World in Data*. <https://ourworldindata.org/co2-and-other-greenhouse-gas-emissions>.

- Robinson, S. K. (1991). Coherent motions in the turbulent boundary layer. *Annual review of fluid mechanics*, 23(1):601–639.
- Samimy, M. and Lele, S. (1991). Motion of particles with inertia in a compressible free shear layer. *Physics of Fluids A: Fluid Dynamics*, 3(8):1915–1923.
- Scarano, F. (2003). Theory of non-isotropic spatial resolution in piv. *Experiments in Fluids*, 35:268–277.
- Scarano, F., Kempaiah, K. U., and Kotsonis, M. (2022). Piv analysis of skin friction and coherent structures in turbulent drag reduction regimes. In *20th International Symposium on the Application of Laser and Imaging Techniques to Fluid Mechanics*.
- Scarano, F. and Poelma, C. (2009). Three-dimensional vorticity patterns of cylinder wakes. *Experiments in fluids*, 47:69–83.
- Scarano, F. and Riethmuller, M. L. (2000). Advances in iterative multigrid piv image processing. *Experiments in fluids*, 29(Suppl 1):S051–S060.
- Schlatter, P., Li, Q., Örlü, R., Hussain, F., and Henningson, D. S. (2014). On the near-wall vortical structures at moderate reynolds numbers. *European Journal of Mechanics-B/Fluids*, 48:75–93.
- Schlatter, P. and Örlü, R. (2010). Assessment of direct numerical simulation data of turbulent boundary layers. *Journal of Fluid Mechanics*, 659:116–126.
- Schlichting, H. and Kestin, J. (1961). *Boundary layer theory*, volume 121. Springer.
- Schröder, A., Geisler, R., Staack, K. é. a. a., Elsinga, G., Scarano, F., Wieneke, B., Henning, A., Poelma, C., and Westerweel, J. (2011). Eulerian and lagrangian views of a turbulent boundary layer flow using time-resolved tomographic piv. *Experiments in fluids*, 50:1071–1091.
- Sendstad, O. (1992). *The near-wall mechanics of three-dimensional turbulent boundary layers*. Stanford University.
- Sillero, J. A., Jiménez, J., and Moser, R. D. (2014). Two-point statistics for turbulent boundary layers and channels at reynolds numbers up to $\delta^+ = 2000$. *Physics of Fluids*, 26(10):105109.
- Smith, C. and Metzler, S. (1983). The characteristics of low-speed streaks in the near-wall region of a turbulent boundary layer. *Journal of Fluid Mechanics*, 129:27–54.

- Smith, C. R., Walker, J., Haidari, A., and Sobrun, U. (1991). On the dynamics of near-wall turbulence. *Philosophical Transactions of the Royal Society of London. Series A: Physical and Engineering Sciences*, 336(1641):131–175.
- Starikovskiy, A. Y. and Aleksandrov, N. (2021). Gasdynamic flow control by ultra-fast local heating in a strongly nonequilibrium pulsed plasma. *Plasma Physics Reports*, 47(2):148–209.
- Stokes, G. (1851). On the effect of the internal friction on the motion of pendulums. *Philos. Trans*, 9(8).
- Su, Z., Zong, H., Liang, H., Li, J., and Kong, W. (2021). Effect of pulse width on the characteristics of a dielectric barrier discharge plasma actuator driven by high-voltage pulses. *Journal of Physics D: Applied Physics*, 54(33):33LT02.
- Tennekes, H., Lumley, J. L., Lumley, J. L., et al. (1972). *A first course in turbulence*. MIT press.
- Thomas, F., Corke, T., Duong, A., Midya, S., and Yates, K. (2019). Turbulent drag reduction using pulsed-dc plasma actuation. *Journal of Physics D: Applied Physics*, 52(43):434001.
- Thomas, F. O., Corke, T. C., Iqbal, M., Kozlov, A., and Schatzman, D. (2009). Optimization of dielectric barrier discharge plasma actuators for active aerodynamic flow control. *AIAA journal*, 47(9):2169–2178.
- Tong, F., Dong, S., Lai, J., Yuan, X., and Li, X. (2022). Wall shear stress and wall heat flux in a supersonic turbulent boundary layer. *Physics of Fluids*, 34(1):015127.
- Touber, E. and Leschziner, M. A. (2012). Near-wall streak modification by spanwise oscillatory wall motion and drag-reduction mechanisms. *Journal of Fluid Mechanics*, 693:150–200.
- Trujillo, S., Bogard, D., Ball, K., Trujillo, S., Bogard, D., and Ball, K. (1997). Turbulent boundary layer drag reduction using an oscillating wall. In *4th Shear Flow Control Conference*, page 1870.
- Vanderwel, C. and Ganapathisubramani, B. (2015). Effects of spanwise spacing on large-scale secondary flows in rough-wall turbulent boundary layers. *Journal of Fluid Mechanics*, 774:R2.
- Vila, C. S., Vinuesa, R., Discetti, S., Ianiro, A., Schlatter, P., and Örlü, R. (2017). On the identification of well-behaved turbulent boundary layers. *Journal of Fluid Mechanics*, 822:109–138.

- Viotti, C., Quadrio, M., and Luchini, P. (2009). Streamwise oscillation of spanwise velocity at the wall of a channel for turbulent drag reduction. *Physics of fluids*, 21(11):115109.
- Von Karman, T. (1934). Turbulence and skin friction. *Journal of the Aeronautical Sciences*, 1(1):1–20.
- Vukoslavčević, P., Wallace, J. M., and Balint, J.-L. (1991). The velocity and vorticity vector fields of a turbulent boundary layer. part 1. simultaneous measurement by hot-wire anemometry. *Journal of Fluid Mechanics*, 228:25–51.
- Wallace, J. M. (2012). Highlights from 50 years of turbulent boundary layer research. *Journal of Turbulence*, (13):N53.
- Wallace, J. M. and Brodkey, R. S. (1977). Reynolds stress and joint probability density distributions in the u-v plane of a turbulent channel flow. *The Physics of Fluids*, 20(3):351–355.
- Wallace, J. M., Eckelmann, H., and Brodkey, R. S. (1972). The wall region in turbulent shear flow. *Journal of Fluid Mechanics*, 54(1):39–48.
- Wangsawijaya, D. D. and Hutchins, N. (2022). Investigation of unsteady secondary flows and large-scale turbulence in heterogeneous turbulent boundary layers. *Journal of Fluid Mechanics*, 934:A40.
- Westerweel, J. (1997). Fundamentals of digital particle image velocimetry. *Measurement science and technology*, 8(12):1379.
- Whalley, R. D. and Choi, K.-S. (2014). Turbulent boundary-layer control with plasma spanwise travelling waves. *Experiments in Fluids*, 55(8):1–16.
- Wilkinson, S. and Lazos, B. (1988). Direct drag and hot-wire measurements on thin-element riblet arrays. In *Turbulence Management and Relaminarisation*, pages 121–131. Springer.
- Wilkison, S. L., McCOY, T. J., McCAMANT, J. E., Robinson, M. S., and Britt, D. T. (2003). Porosity and density of ordinary chondrites: Clues to the formation of friable and porous ordinary chondrites. *Meteoritics & Planetary Science*, 38(10):1533–1546.
- Wise, D. J., Alvarenga, C., and Ricco, P. (2014). Spinning out of control: Wall turbulence over rotating discs. *Physics of Fluids*, 26(12):125107.
- Wise, D. J. and Ricco, P. (2014). Turbulent drag reduction through oscillating discs. *Journal of Fluid Mechanics*, 746:536–564.

- Wu, X. and Moin, P. (2009). Forest of hairpins in a low-reynolds-number zero-pressure-gradient flat-plate boundary layer. *Physics of Fluids*, 21(9):091106.
- Yakeno, A., Hasegawa, Y., and Kasagi, N. (2009). Spatio-temporally periodic control for turbulent friction drag reduction. In *Sixth International Symposium on Turbulence and Shear Flow Phenomena*. Begel House Inc.
- Yakeno, A., Hasegawa, Y., and Kasagi, N. (2014). Modification of quasi-streamwise vortical structure in a drag-reduced turbulent channel flow with spanwise wall oscillation. *Physics of Fluids*, 26(8):085109.
- Yang, Q. and Hwang, Y. (2019). Modulation of attached exact coherent states under spanwise wall oscillation. In *Eleventh International Symposium on Turbulence and Shear Flow Phenomena (TSFP11)*. Begel House Inc.
- Yao, J., Chen, X., and Hussain, F. (2019). Reynolds number effect on drag control via spanwise wall oscillation in turbulent channel flows. *Physics of Fluids*, 31(8):085108.
- Yu, H., Cui, X., Li, G., and Zheng, J. (2023). Numerical investigation of flow separation control over rotor blades using plasma actuator. *AIAA Journal*, 61(3):1151–1167.
- Yuan, W., Zhang, M., Cui, Y., and Khoo, B. C. (2019). Phase-space dynamics of near-wall streaks in wall-bounded turbulence with spanwise oscillation. *Physics of Fluids*, 31(12):125113.
- Zhou, J., Adrian, R. J., and Balachandar, S. (1996). Autogeneration of near-wall vortical structures in channel flow. *Physics of Fluids*, 8(1):288–290.
- Zhou, J., Adrian, R. J., Balachandar, S., and Kendall, T. (1999). Mechanisms for generating coherent packets of hairpin vortices in channel flow. *Journal of fluid mechanics*, 387:353–396.
- Zong, H., Su, Z., Liang, H., and Wu, Y. (2022). Experimental investigation and reduced-order modeling of plasma jets in a turbulent boundary layer for skin-friction drag reduction. *Physics of Fluids*, 34(8):085133.

ACKNOWLEDGEMENTS

As my time in Delft draws to a close, my heart brims with several emotions. When I first arrived in the Netherlands in August 2017, little did I know the incredible journey that awaited me over the next six years. However, this journey would have been harder to navigate if not for the help and support from many of you.

First and foremost, my heartfelt gratitude to Prof. Dr. Fulvio Scarano, my promoter, who granted me the opportunity to embark on this PhD adventure and remained a beacon of enthusiasm, motivation, and insight throughout. The invaluable lessons I've learned from him will accompany me forever.

I am also grateful to Dr. Bernd Wieneke, Dr. Dirk Micheals, and LaVision GmbH for funding and supporting the NIFTI project. Collaborating with such a talented group has been a truly enriching experience. Additionally, I would like to thank Dr. Andrea Sciacchitano for his guidance in supervising the NIFTI activities and providing invaluable feedback crucial to the project's success.

Dr. Woutijn Baars, my co-promoter, joined the supervisory team midway through my PhD, and his expertise in turbulent boundary layers has been instrumental in the execution of my work. Special mention to Prof. Dr. Marios Kotsonis who laid the foundation for my research on plasma actuators.

My sincere thanks go to the dedicated support staff whose contributions immensely facilitated the smooth progression of my PhD. Colette Russo, Henk-Jan Siemmer, Frits Donker Duyvis, Dennis Bruikman, Peter Duyndam, Stefan Bernardy, and Emiel Langedijk, your continuous support and assistance were invaluable.

This thesis outcome is a testament to the power of teamwork, and I am grateful to Leon Bermel, Jacopo Sem, and Giuseppe Vacca for allowing me to supervise their Master's thesis projects. Working together has been an enriching experience.

Over the years, I've shared my office space with incredible colleagues, past, and present, representing diverse backgrounds that have contributed to rich discussions and fruitful ideas. To those who have already completed their PhDs, including Dr. Tiago Pestana, Dr. David E Faleiros, Dr. Weibo Hu, Dr. Zeno Belligoli, Dr. Yi Zhang, Dr. Constin Jux, Dr. Alexander Spoelstra, Dr. Alessandro Daguano, Dr. Edoardo Saredi, and Dr. Christoph Merten, your research and personal journeys have been an inspiration. To my colleagues who are on the journey - Abdo, Adrian, Ata, Babak, Gabriel, Guanqun, Harris, Hasse, Ilda, Jane, Jordi, Kherlen,

Kiran, Luuk, Renzhi, Sagar, Sven, Tercio, Thomas, Varun, Yifu, Wencan - I extend my heartfelt wishes for success.

Gratitude is also due to my friends and family in Europe, who have made it feel like home. I extend my deepest thanks to Yoga Uncle for being my guardian during my time in the Netherlands. I am grateful for the time I spent in your company and will always hold it dear to my heart. I would like to thank Suman Aunty and Mahima for the many warm conversations over lunch and dinner.

To the "aerodynamics boys," thank you for being an integral part of this journey and sharing unforgettable moments together. Your camaraderie has enriched my life beyond measure.

Lastly, I would like to thank my family, who have been the pillars of support and encouragement throughout my life. To my grandparents, parents, Bharani, Ojas, and Vagvi - you have been the driving force behind my perseverance through triumphs and challenges. Your love, understanding, and unwavering belief in my abilities have been the wind beneath my wings, propelling me forward on this incredible journey. I owe my success to each and every one of you.

Kushal UJJAINI KEMPAIAH

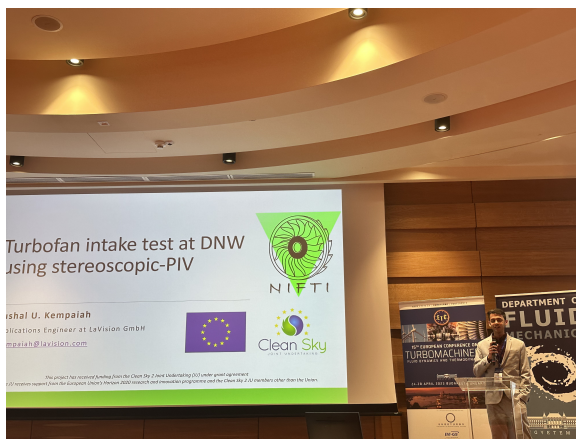
Pune, July 2023

CURRICULUM VITÆ

Kushal Kempaiah was born on April 6, 1995, in the southern state of Karnataka, India. He graduated with a Bachelor's in Mechanical Engineering in 2017 from BMS College of Engineering, Bengaluru, India, where he wrote his thesis on 'Design of Oxidizing Tank and Cold Testing of Hybrid Rocket Motor'. After completing his undergraduate studies, he moved to the Netherlands to pursue a Master's in Aerospace Engineering at TU Delft, specializing in Aerodynamics. His thesis, which focused on 'Spanwise wall oscillation as a drag reduction technique' was performed under the supervision of Prof. Fulvio Scarano and in collaboration with Dr. Bas van Oudheusden, and Dr. Gerrit Elsinga at the faculty of Aerospace Engineering.

In January 2020, Kushal began working as a PIV Applications Engineer at LaVision GmbH, working on the Clean Sky2 project NIFTI, or Non-Intrusive Flow Distortion Measurements within a Turbofan Intake. This project aims to develop and demonstrate a non-intrusive technique for measuring velocity fields across a plane upstream of a large diameter fan of a high bypass ratio aero-engine. The project is in collaboration with German-Dutch Wind Tunnels (DNW), Cranfield University, Imperial College, and Rolls Royce. (DNW), Cranfield University, Imperial College and Rolls Royce.

Kushal's research in active skin friction control has been performed in parallel with the NIFTI project at Delft under the supervision of Prof. Fulvio Scarano.



SUMMARIZED CURRICULUM VITAE

06-04-1995 Born in Mandya, India

EDUCATION

2011–2013 High School
Delhi Public School (IND)

2013–2017 Bachelor of Engineering, Mechanical Engineering
BMS College of Engineering (IND)

2017–2019 Master of Science Aerospace Engineering – Aerodynamics
Delft University of Technology (NED)

2020–2023 PhD Aerospace Engineering – Aerodynamics
Delft University of Technology (NED)

PROFESSIONAL EXPERIENCE

2020–2023 PIV Applications Engineer
LaVision GmbH (GER)

2018 Earth Observation Intern
Netherlands Space Research Organisation (NED)

LIST OF PUBLICATIONS

JOURNAL PUBLICATIONS

1. **Kushal U. Kempaiah**, Fulvio Scarano, Gerrit E Elsinga, Bas W Van Oudheusden, Leon Bermel (2020), 3-dimensional particle image velocimetry based evaluation of turbulent skin-friction reduction by spanwise wall oscillation, *Physics of Fluids* **32(8)** 085111
2. **Kushal U. Kempaiah**, Fulvio Scarano (2022), Feature-based analysis of a turbulent boundary layer under spanwise wall oscillation, *Physics of Fluids* **34 (11)** 115152
3. **Kushal U. Kempaiah**, Fulvio Scarano, Marios Kotsonis (2023), Characterisation and implementation of unsteady AC-DBD plasma actuator for turbulent skin-friction reduction, *in preparatin*
4. **Kushal U. Kempaiah**, Tommaso Piovesan, Dirk Michaelis, Pavlos K Zachos, Roy Gebbink, Bart van Rooijen, Daniel Gil Prieto, David MacManus, Andrea Sciacchitano, Christopher Sheaf (2023), High-resolution Turbofan Intake Flow Characterization by Automated Stereoscopic-PIV in an Industrial Wind Tunnel Environment, *Submitted*

CONFERENCE PUBLICATIONS AND PRESENTATIONS

1. **Kushal U. Kempaiah**, Fulvio Scarano, Gerrit E Elsinga, Bas W Van Oudheusden (2021), Particle image velocimetry based evaluation of coherent structures and skin-friction drag reduction by spanwise wall oscillations. *25th International Congress of Theoretical and Applied Mechanics (ICTAM 2020+1 virtual), Milan, 23-28 August 2021*
2. **Kushal U. Kempaiah**, Jacopo Sem, Woutijn J. Baars (2022), Large-scale flow organization of wall-bounded turbulence over flush-mounted rotating discs. *12th International Symposium on Turbulence and Shear Flow Phenomena (TSFP12), 20-23 July 2022*
3. Fulvio Scarano, **Kushal U. Kempaiah**, Marios Kotsonis (2022), PIV analysis of skin friction and coherent structures in turbulent drag reduction regimes. *20th International Symposium on Applications of Laser and Imaging Techniques to Fluid Mechanics, 11-14 July 2022*
4. **Kushal U. Kempaiah**, Fulvio Scarano, (2022), Comparison of feature-based analysis with correlation techniques of a turbulent boundary layer under spanwise wall

- oscillation.
14th *European Fluid Mechanics Conference*, 13-16 Sept 2022
5. **Kushal U. Kempaiah** (2023), Turbofan intake test at DNW using stereoscopic-PIV.
15th *European Turbomachinery Conference*, 24-28 April 2023